Primordial non-Gaussianity with Planck

Alessandro Renzi, Supervisor: Carlo Baccigalupi, Co-supervisor: Michele Liguori

10 May 2013

Contents

List of Figures

List of Tables

Chapter 1

Introduction

We are currently well inside the so-called High-Precision Era of Cosmology. Nearly 50 years after the discovery of a Cosmic Microwave Background (CMB), in the 1965 from Penzias and Wilson (Penzias and Wilson 1965), we reached the theoretical ideal limits of estimation for many of the possible parameters derived from this observable. The CMB, that is the relic radiation of the primordial universe and the oldest observable today, allows the most accurate measurement of cosmological parameters. Moreover, the theory that describes the CMB as well as the model that describe the Universe now and in its early stages is based on a "simple" (namely linear) theory.

Since the CMB is the oldest observable in the Universe is in particular the ideal dataset to test initial conditions. The present cosmological theory is based on some predictions on inflation, an early period of accelerated expansion of the Universe, that are well verified:

- (nearly) scale-invariant spectrum;

- Gaussianity of the CMB fluctuations;
- flatness of the Universe.

In the High-precision era is of fundamental importance the study of small departures from those predictions.

In particular, non-Gaussianity (NG), main topic of this thesis, is showed to be a powerful tool to constraint inflation. We will look at this point more carefully on Chapter (2)

The first upper limit on NG comes from COsmic Background Explorer (COBE) (Bennett et al. 1996). Then, more recently, the Wilkinson Microwave Anisotropy Probe (WMAP) experiment poses more stringent constraints (Hinshaw et al. 2012a). In Chapter (3) we will describe the Planck satellite experiment, that represents the most accurate, nearly-ideal, and recent CMB experiment, for NG estimation from CMB.

In this thesis we developed, validated and applied to data, the most advanced statistical tools to measure NG in the high resolution CMB datasets coming from the Planck satellite First Cosmology Public Release. In particular, our efforts were conveyed to the development of the so called (Komatsu-Spergel-Wandelt) KSW estimator (Komatsu et al. 2005), the Planck breeded version of the estimator used by the WMAP team, that was selected as a front-runner estimator for NG for the Planck first public release. Moreover, we developed a second estimator, the Skew-Cl (Munshi and Heavens 2010). This estimator has the advantage to estimate NG in armonic space giving rise the possibility to study possible contamination that can be present in the data. Both the description and the validation of KSW and Skew-Cl are fully covered in Chapter (4) and Chapter (5).

Finally, in the conclusion Chapter (6) we will describe and discuss the results we obtained, showing not only the numbers, but focusing in particular on their robustness, achieved through an intense campaign of validation made inside the Planck collaboration, that allowed us to claim the final constraint on inflationary NG.

Chapter 2

The early Universe

2.1 Inflationary framework

The study of primordial NG is generally aimed at testing primordial inflation. Throughout this chapter we will describe the theoretical framework of inflation needed to understand the physics and the motivation for NG.

The inflationary cosmology (Albrecht and Steinhardt 1982; Guth 1981; Linde 1982, 1983) is a sort of add-on to the Hot Big Bang model, it occurs at early times without altering any of the successful predictions of the model at later times.

2.1.1 Lemaître-Friedmann-Robertson-Walker Universe

In this paragraph we will quickly review the standard homogeneous and isotropic model of the Universe described by the Lemaître-Friedmann-Robertson-Walker (LFRW) metric (Bartolo et al. 2004a),

$$ds^2 = -dt^2 + a^2(t)\left[\frac{dr^2}{1-\mathcal{K}r^2} + r^2(d\theta^2 + \sin^2\theta d\varphi^2)\right], \quad (2.1)$$

where t is the cosmic time, r, θ, φ are the comoving (polar) coordinates, $a(t)$ is the scale factor of the Universe, and $\mathcal{K}$ is the curvature constant of 3-dimensional hypersurfaces. If the Universe is filled with matter described by the energy-momentum tensor $T_{\mu\nu}$ of a perfect fluid with energy density ρ and pressure P, the solution of Einstein equations

$$G_{\mu\nu} = 8\pi G_N T_{\mu\nu}, \quad (2.2)$$

with $G_{\mu\nu}$ the Einstein tensor and G_N the Newtonian gravitational constant, is provided by the Friedmann equations

$$H^2 = \frac{\rho}{3M_{\rm Pl}^2} - \frac{\mathcal{K}}{a^2}, \quad (2.3)$$

$$\frac{\ddot{a}}{a} = -\frac{\rho + 3P}{6M_{\rm Pl}^2}, \quad (2.4)$$

$$\dot{\rho} = -3H(\rho + \mathrm{P}). \quad (2.5)$$

where $H = \dot{a}/a$ is the Hubble expansion parameter, dots denote differentiation with respect to cosmic time t, and $M_{\rm Pl} = (8\pi G_N)^{-1/2}$ is the reduced Planck mass[1].

[1] We can include the Cosmological Constant considering it a possible time-independent contribution to the energy density and pressure of the vacuum, so that (Liddle and Lyth 2000) $\rho_{\rm total} = \rho + \rho_{\rm vac}$, $\mathrm{P}_{\rm total} = \mathrm{P} + \mathrm{P}_{\rm vac}$ with $\rho_{\rm vac} = -\mathrm{P}_{\rm vac} = M_{\rm Pl}^2\Lambda$, where Λ is the Cosmological Constant.

Eq. (2.3) allows to define the critical density, ρ_c, for a spatially flat Universe without cosmological constant, that is

$$\rho_{\rm c} \equiv \frac{3H_0^2}{8\pi G} = 3H_0^2 M_{\rm Pl}^2 \,. \tag{2.6}$$

The critical density is the energy density of a flat Universe. From the critical density is usually defined the density parameter $\Omega = \rho/\rho_c$. The inverse of the Hubble parameter H^{-1} is also a quantity that will be often used in the following. It plays an important role during inflation: it represents the Hubble horizon (in units of $c = 1$) and is an estimate of the distance that light can travel while the Universe expands in the early stages of evolution. The Hubble radius represents a characteristic length scale beyond which causal processes cannot operate. During inflation the comoving Hubble horizon, $(aH)^{-1}$, decreases with time since the scale-factor a grows quasi-exponentially, and the Hubble radius remains almost constant. Therefore, a given comoving length scale, L, will become larger than the Hubble radius and eventually *leave the Hubble horizon*.

2.1.2 Inflation basics

Inflation is defined as an early period of acceleration in the Universe expansion rate, namely $\ddot{a} > 0$. As we will see later this mechanism was originally invoked to solve several problems arising in the standard Hot Big Bang model. The problems are illustrated in subsection 2.1.3. However, in the following paragraphs we will focus on how to set up a physical mechanism to produce $\ddot{a} > 0$. We want to understand the consequences of the inflationary hypothesis in a LFRW Universe. Eq. (2.4) shows that a period of inflation is possible if the pressure P is *negative*

with

$$P < -\frac{\rho}{3} . \tag{2.7}$$

Let us consider the special case where $P = -\rho$, this is called a de Sitter stage.

We can re-write the inflationary condition in an equivalent alternative expression that has more physical insight, $d/dt(1/aH) < 0$. This form is particularly important since it tells that during inflation the Hubble comoving length ($(aH)^{-1}$) decrease. From the energy continuity Eq. (2.5) and Eq. (2.3) (neglecting the curvature $\mathcal{K}$ which is soon redshifted by the a^{-2} factor) we see that in a de Sitter phase ρ = constant and

$$H = H_{\rm I} = \text{constant} , \tag{2.8}$$

where I stands for Inflation. Integrating the Hubble equation $H(t) = d\ln(a)/dt$ with the condition in Eq. (2.8) gives

$$a(t) = a_i \exp\left(\int_{t_i}^{t} H(t')dt'\right) = a_i \exp\left[H_I(t - t_i)\right] , \tag{2.9}$$

where we have defined t_i as the time at which inflation starts.

In the following sections we will build a simple model characterized by an initial de Sitter phase and discuss its implications for the standard cosmological model.

It is clear that ordinary matter or radiation cannot produce a pressure $\mathcal{P} < 0$. In order to get a negative pressure sufficient for accelerating the expansion, we resort to a scalar field. In the following we will see how a scalar field can generate negative pressure, but before, we will provide a brief motivation for inflation.

2.1.3 Motivation for inflation

Primarily, this thesis is about experimental tests of cosmological inflation. As stated in (Liddle and Lyth 2000) the main modern motivation for inflation is that it is a mechanism for generating inhomogeneities in the universe, which leads to the formation of structures. However, inflation was originally introduced to solve some "historical problems" that arise studying the initial conditions for the Hot Big Bang model. It was a great success of the theory that inflation can even seed structure formation.

The first problem is the so called **flatness problem**. Using the definition of the density parameter $\Omega = \rho/\rho_c$, we can rewrite Eq. (2.3) as

$$\Omega - 1 = \frac{\mathcal{K}}{(aH)^2} . \tag{2.10}$$

where $\mathcal{K}$ is the spatial curvature, . The density Ω stays constant if the Universe is flat. Otherwise, it should be $|1 - \Omega| \propto t$ during radiation domination era, and $|1 - \Omega| \propto t^{2/3}$ during matter domination. Since we observe a spatially flat Universe today, we obtain a fine tuning problem on the initial conditions. To get the Universe as flat as it is at $t = 0$ we need $\Omega_{\text{primordial}} = 1 + \epsilon$ where $\epsilon \to 0$ as we look at earlier times.

Besides flatness, we also have an **horizon problem**. If we look at CMB pho-

tons coming from regions of the sky separated by more than the horizon scale at last scattering (nearly 1 degree) they cannot have interacted before decoupling. Within the Hot Big Bang model there is no way to explain why the temperature seen in different regions of the sky is so accurately uniform. The horizon problem is the problem of how the CMB is so homogeneous and isotropic.

The last "historical" problem are the so called **unwanted relics**. Since the Hot Big Bang model provide very high temperature at the beginning of the expansion, the primordial universe can produce relic to a level forbidden by current observations. Prominent examples are the magnetic monopole (Rajantie 2012), primordial magnetic field (Yamazaki et al. 2012), cosmic strings and topological defects in general (Vilenkin and Shellard 1994). The production rate of those relics in the Hot Big Bang model is so high that they should be observed today.

A final problem we have to address is that of the **generation of primordial perturbations**. As important as the solution to the aforementioned problems, inflation provide us a theory of the origin of the inhomogeneity. Even if the Universe is very close to be perfectly isotropic and homogeneous on large scales, the CMB displays anisotropies whose generations needs to find an explanation. Within the Hot Big Bang model we can define a mechanism to evolve early time inhomogeneities into CMB anisotropies and cosmological structures, however we do need a model for the initial conditions. In the remaining part of this chapter we well see how inflation is a paradigm that gives us a way to set initial conditions and a base for building a standard cosmological model of the Universe.

2.1.4 Scalar field basics

Let us first review some basic concepts about a scalar field and in the next subsections we will see how we can relate this to inflation.

The energy-momentum tensor for a minimally-coupled scalar field ϕ is given by

$$T_{\mu\nu} = -2\frac{\partial \mathcal{L}}{\partial g^{\mu\nu}} + g_{\mu\nu}\mathcal{L} = \partial_\mu\phi\partial_\nu\phi + g_{\mu\nu}\left[-\frac{1}{2}g^{\alpha\beta}\partial_\alpha\partial_\beta\phi - V(\phi)\right] . \tag{2.11}$$

The action for a minimally-coupled scalar field ϕ is given by

$$S \equiv \int d^4x\sqrt{-g}\mathcal{L} = \int d^4x\sqrt{-g}\left[-\frac{1}{2}g^{\mu\nu}\partial_\mu\phi\partial_\nu\phi - V(\phi)\right] , \tag{2.12}$$

where g is the determinant of the metric tensor $g_{\mu\nu}$ such that $g_{\mu\nu}g^{\nu\lambda} = \delta^\lambda_\nu$ and $V(\phi)$ is the scalar field potential. By varying the action with respect to ϕ one obtains the usual Klein-Gordon equations;

$$\Box\phi = \frac{\partial V}{\partial\phi} , \tag{2.13}$$

where $\Box$ is the covariant D'Alembert operator,

$$\Box\phi = \frac{1}{\sqrt{-g}}\partial_\nu\left(\sqrt{-g}g^{\mu\nu}\partial_\mu\phi\right) . \tag{2.14}$$

The equation of motion for a field ϕ described by the action Eq. (2.12) becomes

$$\ddot{\phi} + 3H\dot{\phi} - \frac{\nabla^2\phi}{a^2} + V'(\phi) = 0 \,, \tag{2.15}$$

where $V'(\phi) = (\partial V(\phi)/\partial\phi)$. The most interesting point about a scalar field in a LFRW metric is the appearance of the friction term $3H\dot{\phi}$ due to the expansion of the Universe. This term describes the friction that the scalar field experiences while rolling down its potential.

Since in the following sections we will be interested in studying the generation of cosmological perturbations from quantum fluctuations of the inflaton field, we are going to split the inflaton field as

$$\phi(t, \mathbf{x}) = \phi_0(t) + \delta\phi(t, \mathbf{x}) \,, \tag{2.16}$$

where ϕ_0 (from now on we will call $\phi_0 \equiv \phi$) is the 'classical' (infinite wavelength) field, that is the expectation value of the inflaton field on the initial isotropic and homogeneous state, while $\delta\phi(t, \mathbf{x})$ represents the quantum fluctuations of the classical field ϕ. The next subsection will be focusing on to the study of ϕ_0 and of the background evolution. The following one instead, will be devoted to the study of the evolution of the quantum perturbations during inflation. As we will explain later in better detail, inflation will be the key ingredient to evolve quantum fluctuations to the classical ones observed through the CMB. The final part of the chapter will try to establish a link between the theory of inflation and the way in which we can constrain it with non-Gaussianity.

2.1.5 A simple model of inflation

In a LFRW Universe accelerated expansion is possible only if a negative pressure component dominates the energy balance as we saw in Eq. (2.4), that is $\rho+3P < 0$.

Scalar fields possess the feature of a potential energy that may redshift extremely slowly as the Universe expand. This corresponds to an effective equation of state with a negative pressure. To check this, the starting point is to write the expressions for the energy density and pressure of a homogeneous scalar field $\phi \equiv \phi(t)$, called the inflaton, with a potential $V(\phi)$,

$$\rho_\phi = \frac{1}{2}\dot{\phi}^2 + V(\phi) \,, \tag{2.17}$$

$$P_\phi = \frac{1}{2}\dot{\phi}^2 - V(\phi) \,. \tag{2.18}$$

Different $V(\phi)$ can be obtained in specific particle physics scenarios. For a review see (Bartolo et al. 2004a). We just focus here on building a potential $V(\phi)$ that produce the desired accelerated expansion. If we impose the condition

$$V(\phi) \gg \dot{\phi}^2 \,, \tag{2.19}$$

then we obtain

$$P_\phi \simeq -\rho_\phi \,. \tag{2.20}$$

Then, the necessary condition for acceleration is that Eq. (2.19) holds. This condition is called the *slow-roll condition*. So, a scalar field that is the dominant component in the Universe and whose potential energy dominates over the kinetic

term is sufficient to give inflation[2].

Let us study in better detail how the slow-roll condition gives rise to inflation. The equation of motion for a homogeneous scalar field is

$$\ddot{\phi} + 3H\dot{\phi} + V'(\phi) = 0 \, . \tag{2.21}$$

The slow-roll condition, Eq. (2.19), can be achieved if the inflaton field ϕ is in a region where the potential is sufficiently flat (how flat it should be exactly will be quantified soon). We can expect that the flat potential is going to make $\ddot{\phi}$ negligible. With those considerations the Friedmann Eq. (2.3) and the equation of motion (2.15) becomes

$$H^2 \simeq \frac{V(\phi)}{3M_{Pl}^2} \, , \tag{2.22}$$

$$3H\dot{\phi} \simeq -V'(\phi) \, , \tag{2.23}$$

where we have assumed that the inflaton field dominates the energy density of the Universe. The last equation combined with the slow-roll condition imposes

$$V(\phi) \gg \dot{\phi}^2 \quad \Rightarrow \quad H^2 \gg \frac{(V')^2}{V} \, , \tag{2.24}$$

$$3H\dot{\phi} \gg \ddot{\phi} \quad \Rightarrow \quad H^2 \gg V'' \, . \tag{2.25}$$

Those equation can be rewritten introducing the *slow-roll parameters*

[2]We can safely neglect spatial curvature, matter and radiation since their contribution to the energy density is redshifted away during inflation. Similar arguments can be applied to the possible small inhomogeneities to justify the use of the background LFRW metric.

$$\epsilon(\phi) = \frac{M_{Pl}^2}{2}\left(\frac{V'}{V}\right)^2 , \tag{2.26}$$

$$\eta(\phi) = M_{Pl}^2\frac{V''}{V} , \tag{2.27}$$

where now we can recast the slow-roll condition as

$$\epsilon(\phi) \ll 1 , \tag{2.28}$$

$$|\eta(\phi)| \ll 1 . \tag{2.29}$$

A successful inflationary phase has to follow from Eqs. (2.26), (2.27), and (2.23). It is easy to see that Eq. (2.22) is a consequence of Eqs. (2.23) and (2.28). Note that at first-order in the slow-roll parameters ϵ and η can be considered constant, since the potential is very flat. In particular is very important to note that $\dot{\epsilon}, \dot{\eta} = O(\epsilon^2, \eta^2)$.

The parameter ϵ can be rewritten as

$$\epsilon = -\frac{\dot{H}}{H^2} , \tag{2.30}$$

thus it quantifies how much the Hubble rate H changes with time during inflation. This definition help us to modify the Eq. (2.4) as

$$\frac{\ddot{a}}{a} = \dot{H} + H^2 = (1-\epsilon)H^2 , \tag{2.31}$$

that tell us that inflation can be obtained only if $\epsilon < 1$. As soon as this condi-

tion does not hold anymore, inflation ends.

A simple example of scalar field that gives rise to a negative pressure is one with a power-law potential $V(\phi) \sim \phi^n$. This model is called *chaotic inflation* (Linde 1990). In this particular inflation model the field ϕ starts slow-rolling down the potential, making the universe exponentially expanding. When it reaches the minimum of the potential it starts to oscillate rapidly, terminating inflation. Single field inflationary models can be broadly divided into three classes (Bartolo et al. 2004a): "small field" where ($\eta < -\epsilon$) and a typically they have the form $V(\phi) = \Lambda^4[1 - (\phi/\mu)]$; "large field" (or chaotic) where ($0 < \eta < 2\epsilon$) and typical examples are represented by polynomial potential $V(\phi) = \Lambda^4(\phi/\mu)^p$ and exponential potentials $V(\phi) = \Lambda^4 \exp(\phi/\mu)$; last, the "hybrid" type class where ($0 < 2\epsilon < \eta$) are of the form $V(\phi) = \Lambda^4[1 + (\phi/\mu)^p]$.

The very last ingredient of inflation stems from the consideration that we need to recreate the condition necessary to the Big Bang Cosmology to set in. During inflation any contribution to the energy density and entropy of the Universe has been redshifted away by the inflationary expansion, so we must find a mechanism to repopulate the Universe by a hot radiation fluid to restart the Big Bang model. This is achieved through a process called *reheating*. At the end of inflation, the inflaton field ϕ roll fast along its potential. The scalar field will reach the minimum of its potential and will start to oscillate around it. During the oscillatory phase it interacts with other particles, decaying over time, producing particles and energy. At the end of this phase, radiation dominates and the standard cosmological model describe Universe evolution from now on.

In the ordinary scenario of reheating (Abbott et al. 1982; Albrecht et al. 1982; Dolgov and Linde 1982; Linde 1982) such a transfer corresponds to the decay of

the inflaton field into other lighter particles to which it couples through a decay rate Γ_ϕ. Such a decay damps the inflaton oscillations and when the decay products thermalize and form a thermal background the Universe is finally reheated.

2.1.6 Solution to the historical cosmological problems

Let us conclude this section with the solutions of the "historical" cosmological problems. As mentioned in subsection (2.1.3), a crucial quantity for understanding the generation of the primordial perturbations and inflationary dynamics is the Hubble radius H^{-1}. Now, to solve the horizon and flatness problems, inflation must last for "a long enough period" so that a small, smooth patch of size that is smaller than the Hubble radius can grow to encompass *at least* the entire observable Universe (see figure 2.1). Typically the amount of inflation is measured in terms of the numbers of *e-folding*, defined as

$$N_{TOT} = \int_{t_i}^{t_f} H dt \,, \tag{2.32}$$

where t_i and t_f are the inflation start and end respectively. Since the largest scale we can probe today is about ~ 4200 Mpc, then $N_{\rm TOT} \simeq 60$. Instead, if we are interested in the number of e-folding from the time when a particular wavelength λ leaves the horizon till the end of inflation we have,

$$N_\lambda = \int_{t(\lambda)}^{t_f} H dt = \ln\left(\frac{a_f}{a_\lambda}\right) \,, \tag{2.33}$$

where $t(\lambda)$ is the time when λ leaves the horizon during inflation and $a_\lambda = a(t(\lambda))$. The cosmologically interesting scales probed by the CMB anisotropies correspond to $N_\lambda \simeq 40-60$. If we produce acceleration for a large enough number

of e-folds, we see that we can solve all the "historical problems" of the cosmological model:

- **Flatness:** the solution to this problem within the inflationary hypothesis relies on Eq. (2.10). Since the scale factor a grows exponentially with time and that the Hubble parameter H is nearly constant, then the right hand side of this equation goes to zero very fast whatever value of the curvature $\mathcal{K}$ we have.

- **Horizon:** the inflationary solution to this problem is very well explained in figure (2.1). The Universe that we observe now was well inside the Hubble radius (and consequently in causal contact) at the end of inflation.

- **Unwanted Relics:** the inflation solution is to dilute the numbers of unwanted relics below the observational limit.

All those solutions need exactly N_λ e-folds to occur.

2.2 Linear cosmological perturbations

We saw in the previous section how inflation can address the classic fine-tuning problems of standard Hot Big Bang cosmology when it comes to define initial conditions. However a crucial issue remains open: how can a homogeneous and isotropic Universe that lasts after inflation generate the structures in the Universe? To answer this question, we need to discuss the evolution of quantum fluctuations of the inflaton field $\delta\phi(t, \mathbf{x})$ (see Eq. (2.16) and following comments). We will see in fact that, quantum perturbations of the field are are converted into classical fluctuations at horizon crossing, and these in turn seed primordial cosmological

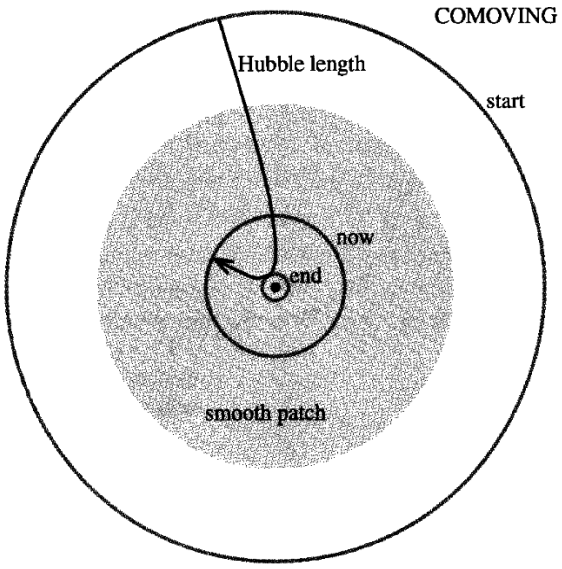

Figure 2.1: Evolution of the Hubble radius in comoving units. During inflation the Hubble (comoving) radius exponentially shrinks to the end point inf figure, then at the end of inflation, start again to expand within the standard Hot Big Bang model. Figure taken from (Liddle and Lyth 2000).

perturbations in matter and radiation components when inflation ends. Our current understanding of the origin of structures in the Universe is that, once the Universe became matter dominated ($z \sim 3200$), initial density inhomogeneities ($\delta\rho/\rho \sim 10^{-5}$) were amplified by gravity and grew into the structure we see today (Coles and Lucchin 1995; Peebles 1980). The existence of these primordial inhomogeneities was for the first time confirmed by the COBE discovery of CMB anisotropies (Smoot et al. 1992).

In the framework of the Hot Big Bang model the initial conditions, or seeds, of those perturbations must be put by hand. Figure 2.2 shows how inflation provides a physical mechanism for generating primordial density perturbations and explain CMB anisotropies. As mentioned at the beginning of this section, two are the key

ingredients:

- quantum fluctuations of the inflaton field are excited during inflation and stretched to cosmological scales. At the same time, as the inflaton fluctuations couple to the metric perturbations through Einstein's equations, ripples on the metric are also excited and stretched to cosmological scales;

- the metric perturbations induce fluctuations in the baryon and photon density. When fluctuation modes re-enter the (acoustic) horizon, baryons and photons interact via Thomson scattering, before hydrogen recombination, setting up acoustic oscillations;

from the two points above, we see that the amplitude and statistical features of primordial cosmological perturbations will depend on the properties of the fluctuations of the scalar field, which we are going to study in the next section.

2.2.1 Quantum fluctuations of a generic scalar field during a de Sitter stage

In this section we will see how quantum fluctuations are generated during inflation. The first important point to note is that the mechanism by which the quantum fluctuations of the inflaton field are produced during an inflationary epoch is not peculiar to the inflaton field itself, rather it is generic to any scalar field evolving in an accelerated background. We will call this scalar field χ.

So, let us consider a generic scalar field χ with potential $V(\chi)$ in a pure de Sitter stage, during which H is constant. The analogue of Eq. (2.16) can be written using this new field,

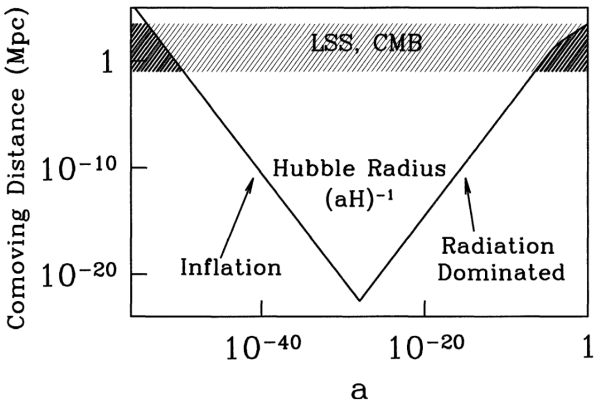

Figure 2.2: The comoving Hubble radius as a function of scale factor. Scales of cosmological interest (shaded band) were larger than the Hubble radius until $a \sim 10^{-5}$. Dark shaded regions show when these scales were smaller than the Hubble radius, and therefore susceptible to microphysical processes. Very early on, before inflation operated, all scales of interest were smaller than the Hubble radius and therefore susceptible to microphysical processing. Similarly, at very late times, scales of cosmological interest came back within the Hubble radius. Figure taken from (Dodelson 2003).

$$\chi(\tau, \mathbf{x}) = \chi(\tau) + \delta\chi(\tau, \mathbf{x}) \,, \tag{2.34}$$

where, again, $\chi(\tau)$ is the homogeneous classical value of the scalar field. The perturbation $\delta\chi$ is now an operator and represent the quantum fluctuation of χ and τ is the conformal time related to the cosmic time t through $d\tau = dt/a(t)$.

The scalar field χ is quantized by implementing the standard technique of second quantization, where we will make the redefinition $\delta\tilde{\chi} = a\delta\chi$. Recalling the second quantization, the operator $\delta\tilde{\chi}$ can be written in terms of creation and annihilation operators $a_{\mathbf{k}}$ and $a^{\dagger}_{\mathbf{k}}$,

$$\delta\tilde{\chi}(\tau, \mathbf{x}) = \int \frac{d^3\mathbf{k}}{(2\pi)^{3/2}} \left[u_k(\tau) a_{\mathbf{k}} e^{i\mathbf{k}\cdot\mathbf{x}} + u_k^*(\tau) a^{\dagger}_{\mathbf{k}} e^{-i\mathbf{k}\cdot\mathbf{x}} \right] \,, \tag{2.35}$$

where creation and annihilation operators for $\tilde{\delta\chi}$ (not for $\delta\chi$) satisfy the standard commutation relations

$$[a_{\mathbf{k}}, a_{\mathbf{k}'}] = 0 \,, \tag{2.36}$$

$$\left[a_{\mathbf{k}}, a^{\dagger}_{\mathbf{k}'}\right] = \delta^{(3)}(\mathbf{k} - \mathbf{k}') \,, \tag{2.37}$$

and the modes $u_k(\tau)$ are normalized so that they satisfy the condition

$$u^{*}_k u'_k - u_k u^{*\prime}_k = -i \,, \tag{2.38}$$

deriving from the usual canonical commutation relations between the operators $\tilde{\delta\chi}$ and its conjugate momentum $\Pi = \tilde{\delta\chi}'$. Here primes denote derivatives with respect to the conformal time τ.

Note that if u_k has a positive frequency mode with respect to the conformal time-like Killing vector ($\partial/\partial\tau$ for our metric), i.e., $\dot{u}_k = -i\omega_k u_k$, then the condition gives $u_k(\tau) = (2\omega_k)^{-1/2} e^{-i\omega_k \tau}$, a ground state in the Minkowski vacuum. This is why we use directly the redefined version of Eq. (2.35), see in particular (Komatsu 2002).

Similarly as Eq. (2.13) the evolution of the scalar field $\chi(\tau, \mathbf{x})$ is given by the Klein-Gordon equation

$$\Box\chi = \frac{\partial V}{\partial \chi} \,. \tag{2.39}$$

The Klein-Gordon equation in an unperturbed LFRW Universe is

$$\chi'' + 2\mathcal{H}\chi' = -a^2 \frac{\partial V}{\partial \chi} \,, \tag{2.40}$$

where $\mathcal{H} \equiv a'/a$ is the Hubble expansion rate in conformal time.

In this section we are interested in the perturbations of the scalar field χ. To simplify the treatment, while preserving the fundamental physical ideas, we will neglect the metric perturbations. The connection with the metric perturbations will be studied in the following subsections.

Perturbing equation 2.39, but neglecting the metric perturbation we have an equation of motion for the eigenfunctions $u_k(\tau)$

$$u_k'' + \left(k^2 - \frac{a''}{a} + m_\chi^2 a^2\right) u_k = 0 \,, \tag{2.41}$$

where we introduced the effective mass of the scalar field $m_\chi^2 = \partial^2 V/\partial\chi^2$. Let us now study the asymptotic behaviour of Eq. (2.41).

Sub-horizon scales. For scales $k^2 \gg a''/a$, the mass term is negligible, so Eq. (2.41) becomes

$$u_k'' + k^2 u_k = 0 \,, \tag{2.42}$$

whose solution is a plane wave

$$u_k \propto e^{-ik\tau} \,. \tag{2.43}$$

Thus, fluctuations with wavelength within the cosmological horizon oscillate.

Super-horizon scales. For scales $k^2 \ll a''/a$, Eq. (2.41) becomes

$$u_k'' - \left(\frac{a''}{a} - m_\chi^2 a^2\right) u_k = 0 \,. \tag{2.44}$$

For a massless scaler field, $m_\chi^2 = 0$, the solution of Eq. (2.44) is a superposition

of a growing (+) and a decaying (-) mode:

$$u_k = B_+(k)a + B_-(k)a^{-2} \ . \tag{2.45}$$

We can fix the amplitude of the growing mode, B_+ , by matching the (absolute value of the) solution (2.45) to the plane wave solution (in a flat space-time and sub-horizon) when the fluctuation with wavenumber k leaves the horizon ($k = aH$)

$$|B_+(k)| = \frac{H}{\sqrt{2k^3}} \ , \tag{2.46}$$

so that the quantum fluctuations of the original scalar field χ on super-horizon scales are constant,

$$|\delta\chi_k| = \frac{|u_k|}{a} = \frac{H}{\sqrt{2k^3}} \ . \tag{2.47}$$

Is it possible to solve exactly Eq. (2.41). In a de Sitter stage, as $a = -(H\tau)^{-1}$ we have

$$\frac{a''}{a} - m_\chi^2 a^2 = \frac{2}{\tau^2}\left(1 - \frac{m_\chi^2}{2H^2}\right) \ , \tag{2.48}$$

so that we can rewrite Eq. (2.41) in the form

$$u_k'' + \left(k^2 - \frac{\nu_\chi^2 - 1/4}{\tau^2}\right) = 0 \ , \tag{2.49}$$

where

$$\nu_\chi^2 = \left(\frac{9}{4} - \frac{m_\chi^2}{H^2}\right) \ . \tag{2.50}$$

When the mass m_χ^2 is constant in time, Eq. (2.49) is a Bessel equation whose general solution for *real* ν_χ is (Bartolo et al. 2004a)

$$u_k(\tau) = \frac{\sqrt{\pi}}{2} e^{i(\nu_\chi+\frac{1}{2})\frac{\pi}{2}} \sqrt{-\tau} H^{(1)}_{\nu_\chi}(-k\tau) \,, \tag{2.51}$$

where $H^{(1)}_\nu(x)$ is the Hankel functions of first kind, $H^{(2)}_\nu(x) = [H^{(1)}_\nu(x)]^*$, and the fluctuations $\delta\tilde{\chi}$ becomes

$$\begin{aligned} \delta\tilde{\chi}(\mathbf{x},\tau) \;=\; & \frac{\sqrt{-\pi\tau}}{2} \int \frac{d^3\mathbf{k}}{(2\pi)^{3/2}} \Big[a_\mathbf{k} H^{(1)}_\nu(-k\tau) e^{i\mathbf{k}\cdot\mathbf{x}+\frac{\pi}{2}(\nu_\chi+\frac{1}{2})+} \;, \\ & u^*_k(\tau) a^\dagger_\mathbf{k} e^{-i(\mathbf{k}\cdot\mathbf{x}+\frac{\pi}{2}(\nu_\chi+\frac{1}{2}))} \Big] \,. \end{aligned} \tag{2.52}$$

There are some important considerations that follows from Eq. (2.51) and (2.52):

- Gaussianity of the fluctuations (Komatsu 2002):

  since all the k modes in the integral of Eq. (2.52) are independent of each other, the nearly infinite sum of those modes makes $\delta\tilde{\chi}$ obey Gaussian statistics almost exactly, because of the central limit theorem; thus, the two-point statistics specify all the statistical properties of $\delta\tilde{\chi}$ (we will see the two point statistics definition in the following subsection). This is a generic property of the ground-state quantum fluctuations.

- Amplitude of the fluctuations on *superhorizon scales* (Bartolo et al. 2004a):

  defining the vacuum state as $a_\mathbf{k}|0\rangle = 0$ we can calculate the amplitude of ground-state $\delta\chi(\tau,\mathbf{x})$ fluctuations as

$$
\begin{aligned}
|\delta\chi_k| &= \langle 0|\delta\chi^{\dagger}(\tau,\mathbf{x})\delta\chi(\tau,\mathbf{x})|0\rangle = \int_0^{\infty}\frac{k^2dk}{2\pi^2a^2(\tau)}|u_k(\tau)|^2\ , \\
&= \frac{-\tau}{8\pi a^2(\tau)}\int_0^{\infty}k^2dk|H^{(1)}_{\nu_\chi}(-k\tau)|^2\ . \qquad (2.53)
\end{aligned}
$$

On superhorizon scales, the fluctuation of the scalar field $\delta\chi_k \equiv u_k/a$ with a non-vanishing mass is not exactly constant, but it acquires a dependence upon time (Bartolo et al. 2004a)

$$
|\delta\chi_k| = 2^{(\nu_\chi-3/2)}\frac{\Gamma(\nu_\chi)}{\Gamma(3/2)}\frac{H}{\sqrt{2k^3}}\left(\frac{k}{aH}\right)^{\frac{3}{2}-\nu_\chi}\ ; \qquad (2.54)
$$

that is valid for values of the scalar field mass $m_\chi \leq 3/2H$ (Γ's are the Gamma functions). For very massive scalar fields $m_\chi \gg 3/H$ the fluctuations of the scalar field remain in the vacuum state and do not produce perturbations on cosmologically relevant scales (Bartolo et al. 2004a). Instead, for very light field $m_\chi \ll 3/H$ the Eq. (2.54) further simplify, in analogy with the slow-roll inflaton field, and can be written as

$$
|\delta\chi_k| = \frac{H}{\sqrt{2k^3}}\left(\frac{k}{aH}\right)^{\frac{3}{2}-\nu_\chi}\ , \qquad (2.55)
$$

where

$$
\begin{aligned}
\eta_\chi &= \frac{m_\chi^2}{3H^2} \ll 1\ , \qquad (2.56) \\
\frac{3}{2}-\nu_\chi &\simeq \eta_\chi\ . \qquad (2.57)
\end{aligned}
$$

The fundamental point to keep in mind in Eq. (2.55) and (2.54) is that the quantum fluctuation of the (light) scalar field χ that are initially generated on subhorizon scales, are gravitationally amplified and stretched to super-horizon scales because of the accelerated expansion of the Universe during inflation.

- Quantum fluctuations of a generic scalar field in a quasi-de Sitter stage (Bartolo et al. 2004a);

  so far, we have analyzed the time evolution of the quantum fluctuations of a generic scalar field χ assuming that the scale-factor evolves like in a pure de Sitter expansion, $a(\tau) = -1/(H\tau)$. However, during Inflation the Hubble rate is not exactly constant, but changes with time as $\dot{H} = -\epsilon H^2$ (quasi-de Sitter expansion). It is possible to show that all the results obtained so far, and in the next subsections, are still valid if we expands all the solutions to the lowest order in η_χ and the inflationary parameter $|\epsilon| \ll 1$.

2.2.2 Power spectrum

As we saw in the previous section, in the simplest model of inflation, the primordial perturbation field is Gaussian. That means that the field is entirely characterized by its *power spectrum*. For a given random field $f(t, \mathbf{x})$ which can be expanded in Fourier space (since we work in flat space) as

$$f(t, \mathbf{x}) = \int \frac{d^3\mathbf{k}}{(2\pi)^{3/2}} e^{i\mathbf{k}\cdot\mathbf{x}} f_{\mathbf{k}}(t) \,, \tag{2.58}$$

the (dimensionless) power-spectrum $\mathcal{P}_f(k)$ can be defined as

$$\left\langle f_{\mathbf{k_1}} f^*_{\mathbf{k_2}} \right\rangle \equiv \frac{2\pi^2}{k^3}\mathcal{P}_f(k)\delta^{(3)}(\mathbf{k_1}-\mathbf{k_2}) \,, \tag{2.59}$$

where the angled brackets denote ensemble averages. This particular definition of power spectrum is clearly understandable when we consider the mean square value of $f(t,\mathbf{x})$ in real space

$$\left\langle f^2(t,\mathbf{x}) \right\rangle = \int \frac{dk}{k}\mathcal{P}_f(k) \,; \tag{2.60}$$

thus, according with the (dimensionless) power spectrum definition, $\mathcal{P}_f(k)$ is the contribution to the variance per unit logarithmic interval in the wavenumber k. For a scalar field χ, combining Eq. (2.35) and (2.37) the power spectrum can be evaluated with

$$\left\langle \delta\chi_{\mathbf{k_1}} \delta\chi^*_{\mathbf{k_2}} \right\rangle \equiv \frac{|u_k|^2}{a^2}\mathcal{P}_f(k)\delta^{(3)}(\mathbf{k_1}-\mathbf{k_2}) \,, \tag{2.61}$$

giving the expression ($\delta\chi_k \equiv u_k/a$)

$$\mathcal{P}_{\delta\chi}(k) = \frac{k^3}{2\pi^2}|\delta\chi_k|^2 \,. \tag{2.62}$$

Finally, in the case of the previous subsection, de Sitter phase with light scalar

field, the power spectrum on superhorizon scales is given by

$$\mathcal{P}_{\delta\chi}(k) = \left(\frac{H}{2\pi}\right)^2 \left(\frac{k}{aH}\right)^{3-2\nu_\chi} . \tag{2.63}$$

Another fundamental quantity connected to the power spectrum is the *spectral index* $n_f(k)$, defined as

$$n_f(k) - 1 \equiv \frac{d\ln \mathcal{P}_f}{d\ln k} . \tag{2.64}$$

It is clear from this definition that a spectral index equal to one means a *scale-invariant* power spectrum. In fact, if we combine this equation with the power spectrum in Eq. (2.63) we obtain

$$n_{\delta\chi} - 1 = 3 - 2\nu_\chi = 2\eta_\chi \ll 1 , \tag{2.65}$$

that slightly deviates from unity in the case of light scalar field and is exactly unity for massless scalar field.

To conclude this subsection, a little comment about notation. The (dimensionless) power spectrum $\mathcal{P}_f(k)$ is standard notation in the inflationary literature whereas an alternative definition is used in different fields and in the following chapters. The relation between the two notation is

$$P_f(k) = \frac{2\pi^2}{k^3}\mathcal{P}_f(k)\,. \tag{2.66}$$

In the next subsection we return to the inflationary field ϕ and see how the formalism we developed works for this specific case. In particular, we will provide the link between fluctuations of the scalar field and CMB.

2.2.3 Linear Perturbation Theory in Inflation

In the previous sections, we studied the fluctuations of a generic scalar field. We also mentioned how the perturbations, produce primordial fluctuations from the quantum to classical transition of perturbations on super-horizon scales, re-entering the horizon after inflation. These perturbations set the initial conditions and are in turn the seeds of CMB anisotropies. In this subsection the most important motivation for inflationary models, the creation of linear perturbation due to the inflationary scalar field, is discussed. Let us start from a linearly perturbed conformal LFRW metric of the form (Komatsu 2002),

$$\begin{aligned} ds^2 = a^2(\tau)\Big\{&-(1+2AQ)\,d\tau^2 - 2BQ_i d\tau dx^i + \\ &\Big[(1+2H_L Q)\,\delta_{ij} + 2H_T Q_{ij}\Big]dx^i dx^j\Big\}\,, \end{aligned} \tag{2.67}$$

where, all the metric perturbations A, B, H_L and H_T are $\ll 1$ and functions of τ. The spatial coordinate dependence of the perturbations is described by the scalar harmonic eigenfunctions, Q, Q_i and Q_{ij}, that satisfy $\delta^{ij}Q_{,ij} = -k^2 Q$, $Q_i = -k^{-1}Q_{,i}$, and $Q_{ij} = k^{-2}Q_{,ij} + (1/3)\delta_{ij}Q$. Note that Q_{ij} is traceless: $\delta^{ij}Q_{ij} = 0$. Perturbations

in the metric translate into perturbations into the stress-energy tensor δT^{μ}_{ν}. We expand a scalar field into its homogeneous mean field, $\phi(\tau)$, and fluctuations about the mean, $\delta\phi(\tau)Q(\mathbf{x})$. The energy density and pressure fluctuations are given by

$$\delta\rho_\phi Q \equiv -\delta T^0_0 = \left[a^{-2}\left(\phi'\delta\phi' - A\phi'^2\right) + V_{,\phi}\delta\phi\right] Q\,, \tag{2.68}$$

$$\delta p_\phi Q \equiv \delta T^k_k/3 = \left[a^{-2}\left(\phi'\delta\phi' - A\phi'^2\right) + V_{,\phi}\delta\phi\right] Q\,. \tag{2.69}$$

The energy flux, T^0_i, gives the velocity field, $v_\phi Q_i$,

$$(\rho_\phi + p_\phi)(v_\phi - B)Q_i \equiv T^0_i = \left(\frac{\phi'}{a^2}k\delta\phi\right) Q_i\,. \tag{2.70}$$

Using $\rho_\phi + p_\phi = a^{-2}\phi'^2$, we obtain $v_\phi - B = k\phi'^{-1}\delta\phi$; thus, $\delta\phi$ is responsible for the fluid's peculiar motion. The anisotropic stress, $T^i_j - p_\phi\delta^i_j$, is a second-order perturbation variable for a scalar field, being negligible.

Linear perturbations are affected by gauge freedom, i.e. the existence of reference frames characterized by linear coordinate shifts between each other

$$\tau \rightarrow \tau' = \tau + T(\tau)Q(\mathbf{x})\,, \tag{2.71}$$

$$x^i \rightarrow x'^i = x^i + L(\tau)Q_i(\mathbf{x})\,, \tag{2.72}$$

where T and L are $\ll 1$. So the scalar-field fluctuations transform as (attention to the difference between the $'$ as gauge transformation with respect to $'$ as conformal time derivative)

$$\delta\phi(\tau) \rightarrow \tilde{\delta\phi}(\tau') = \delta\phi(\tau) - \phi'(\tau)T(\tau)\,. \tag{2.73}$$

Then if we choose $T = \phi'^{-1}\delta\phi$ we obtain comoving gauge results $\delta\tilde{\phi} = 0$ (from now on $'$ is again the derivatives with respect to the conformal time).

Following Komatsu (2002) we choose the *comoving* gauge so that $B \equiv v_\phi$ (a fluid element is comoving with the origin of the spatial coordinate). In this particular gauge the scalar-field fluctuations can be written as $\delta\phi_{\rm com} \equiv 0$. As a last note, since we have only one degree of freedom, a scalar field, in the system, $\delta\rho_\phi$, δp_ϕ, and v_ϕ are not independent of each other.

Let us start perturbing the Ricci scalar, R:

$$\delta^{(3)}R = a^{-2}k^2\mathcal{R}Q \,, \tag{2.74}$$

$$\mathcal{R} \equiv H_L + (1/3)H_T \,. \tag{2.75}$$

So, $\mathcal{R}$ represents perturbations in the intrinsic spatial curvature. The definition of $\mathcal{R}$ enters in the definition of the *gauge-invariant* variable (see Bardeen et al. 1983; Komatsu 2002)

$$\zeta \equiv \mathcal{R} - \frac{aH}{\phi'}\delta\phi \,, \tag{2.76}$$

that reduces to $\mathcal{R}$ in the comoving gauge, or to $-(aH/\phi')\delta\phi$ in the spatially flat gauge ($\mathcal{R} = 0$). This variable helps our perturbation analysis not only because of being gauge invariant, but also being *conserved*, that is, it remains constant in time on super-horizon scales (Komatsu 2002).

Using the gauge invariance property of ζ, i.e. $\zeta_{\rm com} = \zeta_{\rm flat}$, we obtain a relation between $\delta\phi$ in the spatially flat gauge, $\delta\phi_{\rm flat}$, and $\mathcal{R}$ in the comoving gauge, $\mathcal{R}_{\rm com}$, as

$$\mathcal{R}_{\rm com} = -\frac{aH}{\phi'}\delta\phi_{\rm flat} = \zeta_{\rm com} \ . \tag{2.77}$$

This formula provides the link between the scalar field and metric perturbations.

As we have seen in the previous section, $\delta\phi$ obeys Gaussian statistics to very good accuracy because of the central limit theorem, that is, $\delta\phi$ is the sum of the nearly infinite number of independent modes Eq. (2.52). Since $\zeta_{\rm com}$ is linearly related to $\delta\phi_{\rm flat}$, then $\zeta_{\rm com}$ also obeys Gaussian statistics in the linear order; however, as we will show later, a significant number of inflationary models beyond standard single field slow-roll, predict significant non-linear corrections that makes $\zeta_{\rm com}$ non-Gaussian.

2.2.4 Generation of primary CMB anisotropy on large scales

The metric perturbations are the seeds for CMB anisotropies on the sky. The anisotropies of the CMB are generated from the interaction between baryons and photons. To understand the generation and evolutions of those interactions, we should solve the full Boltzmann equations of the various components of the Universe. This is beyond the scope of this chapter (a good reference for the generations of CMB anisotropies is Dodelson (2003)). The important point is that, the initial conditions of the Boltzmann equations can all be related to the primordial gravitational potential Φ. The relation between the gravitational potential and the metric perturbations at large scales is called *Sachs-Wolfe effect* and is showed in this subsection.

To relate those anisotropies to the gauge-invariant perturbation, ζ, we must introduce a new gauge-invariant variable, Φ (see Bardeen (1980)), which reduces

to $\mathcal{R}$ in the Newtonian gauge, in which $B \equiv 0 \equiv H_T$. The definition of this variable is

$$\Phi \equiv \mathcal{R} - \frac{aH}{k}\left(-B + \frac{H_T'}{k}\right) . \tag{2.78}$$

Here, the terms in the parenthesis represent the shear, or the anisotropic expansion rate, of the τ = constant hypersurfaces. While Φ represents the curvature perturbations in the zero-shear gauge, it also represents the shear in the spatially flat gauge in which $\mathcal{R} \equiv 0$. Using Φ, we may write ζ as

$$\zeta = \mathcal{R} - \frac{aH}{\phi'}\delta\phi = \Phi - \frac{aH}{k}\left(v_\phi - \frac{H_T'}{k}\right) , \tag{2.79}$$

where the terms in the parenthesis represent the gauge-invariant fluid velocity.

The general relativistic cosmological linear perturbation theory gives the evolution of Φ on super-horizon scales for adiabatic perturbations (Dodelson 2003; Kodama and Sasaki 1984),

$$\Phi = \frac{3 + 3w}{5 + 3w}\zeta , \tag{2.80}$$

where $w = p/\rho$, and hence $\Phi = (2/3)\zeta$ in the radiation era ($w = 1/3$), and $\Phi = (3/5)\zeta$ in the matter era ($w = 0$).

The potential Φ then perturbs the CMB through the so-called Sachs-Wolfe effect (Sachs and Wolfe 1967). The gravitational effects of density perturbations on the potential Φ generates temperature fluctuations

$$\frac{\Delta T}{T} = -\frac{1}{3}\Phi , \tag{2.81}$$

in the simplest case of adiabatic fluctuations in a matter dominated universe. A simple and pedagogic derivation of this effect can be found on White and Hu (1997). We start from the geodesic equation for photons propagating in a metric perturbed by a gravitational potential Φ. The resulting frequency shifts for the CMB photons lead to a temperature perturbation

$$\left.\frac{\Delta T}{T}\right|_f = \left.\frac{\Delta T}{T}\right|_i - \Phi_i \,, \tag{2.82}$$

where i and f refer to "initial" and "final" states. We have dropped the term due to the local gravitational potential (Φ_f) which gives an isotropic temperature shift. We also neglect the Doppler shift from the relative motion of the emitter and receiver and other small scale effects, and assume that the potentials are constant on large scales. The first term of Eq. (2.82) on the right-hand side is the "intrinsic" temperature perturbation at early times. It can be shown that this term is $(\Delta T/T)_i = \{2/[3(1+w)]\}\Phi$ and that, in a matter dominated Universe, is equal to $(\Delta T/T)_i = (2/3)\Phi$. The second term of Eq. (2.82) indicates the energy lost when the photon climbs out of a potential well (redshift). For adiabatic fluctuations, the coefficient which relates the large-angle CMB temperature fluctuations to the gravitational potential, that is Eq. (2.81), comes about by a partial cancellation of two terms: the intrinsic temperature perturbation and the gravitational redshift from climbing out of a potential. The latter wins, meaning that photon over-densities are CMB cold spots.

Thus using the Sachs-Wolfe effect we can relate the gauge-invariant potentials Φ and ζ with the large scale fluctuations

$$\frac{\Delta T}{T} = -\frac{1}{3}\Phi = -\frac{1}{5}\zeta \ . \tag{2.83}$$

In this section we have then shown how primordial perturbations are transferred to CMB anisotropies on super-horizon scales. This last relation is important because tell us that any primordial NG will be transferred to the CMB even at linear order. And, if using the second-order gravitational perturbation theory, $\Delta T/T = -(1/3)\Phi + O(\Phi^2)$, then even if Φ is Gaussian, ΔT becomes weakly non-Gaussian.

2.2.5 Non-linear perturbations in Inflation

In this subsection, we will finally give a prediction for NG in the case of standard single field slow-roll inflation, and show explicitly that it is small.

Suppose that ζ is an arbitrary function of a scalar field: $\zeta = f(\phi)$. By perturbing ϕ as $\phi = \phi_0 + \delta\phi_{\rm flat}$, where $\delta\phi_{\rm flat}$ is a scalar field fluctuation in the spatially flat gauge ($\mathcal{R}_{\rm flat} \equiv 0$), we have

$$\begin{aligned} \zeta &= f(\phi_0 + \delta\phi_{\rm flat}) \\ &= f(\phi_0) + \left(\frac{\partial f}{\partial \phi}\right)\delta\phi_{\rm flat} + \frac{1}{2}\left(\frac{\partial^2 f}{\partial \phi^2}\right)\delta\phi^2_{\rm flat} + O\left(\delta\phi^3_{\rm flat}\right) \ . \end{aligned} \tag{2.84}$$

By comparing this equation with the linear-perturbation results $\zeta = -(aH/\phi')\delta\phi_{\rm flat}$, we find $f(\phi_0) = 0$, $\partial f/\partial\phi = -(aH/\phi')$,

$$\zeta = -\frac{aH}{\phi'}\delta\phi_{\rm flat} - \frac{1}{2}\frac{\partial}{\partial\phi}\left(\frac{aH}{\phi'}\right)\delta\phi^2_{\rm flat} + O\left(\delta\phi^3_{\rm flat}\right) \ ; \tag{2.85}$$

thus, even if $\delta\phi_{\rm flat}$ is exactly Gaussian ζ becomes weakly non-Gaussian because of $\delta\phi^2_{\rm flat}$ or the higher-order terms.

We have shown that non-linearity in inflation creates weakly non-Gaussian curvature perturbations outside the horizon from Gaussian quantum fluctuations inside the horizon. By expanding the non-linear relation between ζ and $\delta\phi_{\rm flat}$ up to the second order, we obtain a non-linear curvature perturbation, $\zeta = \zeta^{\rm L} + \zeta^{\rm NL}$, where

$$\zeta^{\rm L} \equiv -\frac{aH}{\phi'}\delta\phi_{\rm flat}\,, \tag{2.86}$$

$$\zeta^{\rm NL} \equiv -\frac{1}{2}\left[\frac{\partial}{\partial\phi}\left(\frac{aH}{\phi'}\right)\right]\left(\frac{\phi'}{aH}\right)^2\left(\zeta^{\rm L}\right)^2\,. \tag{2.87}$$

Using the Sachs-Wolfe effect we already know that the gauge-invariant primordial potential $\Phi = \Phi_{\rm L} + \Phi_{\rm NL}$ is $(2/3)\zeta^{\rm L,NL}$ in the radiation era and $(3/5)\zeta^{\rm L,NL}$ in the matter era.

In the following chapters, we will focus on measuring $\Phi_{\rm NL}$ using non-Gaussian CMB temperature fluctuations. We will see that the NG is parametrized by different "non-linearity parameters", referred as $f_{\rm NL}$ (Babich et al. 2004; Gangui et al. 1994; Komatsu and Spergel 2001; Wang and Kamionkowski 2000), a dimensionless parameter measuring the amplitude of NG. For the moment, let focus on the most natural parametrization for the amplitude of $\Phi_{\rm NL}$. This parametrization is called "local" NG (Gangui et al. 1994; Komatsu and Spergel 2001; Verde et al. 2000; Wang and Kamionkowski 2000), because it depends locally on the space $\mathbf{x}$ (both sides of the following equation are evaluated at the same location in real space), and is written as

$$\Phi_{\rm NL}(\mathbf{x}) = f_{\rm NL}^{\rm local}\left[\Phi_{\rm L}^2(\mathbf{x}) - \left\langle\Phi_{\rm L}^2(\mathbf{x})\right\rangle\right] . \tag{2.88}$$

We can directly write from Eq. (2.87)

$$f_{\rm NL}^{\rm local} = -\frac{5}{3}\frac{1}{2}\left[\frac{\partial}{\partial\phi}\left(\frac{aH}{\phi'}\right)\right]\left(\frac{\phi'}{aH}\right)^2 . \tag{2.89}$$

In the case of slow-roll inflation with a power-law potential $V(\phi) \propto \phi^n$ we can calculate directly the value of $f_{\rm NL}^{\rm local}$. Using Eqs. (2.26), (2.27), (2.22) and (2.23) we obtain

$$\begin{aligned} f_{\rm NL}^{\rm local} &= \frac{5}{6}\frac{\partial}{\partial\phi}\left[3\,\frac{V}{3M_{\rm Pl}^2}\left(\frac{\partial V}{\partial\phi}\right)^{-1}\right]\frac{M_{\rm Pl}^4}{V^2}\left(\frac{\partial V}{\partial\phi}\right)^2 , \\ &= \frac{5}{6}M_{\rm Pl}^2\left[1 - V^2\left(\frac{\partial V}{\partial\phi}\right)^{-2}\frac{1}{V}\frac{\partial^2 V}{\partial\phi^2}\right]\frac{1}{V^2}\left(\frac{\partial V}{\partial\phi}\right)^2 , \\ &\simeq \frac{5}{6}M_{\rm Pl}^2\left[1 - \frac{M_{\rm Pl}^2}{2\epsilon}\frac{\eta}{M_{\rm Pl}^2}\right]\frac{2\epsilon}{M_{\rm Pl}^2} , \\ &= O(\epsilon) , \end{aligned} \tag{2.90}$$

where we used $1 - \eta/2\epsilon = O(1)$. This results implies that $f_{\rm NL}^{\rm local} \ll 1$. Local type NG is then the general prediction of standard single field slow-roll inflation. However, this value is undetectable from CMB experiments as showed in (Komatsu 2002).

2.3 Parametrization of non-Gaussianity

If the primordial fluctuations are Gaussian-distributed, then they are completely characterised by their two-point correlation function, or equivalently, their power spectrum. If they are non-Gaussian, there is additional statistical information in the higher-order correlation functions, which is not captured by the two-point correlation function. In particular, the 3-point correlation function, or its Fourier counterpart, the *bispectrum*, is important because it is the lowest-order statistic that can distinguish between Gaussian and non-Gaussian perturbations. One of the main goals of this thesis is to constrain the amplitude and shape of primordial NG using the angular bispectrum of the CMB anisotropies. The CMB angular bispectrum is related to the primordial bispectrum defined by

$$\langle \Phi(\vec{k}_1)\Phi(\vec{k}_2)\Phi(\vec{k}_3)\rangle = (2\pi)^3\delta^{(3)}(\vec{k}_1+\vec{k}_2+\vec{k}_3)B_\Phi(k_1,k_2,k_3), \tag{2.91}$$

where the 3d Dirac delta functions enforce the triangle conditions of the three $\vec{k}$ modes, due to the assumed translational and rotational invariance. The bispectrum $B_\Phi(k_1,k_2,k_3)$ measures the correlation among three perturbation modes. Assuming translational and rotational invariance, it depends only on the magnitudes of the three wavevectors. In general the bispectrum can be written as

$$B_\Phi(k_1,k_2,k_3) = f_{\rm NL}F(k_1,k_2,k_3)\,. \tag{2.92}$$

The bispectrum is measured by sampling triangles in Fourier space. The dependence of the function $F(k_1,k_2,k_3)$ on the type of triangle (i.e., the configuration) formed by the three wavevectors describes the *shape* of the bispectrum (Babich et al.

2004), which encodes lots of physical information. It can also encodes the scale dependence, i.e., the *running*, of the bispectrum (Chen 2005).[3] Different NG shapes are linked to distinctive physical mechanisms that can generate such non-Gaussian fingerprints in the early Universe. For example, the so-called "local" NG is characterized by a signal that is maximal for "squeezed" triangles with $k_1 \ll k_2 \simeq k_3$ (or permutations; Maldacena 2003) which occurs, in general, when the primordial NG is generated on super-horizon scales. Conversely, "equilateral" NG (Babich et al. 2004) peaks for equilateral configurations $k_1 \approx k_2 \approx k_3$, due to correlations between fluctuation modes that are of comparable wavelengths, which can occur if the three perturbation modes mostly interact when they cross the horizon approximately at the same time. Other relevant shape is the "orthogonal" NG (Senatore et al. 2010) that generates a signal with a positive peak at the equilateral configuration and a negative peak at the folded configuration.

2.3.1 Inflationary models for primordial non-Gaussianity

There is a simple reason why standard single-field models of slow-roll inflation predict a tiny level of NG, of the order of the usual slow-roll parameters $f_{\rm NL} \sim O(\epsilon, \eta)$:[4] in order to achieve an accelerated period of expansion, the infla-

[3] Specifically, one can define the shape of the bispectrum as the dependence of $F(k_1, k_2, k_3)(k_1 k_2 k_3)^2$ on the ratios of momenta, e.g., (k_2/k_1) and (k_3/k_1), once the overall scale of the triangle $K = k_1 + k_2 + k_3$ is fixed. The scale dependence of the bispectrum can be characterized by the dependence of $F(k_1, k_2, k_3)(k_1 k_2 k_3)^2$ on the overall scale K, once the ratios (k_2/k_1) and (k_3/k_1) are fixed (see, e.g., Chen 2010).

[4] This has been shown in the pioneering research which demonstrated that perturbations produced in single-field models of slow-roll inflation are characterized by a low-amplitude NG (Falk et al. 1993; Gangui et al. 1994; Salopek and Bond 1990). Later Acquaviva et al. (2003) and Maldacena (2003) obtained a complete quantitative prediction for the nonlinearity parameter in single-field slow-roll inflation models, also showing that the predicted NG is characterized by a shape dependence which is more complex than suggested by previous results expressed in terms of the simple parameterization $\Phi(\vec{x}) = \Phi_{\rm L}(\vec{x}) + f_{\rm NL}\Phi^2_{\rm L}(\vec{x})$ (Gangui et al. 1994; Komatsu and Spergel

ton potential must be very flat, thus suppressing the inflaton (self-)interactions and any source of nonlinearity, and leaving only its weak gravitational interactions as the main source of NG. This fact leads to a clear distinction between the simplest models of inflation, and scenarios where a significant amplitude of NG can be generated (e.g., Komatsu 2010), as follows. The simplest inflationary models are based on a set of minimal conditions:

(i) a single weakly-coupled neutral single scalar field (the *inflaton*, which drives inflation and generates the curvature perturbations);

(ii) with a canonical kinetic term;

(iii) slowly rolling down its (featureless) potential;

(iv) initially lying in a Bunch-Davies (ground) vacuum state.

In the last few years, an important theoretical realization has taken place: a detectable amplitude of NG with specific triangular configurations (corresponding broadly to well-motivated classes of physical models) can be generated if any one of the above conditions is violated (Bartolo et al. 2004b; Chen 2010; Komatsu 2010; Liguori et al. 2010; Yadav and Wandelt 2010):

- "local" NG, where the signal peaks in "squeezed" triangles ($k_1 \ll k_2 \simeq k_3$) (e.g., multi-field models of inflation);

- "equilateral" NG, peaking for $k_1 \approx k_2 \approx k_3$. Examples of this class include single-field models with non-canonical kinetic term (Chen et al. 2007), such as k-inflation (Armendariz-Picon et al. 1999; Chen et al. 2007) or Dirac-Born-Infield (DBI) inflation (Alishahiha et al. 2004; Silverstein and Tong 2001; Verde et al. 2000; Wang and Kamionkowski 2000).

2004), models characterized by more general higher-derivative interactions of the inflaton field, such as ghost inflation (Arkani-Hamed et al. 2004), and models arising from effective field theories (Cheung et al. 2008);

- "orthogonal" NG which is generated, e.g., in single-field models of inflation with a non-canonical kinetic term (Senatore et al. 2010), or with general higher-derivative interactions.

It is then clear that, detecting primordial NG with given shape would have major consequences on our understanding of inflation, as it would select one of the "scenarios" above, thus strongly discriminating between models. A detection of large $f_{\rm NL}$ signal would rule out the simplest models of single-field inflation, which, obeying *all* the conditions above, are characterized by weak gravitational interactions with $|f_{\rm NL}| \ll 1$.

The above scheme provides a general classification of inflationary models in terms of the corresponding NG shapes, which we adopt for the data analysis presented in this theses:

1. "general" single-field inflationary models (tested using the equilateral and orthogonal shapes);

2. multi-field models of inflation (tested using the local shape).

In each class, there exists specific realizations of inflationary models which generate a specific NG shape. We will investigate these classes of inflationary models by constraining the corresponding NG content, focusing on amplitudes and shapes. Different NG shapes are observationally distinguishable if their cross-correlation is sufficiently low; almost all of the shapes analysed in this thesis are

highly orthogonal to each other (e.g., Babich et al. 2004; Fergusson and Shellard 2007).

There are exceptional cases which evade this classification but will be not discussed in this thesis.

2.3.2 General single-field models of inflation

In this subsection we will comment on models that can generate large NG. Typically in models with a non-standard kinetic term (or more general higher-derivative interactions), inflaton perturbations propagate with an effective sound speed c_s which can be smaller than the speed of light, and this results in a contribution to the NG amplitude $f_{\rm NL} \sim c_{\rm s}^{-2}$ in the limit $c_{\rm s} \ll 1$. Equilateral NG is usually generated by derivative interactions of the inflaton field; derivative terms are suppressed when one perturbation mode is frozen on super-horizon scales during inflation, and the other two are still crossing the horizon, so that the correlation between the three perturbation modes will be suppressed, while it is maximal when all the three modes cross the horizon at the same time, which happens for $k_1 \approx k_2 \approx k_3$. The local and equilateral forms are nearly orthogonal to each other, which means that both can be measured nearly independently.

The equilateral type NG is well approximated by the template (Creminelli et al.

2006)

$$B_{\Phi}^{\rm equil}(k_1,k_2,k_3) = 6A^2 f_{\rm NL}^{\rm equil} \times \left\{ -\frac{1}{k_1^{4-n_{\rm s}}k_2^{4-n_{\rm s}}} - \frac{1}{k_2^{4-n_{\rm s}}k_3^{4-n_{\rm s}}} - \frac{1}{k_3^{4-n_{\rm s}}k_1^{4-n_{\rm s}}} - \frac{2}{(k_1k_2k_3)^{2(4-n_{\rm s})/3}} + \left[\frac{1}{k_1^{(4-n_{\rm s})/3}k_2^{2(4-n_{\rm s})/3}k_3^{4-n_{\rm s}}} + (5 \text{ permutations}) \right] \right\} , \quad (2.93)$$

where $P_{\Phi}(k) = A/k^{4-n_{\rm s}}$ is the power spectrum of Bardeen's gravitational potential with normalization A and scalar spectral index $n_{\rm s}$. For example, the models introduced in the string theory framework based on the DBI action (Alishahiha et al. 2004; Silverstein and Tong 2004) give rise to an equilateral NG with an overall amplitude $f_{\rm NL}^{\rm equil} = -(35/108)c_{\rm s}^{-2}$ for $c_{\rm s} \ll 1$, which turns out typically to be $f_{\rm NL}^{\rm equil} < -5$. [5]

The equilateral shape emerges also in models characterized by more general higher-derivative interactions, such as ghost inflation (Arkani-Hamed et al. 2004) or models within effective field theories of inflation (Bartolo et al. 2010; Cheung et al. 2008; Senatore et al. 2010).

Using an effective field theory approach to inflationary perturbations (Cheung et al. 2008), it has been shown that it is possible to build a linear combination of higher-derivative scalar-field interaction terms, each of which yields forms similar to the equilateral shape. This combination generate a bispectrum that is orthogonal to the equilateral (and local) one, the so-called "orthogonal" shape. This can be

[5] An effectively single-field model with a non-standard kinetic term and a reduced sound speed for the adiabatic perturbation modes might also arise in coupled multi-field systems, where the heavy fields are integrated out: see discussions in, e.g., Achúcarro et al. (2011); Shiu and Xu (2011); Tolley and Wyman (2010).

approximated by the template, from Senatore et al. (2010):

$$
\begin{aligned}
& B_{\Phi}^{\rm ortho}(k_1,k_2,k_3) = 6A^2 f_{\rm NL}^{\rm ortho} \\
\times & \left\{ -\frac{3}{k_1^{4-n_{\rm s}}k_2^{4-n_{\rm s}}} - \frac{3}{k_2^{4-n_{\rm s}}k_3^{4-n_{\rm s}}} - \frac{3}{k_3^{4-n_{\rm s}}k_1^{4-n_{\rm s}}} \right. \\
& -\frac{8}{(k_1k_2k_3)^{2(4-n_{\rm s})/3}} + \left[\frac{3}{k_1^{(4-n_{\rm s})/3}k_2^{2(4-n_{\rm s})/3}k_3^{4-n_{\rm s}}} \right. \\
& \left. \left. +(5 \text{ perm.}) \right] \right\} . \qquad (2.94)
\end{aligned}
$$

The orthogonal form, has a positive peak at the equilateral configuration, and a negative valley along the elongated configurations ($k_1 = k_2 + k_3$). The orthogonal bispectrum can also arise as the predominant shape in some inflationary realizations of Galileon inflation (Renaux-Petel et al. 2011).

2.3.3 Multi-field models

This class of models generally includes an additional light scalar field (or more fields) during inflation, which can be different from the inflaton, and whose fluctuations contribute to the final primordial curvature perturbation of the gravitational potential. It could be the case of inflation driven by several scalar fields – "multiple-field inflation" – or the one where the inflaton drives the accelerated expansion, while other scalar fields remain subdominant during inflation. This encompasses, for instance, a large class of multi-field models which leads to non-Gaussian isocurvature perturbations (for early works, see e.g., Linde and Mukhanov 1997, Peebles 1997, Bucher and Zhu 1997). More importantly, such models can also lead to cross-correlated and non-Gaussian adiabatic and isocurvature modes,

where NG is first generated by large nonlinearities in some scalar (possibly non-inflatonic) sector of the theory, and then efficiently transferred to the inflaton adiabatic sector(s) through the cross-correlation of adiabatic and isocurvature perturbations[6] (Bartolo et al. 2002; Bernardeau and Uzan 2002; Lyth and Rodriguez 2005; Rigopoulos et al. 2006, 2007; Tzavara and van Tent 2011; Vernizzi and Wands 2006; for a review on NG from multiple-field inflation models, see, Byrnes and Choi 2010). Another interesting possibility is the curvaton model (Enqvist and Sloth 2002; Lyth and Wands 2002; Mollerach 1990; Moroi and Takahashi 2001), where a second light scalar field, subdominant during inflation, decays after inflation ends, producing the primordial density perturbations which can be characterized by a high NG level (e.g., Bartolo et al. 2004c; Lyth and Wands 2002; Lyth et al. 2003). NG in the curvature perturbation can be generated at the end of inflation, e.g., due to the nonlinear dynamics of (p)reheating (e.g., Barnaby and Cline 2006; Chambers and Rajantie 2008; Enqvist et al. 2005; see also Bond et al. 2009) or, as in modulated (p)reheating and modulated hybrid inflation, due to local fluctuations in the decay rate/interactions of the inflaton field (Bernardeau et al. 2004; Cicoli et al. 2012; Dvali et al. 2004a,b; Kofman 2003; Kolb et al. 2006; Lyth 2005; Lyth and Riotto 2006; Salem 2005; Zaldarriaga 2004). The common feature of all these models is that a large NG in the curvature perturbation can be produced via both a transfer of super-horizon non-Gaussian isocurvature perturbations in the second field (not necessarily the inflaton) to the adiabatic density perturbations, and via additional nonlinearities in the transfer mechanism. Since, typically, this

[6]This may happen, for instance, if the inflaton field is coupled to the other scalar degrees of freedom, as expected on particle physics grounds. These scalar degrees of freedom may have large self-interactions, so that their quantum fluctuations are intrinsically non-Gaussian, because, unlike the inflaton case, the self-interaction strength in such an extra scalar sector does not suffer from the usual slow-roll conditions.

process occurs on super-horizon scales, the form of NG is local in real space. Being local in real space, the bispectrum correlates large and small scale Fourier modes. The local bispectrum is given by (Falk et al. 1993; Gangui et al. 1994; Komatsu and Spergel 2001; Verde et al. 2000; Wang and Kamionkowski 2000)

$$\begin{aligned} B_{\Phi}^{\rm local}(k_1,k_2,k_3) &= 2f_{\rm NL}^{\rm local}\Big[P_{\Phi}(k_1)P_{\Phi}(k_2)+P_{\Phi}(k_1)P_{\Phi}(k_3) \\ &+ P_{\Phi}(k_2)P_{\Phi}(k_3)\Big] \\ &= 2A^2 f_{\rm NL}^{\rm local}\left[\frac{1}{k_1^{4-n_{\rm s}}k_2^{4-n_{\rm s}}}+{\rm cycl.}\right]. \end{aligned} \tag{2.95}$$

Most of the signal-to-noise ratio in fact peaks in the squeezed configurations ($k_1 \ll k_2 \simeq k_3$)

$$B_{\Phi}^{\rm local}(k_1\to 0,k_2,k_3)\to 4f_{\rm NL}^{\rm local}P_{\Phi}(k_1)P_{\Phi}(k_2)\,. \tag{2.96}$$

The typical example of a curvature perturbation that generates the bispectrum of Eq. (2.95) is the standard local form for the gravitational potential (Gangui et al. 1994; Hodges et al. 1990; Kofman et al. 1991; Komatsu and Spergel 2001; Salopek and Bond 1990; Verde et al. 2000; Wang and Kamionkowski 2000)

$$\Phi(\vec{x}) = \Phi_L(\vec{x}) + f_{\rm NL}^{\rm local}(\Phi_L^2(\vec{x}) - \langle\Phi_L^2(\vec{x})\rangle)\,, \tag{2.97}$$

where $\Phi_L(\vec{x})$ is the linear Gaussian gravitational potential and $f_{\rm NL}^{\rm local}$ is the amplitude of a quadratic nonlinear correction (though this is not the only possibility: e.g., the gravitational potential produced in multiple-field inflation models generally cannot be reduced to the Eq. (2.97)). For example, in the (simplest) adiabatic curvaton models, the NG amplitude turns out to be (Bartolo et al. 2004c,d) $f_{\rm NL}^{\rm local} = (5/4r_{\rm D}) - 5r_{\rm D}/6 - 5/3$, for a quadratic potential of the cur-

vaton field (Lyth and Rodriguez 2005; Lyth and Wands 2002; Lyth et al. 2003; Sasaki et al. 2006), where $r_{\rm D} = [3\rho_{\rm curvaton}/(3\rho_{\rm curvaton} + 4\rho_{\rm radiation})]_{\rm D}$ is the "curvaton decay fraction" evaluated at the epoch of the curvaton (sudden approximated) decay. Therefore, for $r_{\rm D} \ll 1$, a high level of NG is imprinted.

There exists a clear distinction between multi-field and single-field models of inflation that can be probed via a consistency condition (Chen 2010; Chen et al. 2007; Creminelli and Zaldarriaga 2004; Maldacena 2003): in the squeezed limit, single-field models predict a bispectrum

$$B_{\Phi}^{\rm single-field}(k_1 \to 0, k_2, k_3 = k_2) \to \frac{5}{3}(1 - n_{\rm s})P_{\Phi}(k_1)P_{\Phi}(k_2)\,, \tag{2.98}$$

and thus $f_{\rm NL} \sim O(n_{\rm s} - 1)$ in the squeezed limit, in a model-independent sense (i.e., not only for standard single-field models). This means that a significant detection of local NG (in the squeezed limit) would rule out a very large class of single-field models of inflation (not just the simplest ones). Although based on very general conditions, the consistency condition of Eq. (2.98) can be violated in some well-motivated inflationary settings (we refer the reader to Chen (2010); Chen et al. (2013) and references therein for more details).

Chapter 3

The Planck experiment

The *Planck* satellite[1] (Planck Collaboration I 2011; Tauber et al. 2010) was launched on 14 May 2009, and has been scanning the sky stably and continuously since 12 August 2009. *Planck* carries a payload consisting of an array of 74 detectors sensitive to a range of frequencies between ~ 25 and ~ 1000 GHz, which scan the sky simultaneously and continuously with an angular resolution varying between ~30, at the lowest frequencies and, ~5 arcminutes at the highest. The array is arranged into two instruments. The detectors of the Low Frequency Instrument (LFI; Bersanelli et al. 2010; Mennella et al. 2011) are pseudo-correlation radiometers, covering three bands centred at 30, 44, and 70 GHz. The detectors of the High Frequency Instrument (HFI; Lamarre et al. 2010; Planck HFI Core Team 2011) are bolometers, covering six bands centred at 100, 143, 217, 353, 545 and 857 GHz. The design of *Planck* allows it to image the whole sky twice per year, with an combination of sensitivity, angular resolution, and frequency coverage

[1] *Planck (http://www.esa.int/Planck)* is a project of the European Space Agency – ESA – with instruments provided by two scientific consortia funded by ESA member states (in particular the lead countries: France and Italy) with contributions from NASA (USA), and telescope reflectors provided in a collaboration between ESA and a scientific consortium led and funded by Denmark.

never before achieved. The *Planck* satellite, its payload, and its performance as predicted at the time of launch, are described in 13 articles included in a special issue (Volume 520) of Astronomy & Astrophysics.

The main objective of *Planck*, defined in 1995, is to measure the anisotropies of the temperature of the CMB, with an accuracy set by fundamental astrophysical limits. Its level of performance was designed to enable *Planck* to extract essentially all the cosmological information embedded in the CMB temperature anisotropies. *Planck* was also designed to measure, with high accuracy, the polarization of the CMB anisotropies, which encodes not only a wealth of cosmological information, but also provides a unique probe of the early history of the Universe during the time when the first stars and galaxies formed. Finally, the *Planck* sky surveys produce a wealth of information on the properties of extragalactic sources and on the dust and gas in our own galaxy (see Fig. 3.1). The scientific objectives of *Planck* are described in detail in Planck Collaboration (2005). We discuss here just the main elements concerning this thesis. The results of the first year of observations (see Planck Collaboration I (2013)) include the work done in this thesis and will be discussed in the next chapters.

3.1 Generalities

Cosmology— A major goal of the *Planck* experiment is to determine with great precision the key cosmological parameters describing our Universe. A combination of high sensitivity, high angular resolution, and wide frequency coverage makes *Planck* ideal for this task. In particular, *Planck* is able to measure anisotropies on intermediate and small angular scales over the whole sky much

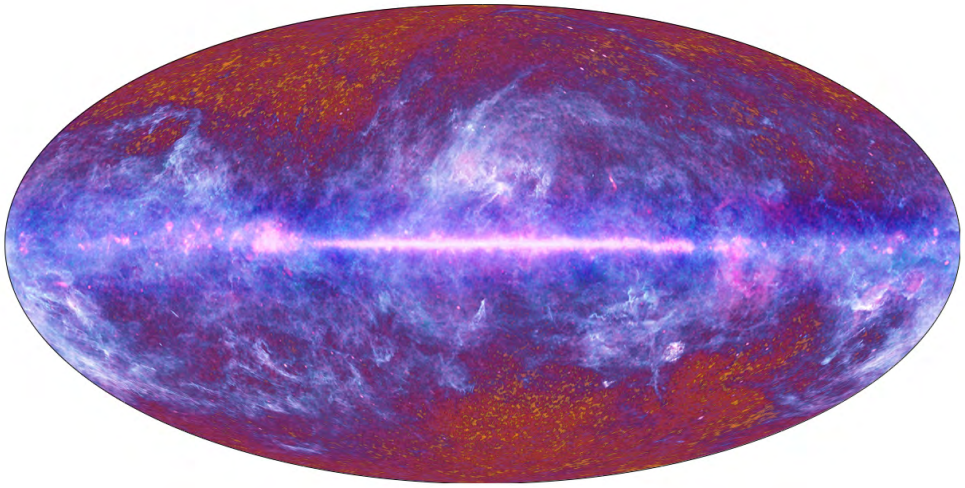

Figure 3.1: The image of the entire sky released by *Planck* in 2010 is a composite of all the data gathered over the first nine months of the mission, and illustrates artistically the multitude of Galactic, extragalactic, and cosmological components that contribute to the radiation detected by its payload.

more accurately than previous experiments. This translates directly into improved constraints on the main cosmological parameters, and the breaking of degeneracies between combinations of the others parameter. *Planck*'s sensitivity and angular resolution also make the analysis less reliant on supplementary astrophysical data than that of previous CMB experiments. *Planck*'s measurements of the cosmological parameters are presented and discussed in Planck Collaboration XVI (2013).

The Universe observed by *Planck* is well-fit by a six parameter ΛCDM model, and *Planck* provides strong constraints on deviations from this model. The values of key parameters in this model are summarized in Table 3.1. In some cases we find significant changes compared to previous measurement, as discussed in detail in Planck Collaboration XVI (2013).

Foregrounds— The astrophysical foregrounds measured by *Planck* represent an

Table 3.1: Cosmological parameter values for the *Planck*-only best-fit 6-parameter ΛCDM model (*Planck* temperature data plus lensing) and for the *Planck* best-fit cosmology including external data sets (*Planck* temperature data, lensing, *WMAP* polarization [WP] at low multipoles, high-ℓ experiments, and BAO, labelled [Planck+WP+highL+BAO] in Planck Collaboration XVI (2013)). Definitions and units for all parameters can be found in Planck Collaboration XVI (2013).

	Planck (CMB+lensing)		*Planck*+WP+highL+BAO	
Parameter	Best fit	68 % limits	Best fit	68 % limits
$\Omega_b h^2$	0.022242	0.02217 ± 0.00033	0.022161	0.02214 ± 0.00024
$\Omega_c h^2$	0.11805	0.1186 ± 0.0031	0.11889	0.1187 ± 0.0017
$100\theta_{MC}$	1.04150	1.04141 ± 0.00067	1.04148	1.04147 ± 0.00056
τ	0.0949	0.089 ± 0.032	0.0952	0.092 ± 0.013
n_s	0.9675	0.9635 ± 0.0094	0.9611	0.9608 ± 0.0054
$\ln(10^{10} A_s)$	3.098	3.085 ± 0.057	3.0973	3.091 ± 0.025
Ω_Λ	0.6964	0.693 ± 0.019	0.6914	0.692 ± 0.010
σ_8	0.8285	0.823 ± 0.018	0.8288	0.826 ± 0.012
z_{re}	11.45	$10.8^{+3.1}_{-2.5}$	11.52	11.3 ± 1.1
H_0	68.14	67.9 ± 1.5	67.77	67.80 ± 0.77
Age/Gyr	13.784	13.796 ± 0.058	13.7965	13.798 ± 0.037
$100\theta_*$	1.04164	1.04156 ± 0.00066	1.04163	1.04162 ± 0.00056
r_{drag}	147.74	147.70 ± 0.63	147.611	147.68 ± 0.45

entire area of science where the *Planck* data are relevant. Here we treat them as "contaminants", to be removed in order to get the CMB. The first foreground to be removed from the *Planck* frequency maps is compact and point-like sources, consisting mainly of extragalactic infrared and radio sources; the *Planck* collaboration released a catalogue of these sources (Planck Collaboration XXVIII 2013). In addition, the collaboration provided an all-sky catalogue of sources detected via the Sunyaev-Zeldovich (SZ) effect, which will become the reference for studies of SZ-detected galaxy clusters (Planck Collaboration XXIX 2013).

Seven types of unresolved foregrounds must be removed or controlled for CMB analysis: dust thermal emission; dust anomalous emission (Anomalous Microwave Emission (AME), likely due to spinning tiny grains); CO rotational emission lines (significant in at least three HFI bands); free-free emission; synchrotron emission; the cosmic infrared background (CIB); and SZ secondary CMB distortion. For cosmological purposes *Planck* achieves robust separation of the CMB from foregrounds using only *Planck* data with multiple independent methods. Other maps (e.g. masks) are released that use ancillary data in addition to the *Planck* data analysis purposes (Planck Collaboration XII 2013).

3.2 Instrumental highlights

Planck has an unprecedented combination of sensitivity, angular resolution, and frequency coverage. For example, the *Planck* detector array at 143 GHz has instantaneous sensitivity and angular resolution 25 and 3 times better, respectively, than the *WMAP* V band (Bennett et al. 2003; Hinshaw et al. 2012b). Considering the final mission durations (9 years for *WMAP*, 29 months for *Planck* HFI, and

an expected 50 months for *Planck* LFI), the white noise at map level is 12 times lower at 143 GHz for the same resolution. In harmonic space, the noise level in *Planck* power spectra is two orders of magnitude lower than *WMAP* at angular scales where beams are unimportant ($\ell < 700$ for *WMAP* and 2500 for *Planck*). *Planck* measures 2.6 times as many independnt ℓ's as *WMAP*, corresponding to 6.8 times as many independent modes (l, m) when comparing the same leading CMB channels for the two missions. This increase in angular resolution and sensitivity results in a large gain for analysis of CMB non-Gaussianity and cosmological parameters. In addition, *Planck* has a large overlap in ℓ with the high resolution ground-based experiments Acatama Cosmology Telescope, ACT, (Sievers et al. 2013) and South Pole Telescope, SPT, (Keisler et al. 2011). The noise spectra of SPT and *Planck* cross at around $\ell \sim 2000$, allowing an excellent check of the relative calibrations and transfer functions.

Increased sensitivity places *Planck* in a new position in the CMB framework. Earlier satellites *COBE* / DMR (Smoot et al. 1992) and *WMAP* (Bennett et al. 2012a) experiments, were limited by detector noise more than by systematic effects and foregrounds. Recent ground-based and balloon-borne experiments (e.g., ACT (Kosowsky 2003), SPT (Ruhl et al. 2004), SPIDER (Fraisse et al. 2011), the E and B EXperiment, EBEX, (Reichborn-Kjennerud et al. 2010)), have far larger numbers of detectors and higher angular resolution than *Planck* but can survey only a fraction of the sky over a limited frequency range. They are therefore sensitive to foregrounds and forced to analyse the "cleanest" regions of the sky. Considering the impact of cosmic variance, Galactic foregrounds turned out not to be a serious limitation for CMB temperature-based cosmology at the largest spatial scales over a limited part (<0.5) of the sky. Diffuse Galactic emissions have

steep frequency and angular spectra, and are very bright at frequencies below 70 and above 143 GHz at low multipoles in the angular domain. At small angular scales, extragalactic foregrounds such as unresolved compact sources (including the SZ effect from galaxy clusters and diffuse hot gas) and the correlated CIB, become important and cannot be ignored when carrying out CMB cosmology studies. *Planck*'s all-sky wide-frequency coverage becomes a key factor in this context, allowing it to measure these foregrounds and remove them to below intrinsic detector noise levels, but the contribution of higher resolution experiments to resolve foregrounds is also very important.

When detector noise is very low, systematic effects that arise from the instrument, telescope, scanning strategy, or calibration approach may dominate over noise in specific spatial, frequency, and/or ℓ ranges. The analysis of redundancy is the main tool used by *Planck* to understand and quantify the effect of systematics. Redundancy on short timescales comes from the scanning strategy — spinning at 1 rpm with the spin axis fixed for 45–80 minutes, depending on phase in the year — which has particular advantages in this respect, especially for the largest scales. When first designed, this strategy was considered ambitious because it required low $1/f$ noise near 0.0167 Hz (the spin frequency), and very stable instruments over the whole mission. Redundancy on long timescales comes in two versions: (i) *Planck* scans approximately the same circle on the sky every six months, alternating in the direction of the scan; and (ii) *Planck* scans exactly (within arcminutes) the same circle on the sky every one year. The ability to compare maps made in individual all-sky "surveys" (i.e., covering approximately six month intervals) and year-by-year is invaluable in identifying specific systematic effects and calibration errors. Although *Planck* was designed to cover the whole

sky twice over, its superb in-flight performance has enabled it to complete nearly five full-sky maps with the HFI instrument, and it will complete eight full-sky maps with the LFI instrument later in 2013. The redundancy provided by such a large number of surveys is a major feature of *Planck*, allowing tests of the overall stability of the instruments over the mission and sensitive measurements of systematic residuals on the sky.

Redundancy of a different sort is provided by multiple detectors within frequency bands. HFI includes four independent pairs of polarization-sensitive detectors in each channel from 100 to 353 GHz, in addition to the four total intensity (spider web) detectors at all frequencies except at 100 GHz. The LFI includes six independent pairs of polarization-sensitive detectors at 70 GHz, with three at 44 GHz and two at 30 GHz. The different technologies used by the two instruments provide an additional powerful tool to identify and remove systematic effects.

Overall, the combination of scanning strategy and instrumental redundancy has allowed identification and removal of most systematic effects affecting CMB temperature measurements. This can be seen in the fact that additional surveys have led to significant improvements, at a rate greater than the square root of the integration time, in the signal-to-noise ratio achieved in the combined maps. Given that the two instruments have achieved their expected intrinsic sensitivity, and that most systematics have been brought below the noise (detector or cosmic variance) for intensity, it is a fact that temperature-based cosmology based on the *Planck* data is already being limited by the foregrounds, fulfilling one of the main objectives of the mission (Planck Collaboration XII 2013; Planck Collaboration XVI 2013).

3.3 The Map-Making and instrumental noise distribution

3.3.1 Beam representation

The *Planck* frequency maps are of course constructed from many detectors that sample each pixel at different angles. Therefore the scanning beams do not represent well the point spread function at map level. Instead, "effective beams" are computed for each pixel and frequency using the Fast Pixel Space Convolution for CMB Surveys with Asymmetric Beams and Complex Scan Strategies, `FEBeCoP`, algorithm (Mitra et al. 2011).

`FEBeCoP` calculates the effective beam at a position in the sky by computing the real space average of the scanning beam over all observed crossing angles at that sky position. Table 3.2 summarizes the distribution across the sky of a set of parameters representing the beams, and Fig. 3.2 shows, in the 100 GHz case, their variation across the sky. We note that the effective beams include pixelization effects (essentially the Hierarchical Equal Area isoLatitude Pixelization, HEALpix, (Gorski et al. 2005) pixelization window function). The effective beam window function for LFI is calculated by `FEBeCoP` using an ensemble of signal-only simulations convolved with the effective beams. For HFI, the `quickbeam` harmonic space effective beam code (Planck Collaboration VII 2013) is used to calculate the effective beam window function given the scan history and the scanning beam.

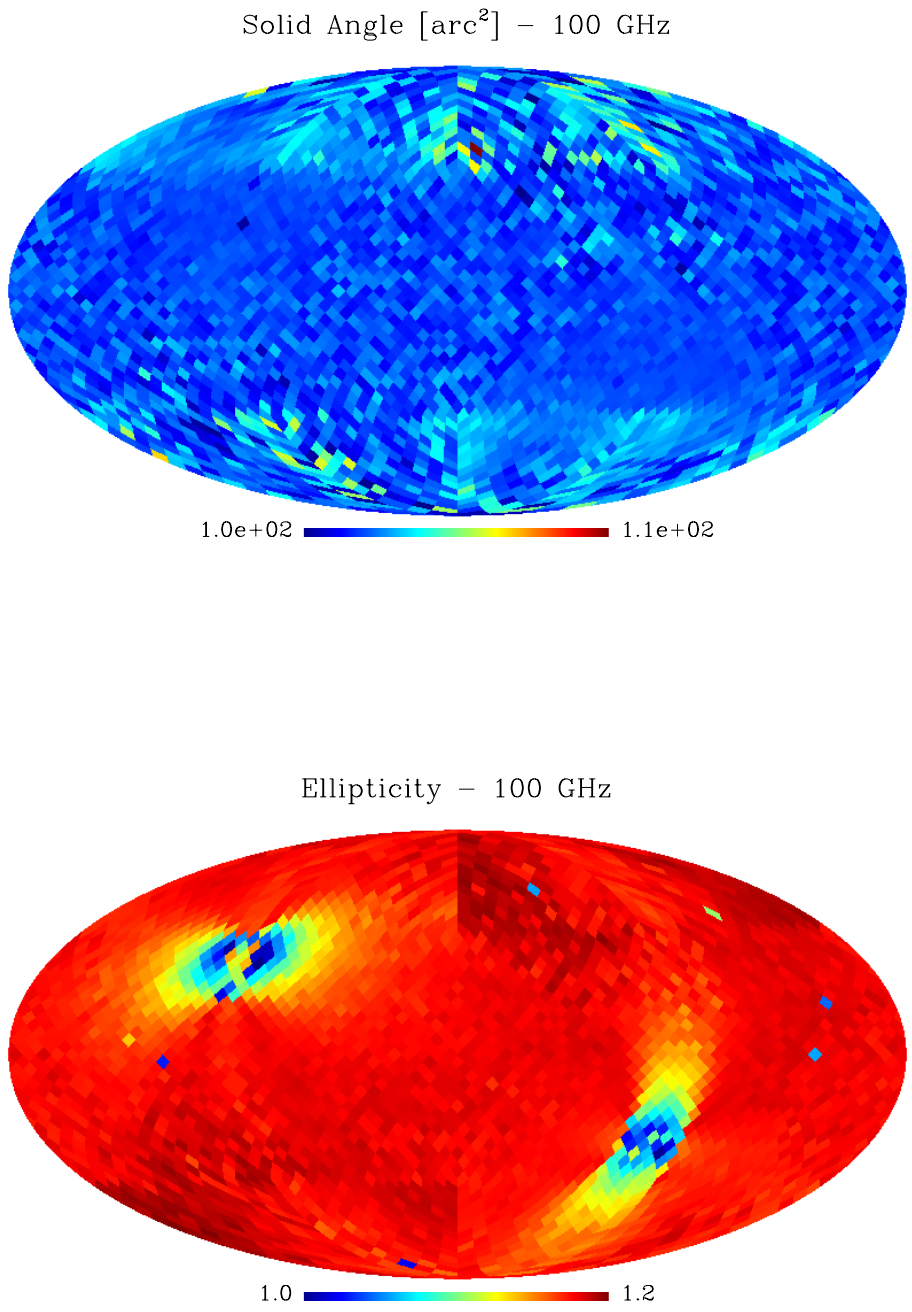

Figure 3.2: This figure shows the distribution across the sky of the solid angle (top) and ellipticity of the effective beams at 100 GHz. The distribution is typical for all channels (Planck Collaboration I 2013).

Table 3.2: Statistics of spatial distribution of effective beam parameters: FWHM, ellipticity and beam solid angle

Band	FWHM[a] [arcmin]	Ellipticity	Ω [arcmin^2]
30.....	32.239 ± 0.013	1.320 ± 0.031	1189.51 ± 0.84
44.....	27.01 ± 0.55	1.034 ± 0.033	833 ± 32
70.....	13.252 ± 0.033	1.223 ± 0.026	200.7 ± 1.0
100.....	9.651 ± 0.014	1.186 ± 0.023	105.778 ± 0.311
143.....	7.248 ± 0.015	1.036 ± 0.009	59.954 ± 0.246
217.....	4.990 ± 0.025	1.177 ± 0.030	28.447 ± 0.271
353.....	4.818 ± 0.024	1.147 ± 0.028	26.714 ± 0.250
545.....	4.682 ± 0.044	1.161 ± 0.036	26.535 ± 0.339
857.....	4.325 ± 0.055	1.393 ± 0.076	24.244 ± 0.193

[a] Mean of best-fit Gaussians to the effective beams.

3.3.2 Map-making

LFI

The calibrated Time-Ordered Information (TOI) of each LFI radiometer are used as input to the `Madam` map-making code (Keihänen et al. 2010) together with the corresponding pointing data, in the form of the Euler angles (θ, ϕ, ψ). `Madam` implements a polarized destriping approach to map-making; the noise is modelled as white noise plus a set of offsets, or baselines. The algorithm estimates in a maximum-likelihood fashion the amplitudes of the baselines, subtracts them from the actual TOI, and then simply bins the result into a map. The output consists of pixelized maps of the three Stokes parameters (T, Q, U). The LFI temperature maps being released at this time by the *Planck*' satellite are shown as the first three maps in Fig. 3.3.

In order to create maps in the maximum-likelihood approach, the noise covariance matrix of the problem has to be specified. In general, *Planck* uses a white noise covariance matrix. The pipeline allows the use of different user-defined

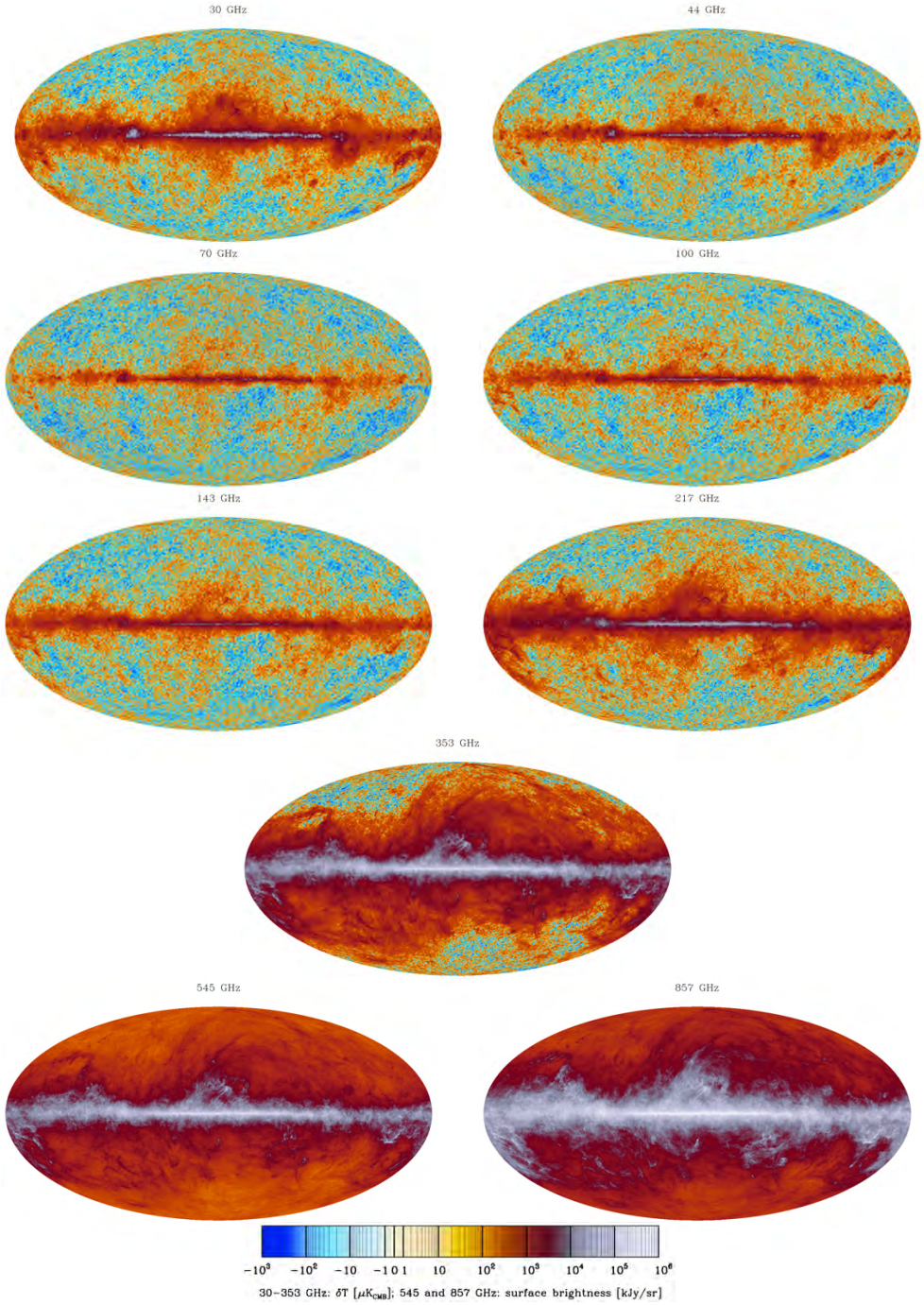

Figure 3.3: The nine *Planck* frequency maps show the broad frequency response of the individual channels. The color scale (shown below) has been tailored to show the full dynamic range of the maps (Planck Collaboration I 2013).

weighting schemes. The released maps are made using the horn-uniform weighting scheme with

$$C_w^{-1} = \frac{2}{\sigma_M^2 + \sigma_S^2}, \tag{3.1}$$

where σ_M and σ_S are the white noise sensitivities of the Main and Side radiometers of a given horn, and these radiometers are weighted equally.

Planck also create half-ring maps[2] using the same algorithm as for the released maps. A time-weighted difference between the first-half and second-half ring maps captures the noise properties directly from the data, but only for noise components whose frequency is $f \gtrsim 2/20\text{min} = 1.7\,\text{mHz}$, i.e., half the duration of the pointing period.

A zero level is determined for each LFI map in two independent ways:

- a cosecant model of latitudinal Galactic emission is fitted to the region $-90\,\text{deg} < b < -15\,\text{deg}$.
- the CMB from a clean patch of the sky is removed, and the remaining level is set to zero.

The two methods yield consistent results, and the level estimated from the first method is subtracted from the LFI maps, see Planck Collaboration I (2013).

HFI

The maps for the HFI channels are made by projecting the processed HEALPix rings built from the TOIs onto an HEALPix map (Planck Collaboration ES 2013; Planck Collaboration VI 2013). First, maps of individual rings are created by

[2] A half-ring map is built from data acquired from either the first half or the second half of the total duration of each ring (pointing period across the scanning).

averaging filtered and baseline-subtracted TOIs into HEALPix pixels. Second, these ring maps are used for the photometric calibration of each detector, see Planck Collaboration I (2013). Then, these calibrated ring maps are combined via a least-squares destriping procedure (Planck Collaboration VIII 2013) that estimates a constant offset per ring using the cross-linking of the *Planck* scan strategy. Various maps are produced, corresponding to individual detectors, subsets of detectors at each frequency, and all the detectors at a given frequency. Half-ring maps are also built, using only the first and second halves of all rings, to monitor the statistical and systematic noise properties of the maps.

Because of its rotation and orbit, contributions to the *Planck* TOI from far-sidelobe pickup (mostly of the Galaxy at high frequencies) and of the Zodiacal light do not project directly onto fixed sky coordinates, and are a significant contaminant at 353 GHz and above. Hence, they must be estimated and removed separately (Planck Collaboration XIV (2013) and Planck Collaboration ES (2013)). In the 2013 release *Planck* provide two setss of HFI maps:

- a "default" set of maps from which neither far-sidelobe straylight nor zodiacal emission has been removed. These default maps are the ones used for the extraction of the CMB map in order to search for NG. The rationale for not removing zodiacal emission is that it has been shown to produce artifacts during component separation (Planck Collaboration XII 2013). For CMB extraction, it is more effective to assume that the component separation (Sect. 3.3.4) efficiently removes zodiacal emission.

- a second set of maps from which an estimate of the far-sidelobe straylight and zodiacal emission have been removed (Planck Collaboration XIV

2013). To achieve this, the zodiacal emission is estimated by fitting to the *COBE* emission model (Kelsall et al. 1998) and subtracted from the TOI before mapmaking. Zodiacal emission is removed at all frequencies. Far-sidelobe emission is estimated and removed at 545 and 857 GHz only. This is the set of maps which should be used for work related to diffuse foregrounds.

The 2013 HFI maps contain significant Galactic CO emission. Specific component separation pipelines, subsection (3.3.4), yield separate estimates of it (see Planck Collaboration XIII (2013)) optimized for different scientific uses.

The HFI frequency maps contain an offset that arises from two different components, the diffuse interstellar medium and the CIB. The offset level due to the diffuse interstellar medium is estimated by correlating the HFI maps with a map of the column density of neutral hydrogen. This offset should be removed from the released maps before carrying out scientific analysis of Galactic emission (Planck Collaboration I 2013). The mean level contributed by the CIB at each frequency is estimated by means of an empirical model that fits the current data. For analysis of total emission, the CIB level, see (Planck Collaboration VIII 2013), must be added to the released maps after readjustment for the interstellar medium offset described above.

The resulting HFI maps are shown in Fig. 3.3.

3.3.3 Simulations

Planck simulates TOI for the Full Focal Plane (FFP) for the nominal mission. Each FFP simulation comprises: a single “fiducial” realization (CMB, astrophysi-

cal foregrounds, and noise), together with separate Monte Carlo (MC) realizations of the CMB and noise. The first *Planck* cosmology results were supported primarily by the sixth FFP simulation-set, hereafter FFP6. The first five FFP realizations were less comprehensive and were primarily used for validation and verification of the *Planck* analysis codes and for cross-validation of the data analysis and FFP simulation pipelines.

To mimic the sky data as closely as possible, FFP6 used the flight pointing, data flags and detector band-passes, beams and noise properties. For the fiducial realization, maps were made of the total observation (CMB, foregrounds and noise) at each frequency for the nominal mission. In addition, maps were made of each component separately, of subsets of detectors at each frequency, and of half-ring and single survey subsets of the data. The noise and CMB Monte Carlo realization-sets also include both full- and sub-sets of detectors at each frequency and full-and half-ring data sets for each detector combination. With about 125 maps per realization and 1000 realizations of both the noise and CMB, FFP6 totals some 250,000 maps — by far the largest simulation set ever fielded in support of a CMB mission. In the next chapters we will see how these simulations are essential in order to make our claims robust.

3.3.4 CMB map extraction

The *Planck* approach to component separation, and more specifically to extraction of a CMB map, is described in detail in Planck Collaboration XII (2013). A single component separation technique cannot extract the maps for all the known intensity diffuse components (CMB and foregrounds) as the number of parame-

ters needed to describe them even minimally exceeds the number of frequency channels. Four different methods were optimized to produce a CMB map based on the *Planck* maps alone, i.e., without the addition of any other external data: Spectral Matching Independent Component Analysis (SMICA), an implementation of independent component analysis of power spectra; Needlet Internal Linear Combination (NILC), a needlet-based version of internal linear combination; Commander-Ruler (C-R), a pixel-based version of parameter and template fitting; and Spectral Estimation Via Expectation Maximisation (SEVEM), template fitting using the lowest and highest frequency bands.

The use of several methods giving consistent results is a useful cross-validation tool, and demonstrates the robustness of the CMB map obtained by *Planck*. All four algorithms were run on the FFP6 simulations of *Planck* data (see Sect. 3.3.3). Based on this comparison and on statistical tests conducted on the real *Planck* data (consistency with *Planck* likelihood, correlation with external templates, local distribution of skewness and kurtosis, and more), one method, SMICA, was selected to extract a CMB map useful for NG and related searches on the largest possible fraction of the sky; this is the map used as the main source in a wide variety of analysis presented in the 2013 *Planck* release (Planck Collaboration XXIII 2013 the analysis on isotropy and statistics of the CMB, Planck Collaboration XXIV 2013 the analysis on primordial NG, and Planck Collaboration XIX 2013 the analysis on the integrated Sachs-Wolfe effect). However, all four methods yield CMB maps that are adequate for similar analysis, although their performance varies from method to method (Planck Collaboration XII 2013), and some may be more suitable for specific studies.

The SMICA map (see Fig. 3.4) estimates the CMB over about 97 % of the sky,

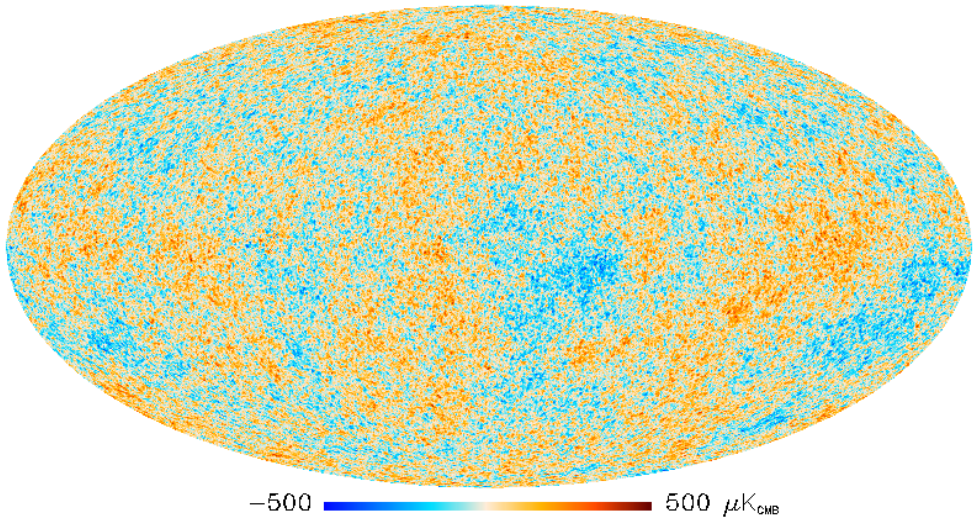

Figure 3.4: The SMICA CMB map (with 3 % of the sky replaced by a constrained Gaussian realization).

with the remaining area replaced with a constrained Gaussian realization. It has an angular resolution of 5′, but its harmonic content is cut off for $\ell > 4000$. In the pixel domain, the noise has an average RMS of about 17 μK (for the cut off at $\ell = 4000$), but its distribution is highly inhomogeneous (see Fig. 3.5).

Figure 3.6 illustrates the signal-to-noise ratio reached by *Planck* for the CMB signal. It shows, for the SMICA rendering, the angular spectrum of the estimated CMB map, of the associated half-ring noise and their difference (both raw and smoothed) after beam correction. The latter noise-corrected spectrum shows the CMB spectrum plus any remaining contamination. Note how the seventh acoustic peak is visible and how the SNR reaches unity (for single multipoles) at $\ell \sim 1700$.

All four methods yield also a set of "residual" maps that contain astrophysical foregrounds and other sources of noise. As noted previously, the problem of

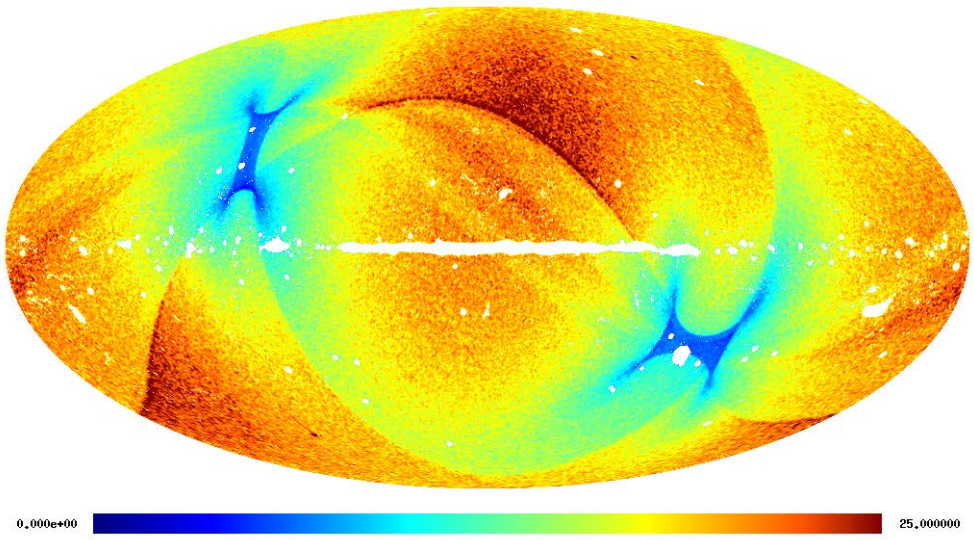

Figure 3.5: Spatial distribution of the noise RMS on a color scale of 25 μK for the SMICA CMB map. It has been estimated from the noise map obtained by running SMICA through the half-ring maps and taking the half-difference. The average noise RMS is 17 μK. SMICA does not produce CMB values in the blanked pixels. They are replaced by a constrained Gaussian realization.

component separation for intensity is such that these methods are not suitable to extract physically meaningful individual components, unless ancillary information is included in the process. Nonetheless, *Planck* released residual maps for analysis in conjunction with the extracted CMB maps.

3.4 Galactic and extra-Galactic foregrounds

3.4.1 The *Planck* point-sources catalogue

The *Planck* Catalogue of Compact Sources (PCCS, Planck Collaboration XXVIII (2013)) is a list of compact sources detected by *Planck* over the entire sky, and which therefore contains both Galactic and extragalactic objects.

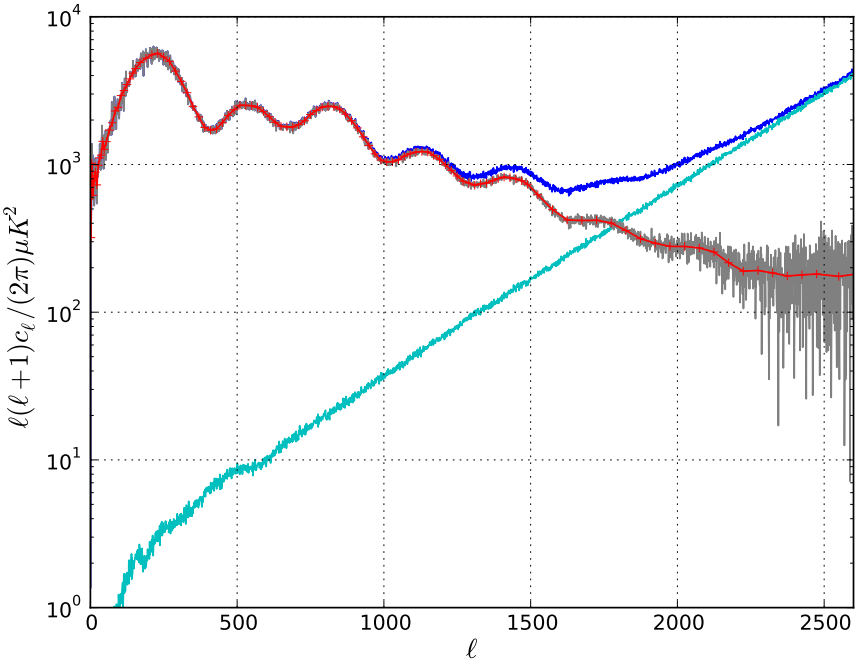

Figure 3.6: Angular spectra for the SMICA CMB products, evaluated over the confidence mask, and after removing the beam window function: spectrum of the CMB map (dark blue), spectrum of the noise in that map from the half-rings (magenta), their difference (grey) and a binned version of it (red).

The sources were extracted from the 2013 *Planck* frequency maps (Fig. 3.3), which include data acquired over more than two sky coverages.The Mexican Hat Wavelet algorithm (López-Caniego et al. 2006) has been selected as the baseline method for the production of the PCCS. However, another methods, MTXF (González-Nuevo et al. 2006) was implemented in order to support the validation and characterization of the PCCS.

The source selection for the PCCS is made on the basis of Signal-to-Noise Ratio (SNR). However, the properties of the background in the *Planck* maps vary substantially depending on frequency and part of the sky. Up to 217 GHz, the

CMB is the dominant source of confusion at high Galactic latitudes. At high frequencies, confusion from Galactic foregrounds dominates the noise budget at low Galactic latitudes, and the CIB at high Galactic latitudes. The SNR has therefore been adapted for each particular case. For details, see (Planck Collaboration I 2013)

Cluster catalogue

Planck's all-sky coverage and broad frequency range are designed to detect the SZ signal of galaxy clusters across the sky. An early catalogue of *Planck* SZ-detected clusters was released in January 2011 (ESZ, Planck Collaboration VIII 2011). In 2013, *Planck* is releasing the largest ensemble of SZ selected sources detected from an all-sky survey (Planck Collaboration XXIX 2013) deeper and six times larger than the ESZ sample.

The *Planck* SZ catalogue of clusters and candidates includes 1227 sources detected from three adapted SZ-finder algorithms down to a signal-to-noise ratio of 4.5 distributed over 83.7 % of the sky (Planck Collaboration I 2013). The statistically characterized catalogue of SZ detections was validated using external X-ray and optical/NearInfraRed (NIR) data, and a multi-frequency follow-up programme for confirmation. A total of 861 SZ detections are associated with *bona fide* clusters, of which 178 are brand new *Planck*-discovered clusters. The remaining cluster candidates are divided into three classes according to their reliability, i.e., the quality of evidence that they are likely to be *bona fide* clusters. Only 142 of them are in the lowest reliability class.

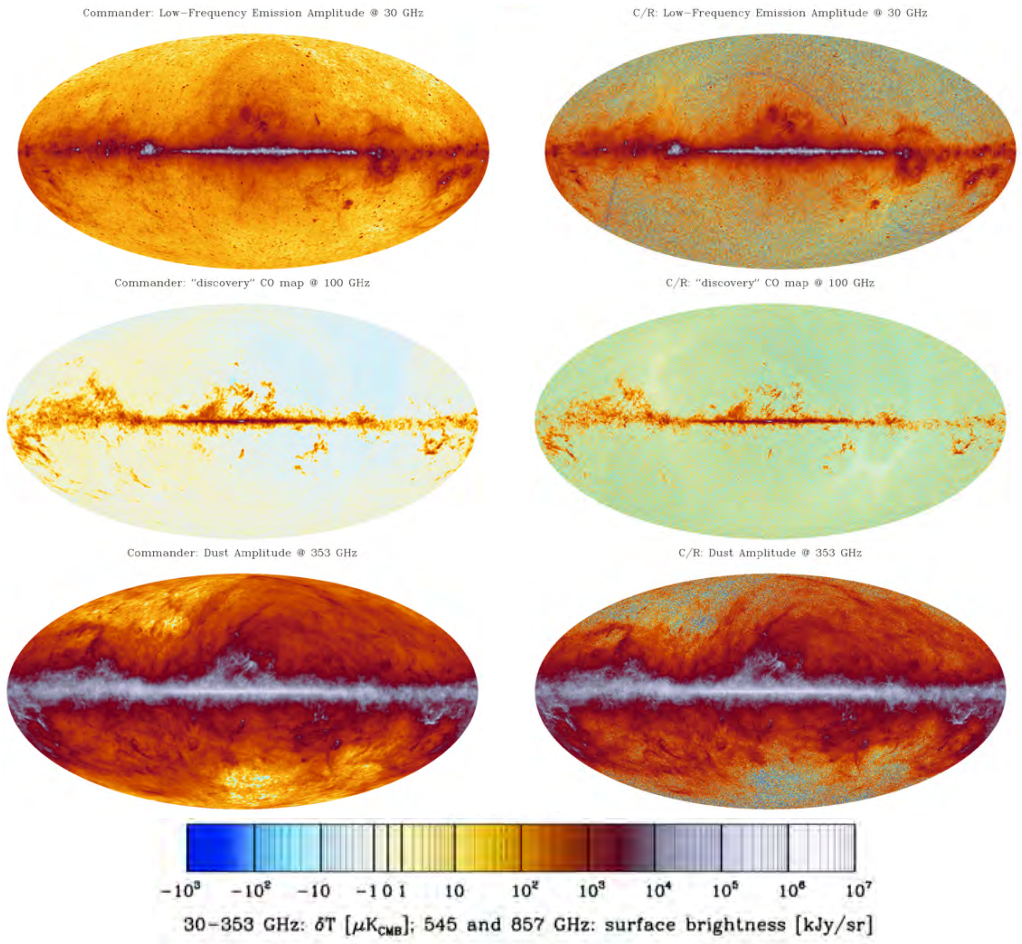

Figure 3.7: Some of the foreground maps produced by Commander (on the left, resolution ∼1 degree) and by Commander-Ruler (on the right, resolution ∼7 arcminutes). At the top, a map of the amplitude of low-frequency foregrounds at 30 GHz (which include synchrotron, free-free, and anomalous emission). In the middle, a map of the integrated intensity of CO TYPE 3. In the bottom panel, a map of the amplitude of high-frequency foregrounds at 353 GHz (dust thermal emission and the CIB).

Astrophysical foregrounds from component separation

The wide frequency range of *Planck* allows to use component separation techniques based on *Planck* data only to derive tight constraints on several astrophysical components in addition to the primary CMB fluctuations. Specifically, in the Planck Collaboration XII (2013) individual maps are represented of: 1) a combined high-frequency component accounting for Galactic thermal dust emission and the integrated thermal dust emission of the CIB; 2) Galactic carbon monoxide (CO, see Planck Collaboration I (2013)); and 3) a combined low-frequency component accounting for synchrotron, free-free, and anomalous microwave emission (AME, almost certainly emission from microscopic spinning dust grains; Fig. 3.7). Only *Planck* frequencies between 30 and 353 GHz are included, as the systematics of 545 and 857 GHz are less well understood than those of the lower ones, and the dust signal is already strongly relevant at 353 GHz.

The astrophysical components are derived by a standard Bayesian parameter estimation approach, in which an explicit parametric model is fitted to the raw observations within the bounds of physically motivated priors.

The thermal dust emission is modelled as a one-component gray-body with a free emissivity, $\beta_{\rm dust}$, and dust temperature, $T_{\rm d}$, per pixel. Since only frequencies up to 353 GHz are included here, the dust temperature is largely unconstrained, and therefore is adapted a tight prior around the commonly accepted mean value of $T_{\rm d} = 18 \pm 0.05$ K. The only reason it is not fixed completely at 18 K is to allow for modelling errors near the Galactic center. The dust emissivity prior is set to $\beta_{\rm d} = 1.5 \pm 0.3$, where the mean is once again set by a dedicated MCMC run. Because the CIB is a statistically isotropic signal, it can be

well-approximated by a dominant monopole plus a small spatially varying fluctuation, analogous to the CMB itself. Further, as shown by Planck Collaboration CIB (Planck Collaboration XVIII 2011), the CIB frequency spectrum follows very nearly a one-component gray-body function with similar parameters to those of the Galactic thermal dust component. The current model therefore accounts for the CIB component without introducing an additional and dedicated CIB parameter, simply by first subtracting off a best-fit monopole at each frequency, and, second, through the free dust parameters (amplitude and spectral indexes) for each pixel. The dust amplitude map shown in Fig. 3.7 therefore contains both Galactic thermal dust and extragalactic CIB fluctuations. The CIB fluctuations are strongly sub-dominant everywhere on the sky except than in the very cleanest regions.

The CO component is modelled in terms of a mean amplitude per pixel at 100 GHz, which is then extrapolated to 217 and 353 GHz through a spatially constant overall factor per frequency called a "line ratio."

The low-frequency component is modelled as a straight power-law in intensity units, with a free spectral index per pixel. A prior of $\beta = -3 \pm 0.3$ for the low-frequency spectral index is adopted; this is mostly relevant only at high Galactic latitudes where the signal-to-noise ratio is low and the dominant foreground component is expected to be synchrotron emission. In the signal-dominated AME and free-free regions at low latitudes, the data are sufficiently strong that the prior becomes irrelevant.

In addition, all (low-resolution) foreground amplitudes are required to be positive; computational cost prohibits *Planck* from imposing the same constraint at high resolution. Fig. 3.7 shows the resulting component maps.

In the 2013 data release, *Planck* adopted the posterior mean as signal estimate,

and the posterior RMS as the corresponding uncertainty. Mean and RMS maps are provided for each signal component and for each per-pixel spectral parameter. Two caveats are in order regarding use of these products for further scientific analysis. First, significant systematic uncertainties are associated with several of these estimates. One example is the correlated HFI noise, which is clearly seen in the thermal dust emissivity map. Second, the full posterior is significantly non-Gaussian due to the presence of non-Gaussian spectral parameters and the positivity amplitude prior, as well as strongly correlated between components. The mean and RMS maps provided in this data release should therefore be considered as a convenient representation of the full posterior, rather than a precise description of each component. For the NG analysis in the *Planck*'s paper and in this thesis the original ensemble of individual Monte Carlo samples are used to obtain the best possible precision in the analysis, as we will discuss in the next chapters.

Table 3.3: *Planck* performance parameters determined from flight data.

			Scanning Beam[c]		Noise[d] Sensitivity	
Channel	$N_{\rm detectors}$[a]	$\nu_{\rm center}$[b] [GHz]	FWHM [arcm]	Ellipticity	[μK_{RJ} $s^{1/2}$]	[μK_{CMB} $s^{1/2}$]
30 GHz	4	28.4	33.16	1.37	145.4	148.5
44 GHz	6	44.1	28.09	1.25	164.8	173.2
70 GHz	12	70.4	13.08	1.27	133.9	151.9
100 GHz	8	100	9.59	1.21	31.52	41.3
143 GHz	11	143	7.18	1.04	10.38	17.4
217 GHz	12	217	4.87	1.22	7.45	23.8
353 GHz	12	353	4.7	1.2	5.52	78.8
545 GHz	3	545	4.73	1.18	2.66	0.0259[d]
857 GHz	4	857	4.51	1.38	1.33	0.0259[d]

[a] For 30, 44, and 70 GHz, each detector is a linearly polarized radiometer, and there are two orthogonally polarized radiometers behind each horn. Each radiometer has two diodes, both switched at high frequency between the sky and a blackbody load at $\sim$ 4 K (Mennella et al. 2011). For 100 GHz and above, each detector is a bolometer (Planck HFI Core Team 2011). Most of the bolometers are sensitive to polarization, in which case there are two orthogonally polarized detectors behind each horn. Some of the detectors are spider-web bolometers (one per horn) sensitive to the total incident power. Two of the bolometers, one each at 143 and 545 GHz, are not used as they are heavily affected by random telegraphic noise (Planck HFI Core Team 2011). A third bolometer, at 857 GHz, is also affected, but some of its data are usable.

[b] Effective (LFI) or Nominal (HFI) center frequency of the N detectors at each frequency.

[c] Mean scanning beam properties of the N detectors at each frequency. FWHM $\equiv$ FWHM of circular Gaussian with the same volume. Ellipticity gives the major axis to minor axis ratio for a best-fit elliptical Gaussian. In the case of HFI, the mean values quoted are the result of averaging the values of total-power and polarization-sensitive bolometers, weighted by the number of channels and after removal of those affected by random telegraphic noise. The actual point spread function of an unresolved object on the sky depends not only on the optical properties of the beam, but also on sampling and time domain filtering in signal processing, and the way the sky is scanned.

[d] The noise level reached in 1 s integration for the array of N detectors, given the noise and integration time in the released maps, for the array of N detectors, in Rayleigh-Jeans units and in thermodynamic CMB units for 30–353 GHz; in Rayleigh-Jeans units and in MJy sr^{-1} $s^{1/2}$ for 545 and 857 GHz. We note that for LFI the white noise level is within 1-2% of these values.

Chapter 4

Estimation of non-Gaussianity

In this chapter, we review the statistical techniques that we use to estimate the non-linearity parameter $f_{\rm NL}$. We begin by fixing some notation and describing the CMB angular bispectrum in Sect. 4.1. We then introduce in Sect. 4.2 the optimal $f_{\rm NL}$ bispectrum estimator. From Sect. 4.2.1 onwards we describe in detail the different implementations of the optimal estimator that were developed and applied to *Planck* data. In particular, the estimators developed by the author of this thesis, KSW and Skew-C_ℓ, will be described in this chapter (definitions are in the following subsections). The companion estimators used in most of the analysis and validation of the *Planck* data in Planck Collaboration XXIV (2013), that are Modal, Binned and Wavelets estimators, are described in Appendix (B). Since those estimators were of critical importance to strengthen the $f_{\rm NL}$ limits obtained, they are also reported here to support the robustness of the results obtained with KSW and Skew-C_ℓ estimators.

4.1 The CMB angular bispectrum

Temperature anisotropies are represented using the $a_{\ell m}$ coefficients of a spherical harmonic decomposition of the CMB map,

$$\frac{\Delta T}{T}(\hat{\mathbf{n}}) = \sum_{\ell m} a_{\ell m} Y_{\ell m}(\hat{\mathbf{n}})\,; \tag{4.1}$$

we write $C_\ell = \langle |a_{\ell m}|^2 \rangle$ for the angular power spectrum and $\hat{C}_\ell = (2\ell+1)^{-1} \sum_m |a_{\ell m}|^2$ for the corresponding (ideal) estimator; hats "ˆ" denote estimated quantities. The CMB angular bispectrum is the three-point correlator of the $a_{\ell m}$:

$$B^{m_1 m_2 m_3}_{\ell_1 \ell_2 \ell_3} \equiv \langle a_{\ell_1 m_1} a_{\ell_2 m_2} a_{\ell_3 m_3} \rangle. \tag{4.2}$$

If the CMB sky is rotationally invariant, the angular bispectrum can be factorized as follows:

$$\langle a_{\ell_1 m_1} a_{\ell_2 m_2} a_{\ell_3 m_3} \rangle = \mathcal{G}^{\ell_1 \ell_2 \ell_3}_{m_1 m_2 m_3}\, b_{\ell_1 \ell_2 \ell_3}\,, \tag{4.3}$$

where $b_{\ell_1 \ell_2 \ell_3}$ is the so called *reduced bispectrum*, and $\mathcal{G}^{\ell_1 \ell_2 \ell_3}_{m_1 m_2 m_3}$ is the Gaunt integral, defined as:

$$\begin{aligned} \mathcal{G}^{\ell_1 \ell_2 \ell_3}_{m_1 m_2 m_3} &\equiv \int Y_{\ell_1 m_1}(\hat{\mathbf{n}})\, Y_{\ell_2 m_2}(\hat{\mathbf{n}})\, Y_{\ell_3 m_3}(\hat{\mathbf{n}})\, d^2\hat{\mathbf{n}} \\ &= h_{\ell_1 \ell_2 \ell_3} \begin{pmatrix} \ell_1 & \ell_2 & \ell_3 \\ m_1 & m_2 & m_3 \end{pmatrix}, \end{aligned} \tag{4.4}$$

where $h_{\ell_1\ell_2\ell_3}$ is a geometrical factor,

$$h_{\ell_1\ell_2\ell_3} = \sqrt{\frac{(2\ell_1+1)(2\ell_2+1)(2\ell_3+1)}{4\pi}} \begin{pmatrix} \ell_1 & \ell_2 & \ell_3 \\ 0 & 0 & 0 \end{pmatrix} . \tag{4.5}$$

The Wigner-3j symbol in parentheses enforces rotational symmetry, and allows us to restrict attention to a tetrahedral domain of multipole triplets $\{\ell_1, \ell_2, \ell_3\}$, satisfying both a triangle condition and a limit given by some maximum resolution $\ell_{\rm max}$ (the latter being defined by the finite angular resolution of the experiment under study). This three-dimensional domain $\mathcal{V}_\mathcal{T}$ of allowed multipoles, sometimes referred to in the following as a "tetrapyd", is illustrated in Fig. 4.1 and it is explicitly defined by

$$\begin{aligned} &\text{Triangle condition:} && \ell_1 \leq \ell_2 + \ell_3 \ \text{ for } \ \ell_1 \geq \ell_2,\ \ell_3, \text{+perms.}, \\ &\text{Parity condition:} && \ell_1 + \ell_2 + \ell_3 = 2n\,, \quad n \in \mathbb{N}\,, \\ &\text{Resolution:} && \ell_1, \ell_2, \ell_3 \leq \ell_{\rm max}\,, \quad \ell_1, \ell_2, \ell_3 \in \mathbb{N}\,. \end{aligned} \tag{4.6}$$

Here, $\mathcal{V}_\mathcal{T}$ is the isotropic subset of the full space of bispectra, denoted by $\mathcal{V}$.

One can also define an alternative rotationally-invariant reduced bispectrum $B_{\ell_1\ell_2\ell_3}$ in the following way:

$$B_{\ell_1\ell_2\ell_3} \equiv h_{\ell_1\ell_2\ell_3} \sum_{m_1m_2m_3} \begin{pmatrix} \ell_1 & \ell_2 & \ell_3 \\ m_1 & m_2 & m_3 \end{pmatrix} B^{m_1m_2m_3}_{\ell_1\ell_2\ell_3} . \tag{4.7}$$

Note that this $B_{\ell_1\ell_2\ell_3}$ is equal to $h_{\ell_1\ell_2\ell_3}$ times the angle-averaged bispectrum as defined in the literature. From Eqs. (4.3) and (4.4), and the fact that the sum over

all m_i of the Wigner-3j symbol squared is equal to 1, it is easy to see that $B_{\ell_1\ell_2\ell_3}$ is related to the reduced bispectrum by

$$B_{\ell_1\ell_2\ell_3} = h^2_{\ell_1\ell_2\ell_3} b_{\ell_1\ell_2\ell_3} \ . \tag{4.8}$$

The interest in this bispectrum $B_{\ell_1\ell_2\ell_3}$ is that it can be estimated directly from maximally-filtered maps of the data:

$$\hat{B}_{\ell_1\ell_2\ell_3} = \int d^2\hat{\mathbf{n}} T_{\ell_1}(\hat{\mathbf{n}}) T_{\ell_2}(\hat{\mathbf{n}}) T_{\ell_3}(\hat{\mathbf{n}}) \ , \tag{4.9}$$

where the filtered maps $T_\ell(\hat{\mathbf{n}})$ are defined as:

$$T_\ell(\hat{\mathbf{n}}) \equiv \sum_m a_{\ell m} Y_{\ell m}(\hat{\mathbf{n}}) \ . \tag{4.10}$$

This can be seen by replacing the $B^{m_1 m_2 m_3}_{\ell_1\ell_2\ell_3}$ in Eq. (4.7) by its estimate $a_{\ell_1 m_1} a_{\ell_2 m_2} a_{\ell_3 m_3}$ and then using Eq. (4.4) to rewrite the Wigner symbol in terms of a Gaunt integral, which in turn is expressed as an integral over the product of three spherical harmonics.

4.2 CMB bispectrum estimators

The full bispectrum for a high-resolution map cannot be evaluated explicitly because of the sheer number of operations involved, $O(\ell^5_{\rm max})$, as well as the fact that the signal will be too weak to measure in individual multipoles with any significance. Instead, we essentially use a least-squares fit to compare the bispectrum of the observed CMB multipoles with a particular theoretical bispectrum

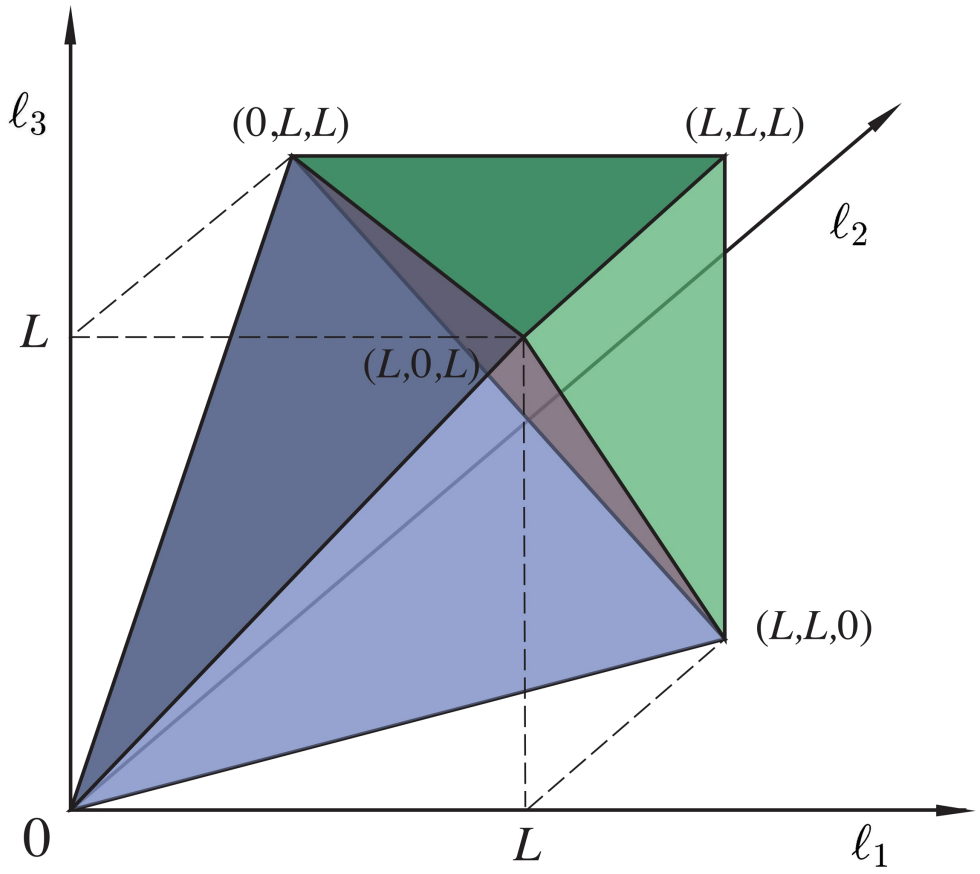

Figure 4.1: Permitted observational domain of Eq. (4.6) for the CMB bispectrum $b_{\ell_1\ell_2\ell_3}$. Allowed multipole values (ℓ_1, ℓ_2, ℓ_3) lie inside the shaded "tetrapyd" region (tetrahedron+pyramid), satisfying both the triangle condition and the experimental resolution $\ell < L \equiv \ell_{\rm max}$.

$b_{\ell_1\ell_2\ell_3}$. We then extract an overall "amplitude parameter" $f_{\rm NL}$ for that specific template, after defining a suitable normalization convention so that we can write $b_{\ell_1\ell_2\ell_3} = f_{\rm NL} b^{\rm th}_{\ell_1\ell_2\ell_3}$, where $b^{\rm th}_{\ell_1\ell_2\ell_3}$ is defined as the value of the theoretical bispectrum ansatz for $f_{\rm NL} = 1$.

Optimal 3-point estimators, introduced by Heavens (1998) (Gangui and Martin 2000), are those which saturate the Cramér-Rao bound . Taking into account the fact that instrument noise and masking can break rotational invariance, it has been

shown that the general optimal $f_{\rm NL}$ estimator can be written as (Babich 2005; Creminelli et al. 2006; Senatore et al. 2010; Verde et al. 2013):

$$\begin{aligned}\hat{f}_{\rm NL} =& \frac{1}{N}\sum_{\ell_i,m_i} \mathcal{G}^{\ell_1\,\ell_2\,\ell_3}_{m_1 m_2 m_3} b^{\rm th}_{\ell_1\ell_2\ell_3} \\ & \times \left[C^{-1}_{\ell_1 m_1,\ell_1' m_1'} a_{\ell_1' m_1'}\, C^{-1}_{\ell_2 m_2,\ell_2' m_2'} a_{\ell_2' m_2'}\, C^{-1}_{\ell_3 m_3,\ell_3' m_3'} a_{\ell_3' m_3'}\right. \\ & \left. - 3\, C^{-1}_{\ell_1 m_1,\ell_2 m_2} C^{-1}_{\ell_3 m_3,\ell_3' m_3'} a_{\ell_3' m_3'}\right],\end{aligned} \tag{4.11}$$

where C^{-1} is the inverse of the covariance matrix $C_{\ell_1 m_1,\ell_2 m_2} \equiv \langle a_{\ell_1 m_1} a_{\ell_2 m_2}\rangle$ and N is a suitable normalization chosen to produce unit response to $b^{\rm th}_{\ell_1\ell_2\ell_3}$.

In the expression of the optimal estimator above we note the presence of two contributions, one (hereafter defined the "cubic term" of the estimator) is cubic in the observed $a_{\ell m}$ and correlates the bispectrum of the data to the theoretical fitting template $b^{\rm th}_{\ell_1\ell_2\ell_3}$, while the other is linear in the observed $a_{\ell m}$ (hereafter, the "linear term"), which is zero on average. In the rotationally-invariant case the linear term is proportional to the monopole in the map, which has been set to zero, so in this case the estimator simply reduces to the cubic term. However, when rotational invariance is broken by realistic experimental features such as a Galactic mask or an anisotropic noise distribution, the linear term has an important effect on the estimator variance. In this case, the coupling between different ℓ would in fact produce a spurious increase in the error bars (coupling of Fourier modes due to statistical anisotropy can be "misinterpreted" by the estimator as NG). The linear term correlates the observed $a_{\ell m}$ to the power spectrum anisotropies and removes this effect, thus restoring optimality (Creminelli et al. 2006; Yadav et al. 2007, 2008b).

The actual problem with Eq. (4.11) is that its direct implementation to get an optimal $f_{\rm NL}$ estimator would require measurement of all the bispectrum configurations from the data. As already mentioned at the beginning of this section, the computational cost of this would scale like $\ell_{\rm max}^5$ and be totally prohibitive for high-resolution CMB experiments. Even taking into account the constraints imposed by isotropy, the number of multipole triples $\{\ell_1, \ell_2, \ell_3\}$ is of the order of 10^9 at *Planck* resolution, and the number of different observed bispectrum configurations $\hat{b}^{\ell_1\ell_2\ell_3}_{m_1m_2m_3}$ is of the order of 10^{15}. For each of them, costly numerical evaluation of the Wigner symbol is also required. This is completely out of reach of existing supercomputers. It is then necessary to find numerical solutions that circumvent this problem and in the following subsections we will show how the different estimators used for the $f_{\rm NL}$ *Planck* data analysis address this challenge. Before entering into a more accurate description of these different methods, we would like however to stress again that they are all going to be different implementations of the optimal $f_{\rm NL}$ estimator defined by Eq. (4.11); therefore they are conceptually equivalent and expected to produce $f_{\rm NL}$ results that are in very tight agreement. This will later on allow for stringent validation tests based on comparing different pipelines. On the other hand, it will soon become clear that the different approaches that we are going to discuss also open up a range of additional applications beyond simple $f_{\rm NL}$ estimation for standard bispectra. Such applications include, for example, full bispectrum reconstruction (in a suitably smoothed domain), tests of directional dependence of $f_{\rm NL}$, and other ways to reduce the amount of data, going beyond simple single-number $f_{\rm NL}$ estimation (Planck Collaboration XXIV 2013). So different methods will also provide a vast range of complementary information.

Another important preliminary point, to notice before discussing different techniques, is that none of the estimators in the following sections implement exactly Eq. (4.11), but a slightly modified version of it. In Eq. (4.11) the CMB multipoles always appear weighted by the inverse of the full covariance matrix. Inverse covariance filtering of CMB data at the high angular resolutions achieved by experiments like *WMAP* and *Planck* is another very challenging numerical issue, which was fully addressed only recently (Elsner and Wandelt 2013; Komatsu et al. 2011; Smith et al. 2009). For *Planck* analyses in (Planck Collaboration XXIV 2013), were developed two independent inverse-covariance filtering pipelines. The former is based on an extension to *Planck* resolution of the algorithm used for *WMAP* analysis (Komatsu et al. 2011; Smith et al. 2009); the latter is based on the algorithm described in Elsner and Wandelt (2013). However, detailed comparisons interestingly showed that our estimators perform *equally* well (i.e., they saturate the Cramér-Rao bound) if we approximate the covariance matrix as diagonal in the filtering procedure *and* we apply a simple diffusive inpainting procedure to the masked areas of the input CMB maps. A more detailed description of inpainting and Wiener filtering algorithms can be found in Sect. 4.3.

In the diagonal covariance approximation, the minimum variance estimator is obtained by making the replacement $(C^{-1}a)_{\ell m} \rightarrow a_{\ell m}/C_\ell$ in the cubic term and then including the linear term that minimizes the variance for this class of cubic estimator (Creminelli et al. 2006). This procedure leads to the following

expression:

$$\hat{f}_{\rm NL} = \frac{1}{N} \sum_{\ell_i, m_i} \mathcal{G}^{\ell_1\,\ell_2\,\ell_3}_{m_1 m_2 m_3} \tilde{b}^{\rm th}_{\ell_1\ell_2\ell_3} \times \left[\frac{\tilde{a}_{\ell_1 m_1}}{\tilde{C}_{\ell_1}} \frac{\tilde{a}_{\ell_2 m_2}}{\tilde{C}_{\ell_2}} \frac{\tilde{a}_{\ell_3 m_3}}{\tilde{C}_{\ell_3}} - 6 \frac{\tilde{C}_{\ell_1 m_1, \ell_2 m_2}}{\tilde{C}_{\ell_1} \tilde{C}_{\ell_2}} \frac{\tilde{a}_{\ell_3 m_3}}{\tilde{C}_{\ell_3 m_3}} \right], \tag{4.12}$$

where the tilde denotes the modification of C_ℓ and $b_{\ell_1\ell_2\ell_3}$ to incorporate instrument beam and noise effects, and indicates that the multipoles are obtained from a map that was masked and preprocessed through the inpainting procedure detailed in Sect. 4.3. This means that

$$\tilde{b}_{\ell_1\ell_2\ell_3} \equiv b_{\ell_1} b_{\ell_2} b_{\ell_3} b_{\ell_1\ell_2\ell_3} \,, \qquad \tilde{C}_\ell \equiv b_\ell^2 C_\ell + N_\ell \,, \tag{4.13}$$

where b_ℓ denotes the experimental beam, and N_ℓ is the noise power spectrum. For simplicity of notation, in the following we will drop the tilde and always assume that beam, noise and inpainting effects are properly included.

Using Eqs. (4.7) and (4.8) we can rewrite Eq. (4.12) in terms of the bispectrum $B_{\ell_1\ell_2\ell_3}$:

$$\hat{f}_{\rm NL} = \frac{6}{N} \sum_{\ell_1 \le \ell_2 \le \ell_3} \frac{B^{\rm th}_{\ell_1\ell_2\ell_3} \left(B^{\rm obs}_{\ell_1\ell_2\ell_3} - B^{\rm lin}_{\ell_1\ell_2\ell_3} \right)}{V_{\ell_1\ell_2\ell_3}}. \tag{4.14}$$

In the above expression, $B^{\rm th}$ is the theoretical template for B (with $f_{\rm NL} = 1$) and $B^{\rm obs}$ denotes the observed bispectrum (the cubic term), extracted from the (inpainted) data using Eq. (4.9). $B^{\rm lin}$ is the linear correction, also computed using Eq. (4.9) by replacing two of the filtered temperature maps by simulated Gaussian ones and averaging over a large number of them (three permutations). The variance V in the inverse-variance weights is given by $V_{\ell_1\ell_2\ell_3} = g_{\ell_1\ell_2\ell_3} h^2_{\ell_1\ell_2\ell_3} C_{\ell_1} C_{\ell_2} C_{\ell_3}$

(remember that these should be viewed as being the quantities with tildes, having beam and noise effects included) with $g_{\ell_1\ell_2\ell_3}$ a permutation factor ($g_{\ell_1\ell_2\ell_3} = 6$ when all ℓ are equal, $g_{\ell_1\ell_2\ell_3} = 2$ when two ℓ are equal, and $g_{\ell_1\ell_2\ell_3} = 1$ otherwise). Both Eqs. (4.12) and (4.14) will be used in the following. Eq. (4.12) will provide the starting point for the KSW, skew-C_ℓ.

Next, we will describe in detail the different methods, and show how they address the numerical challenge posed by the necessity to evaluate a huge number of bispectrum configurations. Summarizing: the KSW estimator and the Skew-C_ℓ approach achieve massive reductions in computational costs by exploiting separability properties of $b^{\rm th}$.

4.2.1 The KSW estimator

To understand the rationale behind the KSW estimator (Komatsu et al. 2003, 2005, Creminelli et al. 2006, Yadav and Wandelt 2008; Yadav et al. 2007, 2008b, Smith and Zaldarriaga 2011a, Senatore et al. 2010), we need to assume that the theoretical reduced bispectrum $b^{\rm th}_{\ell_1\ell_2\ell_3}$ can be exactly decomposed into a separable structure, e.g., there exist some sequences of functions $\alpha(\ell, r)$, $\beta(\ell, r)$ such that we can approximate $b_{\ell_1\ell_2\ell_3}$ as

$$\begin{aligned} b_{\ell_1\ell_2\ell_3} \simeq \int & [\beta(\ell_1, r)\beta(\ell_2, r)\alpha(\ell_3, r) + \beta(\ell_1, r)\beta(\ell_3, r)\alpha(\ell_2, r) \\ & + \beta(\ell_2, r)\beta(\ell_3, r)\alpha(\ell_1, r)]\, r^2\, dr\,, \end{aligned} \tag{4.15}$$

where r is a radial coordinate. This assumption is fulfilled in particular by the local shape (Babich et al. 2004; Komatsu and Spergel 2001), with $\alpha(\ell, r)$ and $\beta(\ell, r)$ involving integrals of products of spherical Bessel functions and CMB radiation

transfer functions. Let us consider the optimal estimator of Eq. (4.12) and neglect for the moment the linear part. Exploiting Eq. (4.15) and the factorizability property of the Gaunt integral (Eq. (4.4)), the cubic term of the estimator can be written as:

$$S_{\rm cub} = \int dr\, r^2 \int d^2\hat{\mathbf{n}}\, A(\hat{\mathbf{n}}, r) B^2(\hat{\mathbf{n}}, r) \,, \tag{4.16}$$

where

$$A(\hat{\mathbf{n}}, r) = \sum_{\ell m} \frac{\alpha(\ell, r)\, a_{\ell m} Y_{\ell m}(\hat{\mathbf{n}})}{C_\ell} \,, \tag{4.17}$$

and

$$B(\hat{\mathbf{n}}, r) = \sum_{\ell m} \frac{\beta(\ell, r)\, a_{\ell m} Y_{\ell m}(\hat{\mathbf{n}})}{C_\ell} \,. \tag{4.18}$$

From the formulae above we see that the overall triple integral over all the configurations ℓ_1, ℓ_2, ℓ_3 has been factorized into a product of three separate sums over different ℓ. This produces a massive reduction in computational time, as the problem now scales like $\ell^3_{\rm max}$ instead of the original $\ell^5_{\rm max}$. Moreover, the bispectrum can be evaluated in terms of a cubic statistic in pixel space from Eq. (4.16), and the functions $A(\hat{\mathbf{n}}, r)$, $B(\hat{\mathbf{n}}, r)$ are obtained from the observed $a_{\ell m}$ by means of Fast Harmonic Transforms.

It is easy to see that the linear term can be factorized in analogous fashion. Again considering the local shape type of decomposition of Eq. (4.15), it is possible to find:

$$\begin{aligned} S_{\rm lin} = & \frac{-6}{N} \int dr\, r^2 \int d^2\hat{\mathbf{n}} \left[2 \left\langle A(r, \hat{\mathbf{n}}) B(r, \hat{\mathbf{n}}) \right\rangle_{\rm MC} \times \right. \\ & \left. \times B(r, \hat{\mathbf{n}}) + \left\langle B(r, \hat{\mathbf{n}}) B(r, \hat{\mathbf{n}}) \right\rangle_{\rm MC} A(r, \hat{\mathbf{n}}) \right] \,, \end{aligned} \tag{4.19}$$

where $\langle\cdot\rangle_{\rm MC}$ denotes a MC average over simulations accurately reproducing the properties of the actual data set (basically we are taking a MC approach to estimate the product between the theoretical bispectrum and the $a_{\ell m}$ covariance matrix appearing in the linear term expression).

The estimator can be finally expressed as a function of $S_{\rm cub}$ and $S_{\rm lin}$:

$$\hat{f}_{\rm NL} = \frac{S_{\rm cub} + S_{\rm lin}}{N}. \tag{4.20}$$

Whenever it can be applied, the KSW approach makes the problem of $f_{\rm NL}$ estimation computationally feasible, even at the high angular resolution of the *Planck* satellite. One important caveat is that the factorizability of the shape, which is the starting point of the method, is not a general property of theoretical bispectrum templates. Strictly speaking, only the local shape is manifestly separable. However, a large class of inflationary models can be extremely well approximated by separable equilateral and orthogonal templates (Babich et al. 2004; Creminelli et al. 2006; Senatore et al. 2010). The specific expressions of cubic and linear terms are of course template-dependent, but as long as the template itself is separable their structure is analogous to the example shown in this Section, i.e., they can be written as pixel space integrals of cubic products of suitably-filtered CMB maps (involving MC approximations of the $a_{\ell m}$ covariance for the linear term). For a complete and compact summary of KSW implementations for local, equilateral and orthogonal bispectra see Komatsu et al. (2009, Appendix). For convenience we report all the known separable shapes implementation for the KSW in Appendix (A) used in this thesis.

4.2.2 The Skew-C_ℓ Extension

The Skew-C_ℓ statistics were introduced by Munshi and Heavens (2010) to address an issue with estimators such as KSW which reduce the map to an estimator of $f_{\rm NL}$ for a given type of NG. This level of data compression, to a single number, has the disadvantage that it does not allow verification that a NG signal is of the type which has been estimated. KSW on its own cannot tell if a measurement of $f_{\rm NL}$ of given type is actually caused by NG of that type, or by contamination from some other source or sources. The skew-C_ℓ statistics perform a less radical data compression than KSW (to a function of ℓ), and thus retain enough information to distinguish different NG signals. The desire to find a statistics which is able to fulfil this rôle, but which is still optimal, drives one to a case which is closely related to KSW, and indeed reduces to it when the scale-dependent information is not used. A further advantage of the skew-C_ℓ is that it allows joint estimation of the level of many types of NG simultaneously. This requires a very large number of simulations for accurate estimation of their covariance matrix, and they are not used in this role in this thesis. However, they do play an important part in identifying which sources of NG are clearly detected in the data, and which are not.

We define the skew-C_ℓ statistics by extending from KSW, as follows: from Eq. (4.16), the numerator $\mathcal{E}$ can be rewritten as

$$\mathcal{E} = \sum_\ell (2\ell+1)[C_\ell^{A,B^2} + 2C_\ell^{AB,B}] \tag{4.21}$$

where

$$C_\ell^{A,B^2} = \int\int_{S^2} \sum_{\ell_1,\ell_2} \sum_{m_1,m_2,m} \left[\frac{\beta(\ell_1;r) a_{\ell_1 m_1} Y_{\ell_1 m_1}(\hat{\mathbf{n}})}{C_{\ell_1}} \times \frac{\beta(\ell_2;r) a_{\ell_2 m_2} Y_{\ell_2 m_2}(\hat{\mathbf{n}})}{C_{\ell_2}} \frac{\alpha(\ell;r) a_{\ell m} Y_{\ell m}(\hat{\mathbf{n}})}{C_\ell} \right] r^2 d^2\hat{\mathbf{n}} dr \tag{4.22}$$

and

$$C_\ell^{AB,B} = \int\int_{S^2} \sum_{\ell_1,\ell_2} \sum_{m_1,m_2,m} \left[\frac{\beta(\ell_1;r) a_{\ell_1 m_1} Y_{\ell_1 m_1}(\hat{\mathbf{n}})}{C_{\ell_1}} \times \frac{\alpha(\ell_2;r) a_{\ell_2 m_2} Y_{\ell_2, m_2}(\hat{\mathbf{n}})}{C_{\ell_2}} \frac{\beta(\ell;r) a_{\ell m} Y_{\ell m}(\hat{\mathbf{n}})}{C_\ell} \right] r^2 d^2\hat{\mathbf{n}} dr \,. \tag{4.23}$$

The skew-C_ℓ approach allows for the full implementation of the KSW procedure, when the sum in Eq. (4.21) is fully evaluated; furthermore, it allows for extra degrees of flexibility, e.g., by restricting the sum to subsets of the multipole space, which may highlight specific features of the NG signal. Each form of NG considered has its own α, β, hence its own set of skew-C_ℓ, denoted by $S_\ell \equiv C_\ell^{A,B^2} + 2C_\ell^{AB,B}$. We have chosen to illustrate here just the local form, but the method can be extended to other separable shapes; some skew-C_ℓ cases do not involve integrals, such as the ISW-lensing skew statistics. A summary of those (some are new results for this thesis and were previously not present in literature, such as orthogonal and ISW-lensing skew-C_ℓ shapes) can be founded in Appendix A. Note that in this thesis we do not fit the S_ℓ directly, but instead we estimate the NG using KSW, and then verify (or not) the nature of the NG by comparing the skew-C_ℓ with the theoretical expectation. No further free parameters are introduced at this stage. This procedure allows investigation of KSW detections of NG of a given

type, assessing whether or not they are actually due to NG of that type.

4.3 Wiener filtering

As discussed in Sect. 4.2, the $f_{\rm NL}$ bispectrum estimator requires, in principle, inverse covariance filtering of the data to achieve optimality (equivalent to Wiener filtering up to a trivial multiplication by the inverse of the signal power spectrum).

The iterative method of Elsner and Wandelt (2013) has been used for Wiener filtering simulations and data (see Planck Collaboration XXIV 2013). Results of this method have been cross-validated using an independent conjugate gradient inversion algorithm with multi-grid preconditioning, originally developed for the analysis of *WMAP* data in Smith et al. (2009). Applying this estimator to simulations pre-processed using the above mentioned algorithms yielded optimal error bars (Planck Collaboration XXIV 2013).

However, we found (see Chapter (ch:validation) and (ch:results)) that optimal error bars could also be achieved for all shapes using a much simpler diffusive inpainting pre-filtering procedure that can be described as follows: all masked areas of the sky (both Galactic and point sources) are filled in with an iterative scheme. Each pixel in the mask is filled with the average of all surrounding pixels, and this is repeated 2000 times over all masked pixels (we checked on simulations that convergence of all $f_{\rm NL}$ estimates was achieved with 2000 iterations). Note that the effect of this "inpainting" procedure, especially visible for the Galactic mask, is effectively apodizing the mask, reproducing small-scale structure near the edges and only large-scale modes in the interior (see Figure 4.2). This helps to prevent propagating any sharp-edge effects or lack of large-scale power in the interior of

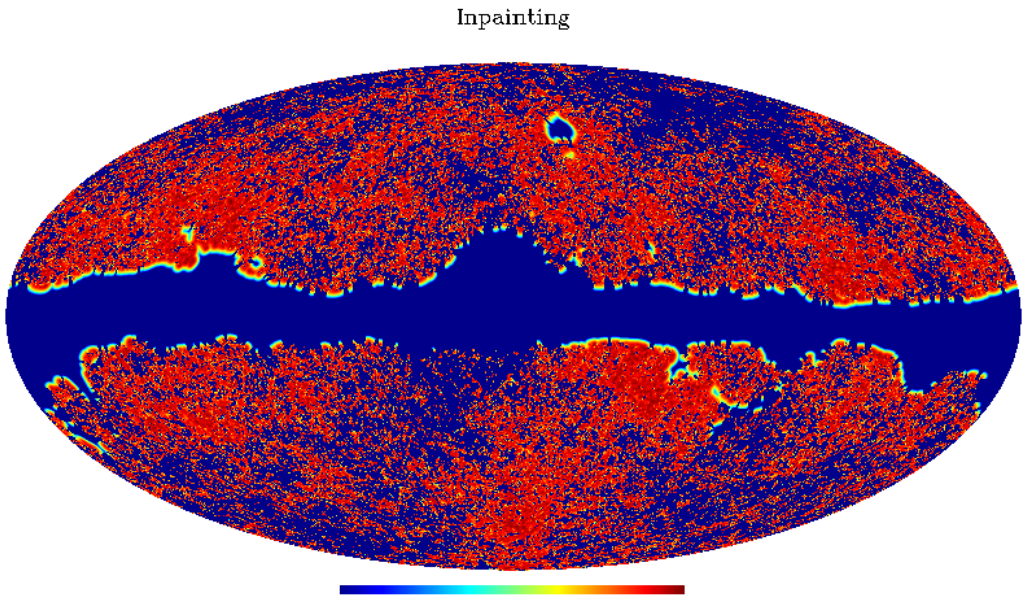

Figure 4.2: In this plot is showed the effect of the inpainting procedure on a masked CMB simulated map. The colors are in logarithmic scale to exaggerate the "rainbow" effect of the apodization at the border of the Galactic mask. The average procedure is done only 200 times to let some masked point-sources still visible on the map.

the mask to the unmasked regions during harmonic transforms.

Any bias and/or excess variance arising from the inpainting procedure were assessed through MC validation (see Chapter 5) and found to be negligible. Since the inpainting procedure is particularly simple to implement, easily allows inclusion of realistic correlated-noise models in the simulations, and retains optimality, we chose inpainting as our data filtering procedure for the $f_{\rm NL}$ analysis.

4.4 Non-primordial contributions to the CMB bispectrum

In this section we present the steps followed to account for and remove the main non-primordial contributions to CMB NG.

4.4.1 The Integrated Sachs-Wolfe-lensing bispectrum

One of the most relevant mechanisms that can generate NG from secondary CMB anisotropies is the coupling between weak lensing and the ISW effect. This is in fact the leading contribution to the CMB secondary bispectrum with a black-body spectrum(Giovi et al. 2005; Goldberg and Spergel 1999; Verde and Spergel 2002a).

Weak lensing of the CMB is caused by gradients in the matter gravitational potential that distorts the CMB photon geodesics. The ISW on the other hand arise because of time-varying gravitational potentials due to the linear and non-linear growth of structure in the evolving Universe. Both the lensing and the ISW effect are then related to the matter gravitational potential and thus are correlated phenomena. This gives rise to a non-vanishing 3-point correlation function. Furthermore, lensing is related to non-linear processes which are therefore non-Gaussian. A detailed description of the signal, which accounts also for the contribution from the early-ISW effect, can be found in Lewis (2012).

The ISW-lensing bispectrum takes the form:

$$B^{m_1 m_2 m_3}_{\ell_1 \ell_2 \ell_3} \equiv \langle a_{\ell_1 m_1} a_{\ell_2 m_2} a_{\ell_3 m_3} \rangle = \langle a^{\rm P}_{\ell_1 m_1} a^{\rm L}_{\ell_2 m_2} a^{\rm ISW}_{\ell_3 m_3} \rangle + 5 \text{ perm.}\,, \tag{4.24}$$

where P, L, and ISW indicate primordial, lensing and ISW contributions respectively. This becomes

$$B^{m_1 m_2 m_3\,(\mathrm{ISW-L})}_{\ell_1\ell_2\ell_3} = \mathcal{G}^{m_1 m_2 m_3}_{\ell_1\ell_2\ell_3} b^{\mathrm{ISW-L}}_{\ell_1\ell_2\ell_3}, \tag{4.25}$$

where $\mathcal{G}^{m_1 m_2 m_3}_{\ell_1\ell_2\ell_3}$ is the Gaunt integral and $b^{\mathrm{ISW-L}}_{\ell_1\ell_2\ell_3}$ is the reduced bispectrum given by

$$\begin{aligned} b^{\mathrm{ISW-L}}_{\ell_1\ell_2\ell_3} = & \frac{\ell_1(\ell_1+1) - \ell_2(\ell_2+1) + \ell_3(\ell_3+1)}{2} \\ & \times \tilde{C}^{\mathrm{TT}}_{\ell_1} C^{\mathrm{T}\phi}_{\ell_3} + (5 \text{ perm.})\,. \end{aligned} \tag{4.26}$$

Here $\tilde{C}^{\mathrm{TT}}_{\ell}$ is the lensed CMB power spectrum and $C^{\mathrm{T}\phi}_{\ell}$ is the ISW-lensing cross-power spectrum (Cooray and Hu 2000; Goldberg and Spergel 1999; Lewis 2012; Verde and Spergel 2002a) that expresses the statistical expectation of the correlation between the lensing and the ISW effect.

As shown in Hanson et al. (2009), Mangilli and Verde (2009), and Lewis et al. (2011), the ISW-lensing bispectrum can introduce a contamination in the constraints on primordial local NG from the CMB bispectrum. Both bispectra are maximal for squeezed or nearly squeezed configurations. The bias on a primordial f_{NL} (e.g., local) due to the presence of the ISW-lensing cross correlation signal is defined as:

$$\Delta f^{\mathrm{local}}_{\mathrm{NL}} = \frac{\hat{S}}{N}, \tag{4.27}$$

with

$$\hat{S} = \sum_{2\leqslant\ell_1\ell_2\ell_3} \frac{B^{\mathrm{ISW-L}}_{\ell_1\ell_2\ell_3} B^{\mathrm{P}}_{\ell_1\ell_2\ell_3}}{V_{\ell_1\ell_2\ell_3}}\,, \quad N = \sum_{2\leqslant\ell_1\ell_2\ell_3} \frac{\left(B^{\mathrm{P}}_{\ell_1\ell_2\ell_3}\right)^2}{V_{\ell_1\ell_2\ell_3}}, \tag{4.28}$$

where $B^{\mathrm{ISW-L}}$ and B^{P} refer respectively to the ISW-lensing and the primordial

Table 4.1: The bias in the three primordial $f_{\rm NL}$ parameters due to the ISW-lensing signal for the four component-separation methods.

	SMICA	NILC	SEVEM	C-R
Local	7.1	7.0	7.1	6.0
Equilateral	0.4	0.5	0.4	1.4
Orthogonal	−22	−21	−21	−19

bispectrum, and V is defined below Eq. (4.14).

The bias in the estimation of the three primordial $f_{\rm NL}$ from *Planck* is given in Table 4.1. As one can see, taking into account the $f_{\rm NL}$ statistical error bars shown, e.g., in Table 6.1, the local shape is most affected by this bias (at the level of more than $1\,\sigma_{\rm local}$), followed by the orthogonal shape (at the level of about $0.5\,\sigma_{\rm ortho}$), while the equilateral shape is hardly affected. In this thesis we have taken into account the bias reported in Table 4.1 by subtracting it from the measured $f_{\rm NL}$.[1]

The results for the amplitude of the ISW-lensing bispectrum from the different foreground-cleaned maps are given in Table 4.2. It should be noted that the binned and modal estimators are less correlated to the exact template for the ISW-lensing shape than they are for the primordial shapes, hence their larger error bars compared to KSW (which uses the exact template by construction (Mangilli et al. 2013)). The conclusion is that we detect the ISW-lensing bispectrum at a value consistent with the fiducial value of 1, at a significance level of $2.6\,\sigma$ (taking the SMICA-KSW value as reference). For details about comparisons between different estimators and analysis of the data regarding primordial shapes we refer the reader to Chapter 5 and Chapter 6.

We show in the top figure of Fig. 4.3 and Fig. (4.4) the measured skew-C_ℓ spectrum (see Sect. 4.2.2) for the SMICA map and for optimal detection of

[1] See Kim et al. (2013) for other debiasing techniques.

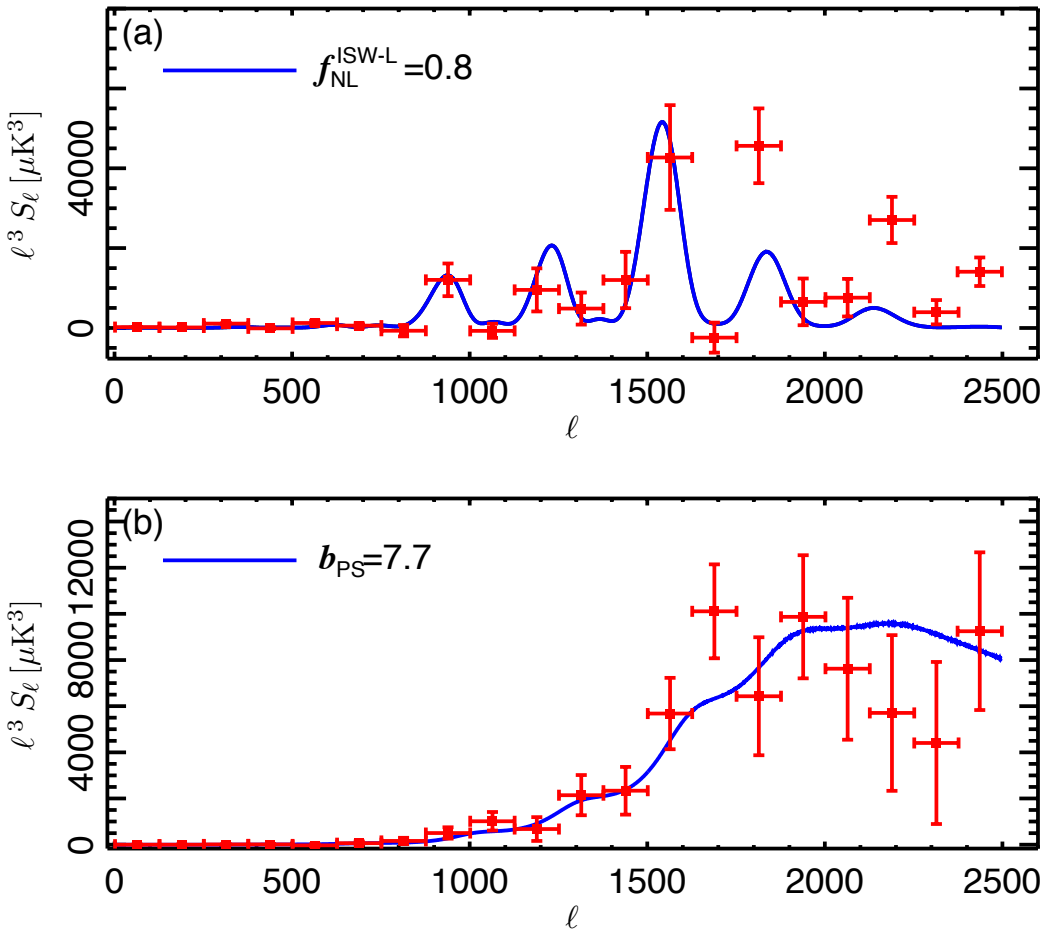

Figure 4.3: The binned skew-C_ℓ statistics from the SMICA map for (a) ISW-lensing and (b) Poisson point sources. Theoretical curves are not fitted to the data shown, but are plotted with the amplitude (the only free parameter) determined from the KSW technique. The Poisson point-source foreground is clearly detected, and the ISW-lensing skew-spectrum is evident for $\ell < 1750$, with a suggestion of another source of NG at high ℓ. b_{ps} is the Poisson point-source amplitude in dimensionless units of 10^{-29}, and f_{NL}^{ISW-L} is the ISW-lensing amplitude in units of that expected from the *Planck* best-fit cosmology. Note that error bars are from data-averaging, and as a consequence are underestimates. See (Planck Collaboration XXIV 2013).

Figure 4.4: ISW-lensing skew-C_ℓ spectra. Blu points are mean skew-C_ℓ from simulations; green is the theoretical skew-C_ℓ; red is the skew-C_ℓ extracted from SMICA. TOP: 300 Gaussian simulations. BOTTOM: 200 Lensed Gaussian simulations.

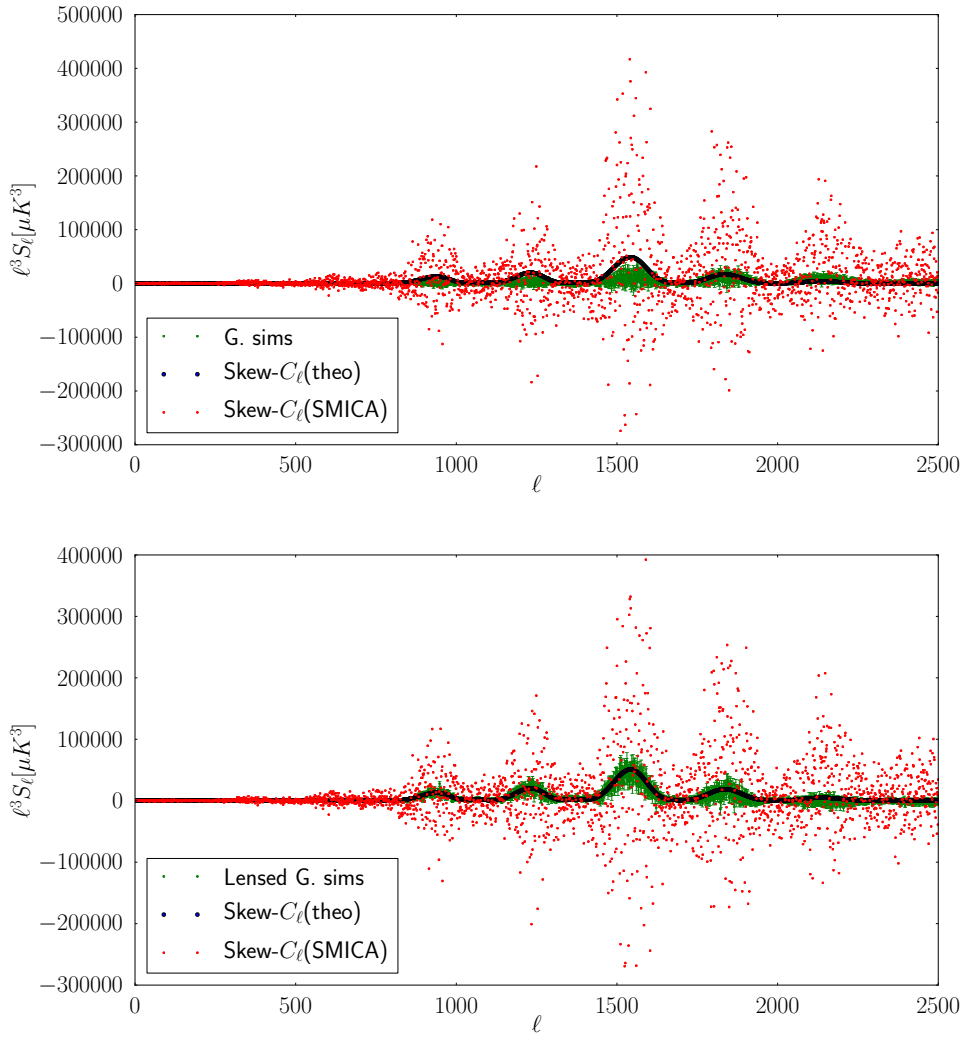

Table 4.2: Results for the amplitude of the ISW-lensing bispectrum from the SMICA, NILC, SEVEM, and C-R foreground-cleaned maps, for the KSW, binned, and modal (polynomial) estimators; error bars are 68% CL .

	SMICA	NILC	SEVEM	C-R
KSW	0.81 ± 0.31	0.85 ± 0.32	0.68 ± 0.32	0.75 ± 0.32
Binned . . .	0.91 ± 0.37	1.03 ± 0.37	0.83 ± 0.39	0.80 ± 0.40
Modal	0.77 ± 0.37	0.93 ± 0.37	0.60 ± 0.37	0.68 ± 0.39

the ISW-lensing bispectrum, along with the best-fitting estimates of $f_{\rm NL}$ from the KSW method for different values of ℓ. It should be noted that the skew-C_ℓ spectrum is *not* a fit to the KSW data points; its shape is fully fixed by the template under consideration, with only the overall amplitude as a free parameter. Hence the agreement between the curve and the points in the régime up to $\ell \sim 1750$ is good evidence that KSW is really detecting the ISW-lensing effect and not some other source of NG (although there might be some evidence of an additional NG contribution at $\ell > 1750$; note that point sources, at the level determined by their own skew-spectrum, do not contribute significantly to the ISW-lensing statistics, see the next subsection). See Planck Collaboration XVII (2013), Planck Collaboration XIX (2013) for further information about the detection by *Planck* of the ISW-lensing signal.

It is important to know that the KSW values in Table (4.2) were obtained using the skew-C_ℓ estimator. As already wrote earlier in this chapter, resumming the estimated skew-C_ℓ, e.g. Eq.(4.21), we obtain the same statistics as KSW. But, as explained in detail in Planck Collaboration XIX (2013), skew-C_ℓ has better convergence properties with respect to KSW in the case of ISW-lensing estimation. In fact, with 200 lensed Gaussian CMB simulations, we obtain a mean value of 0.85 ± 0.66 for KSW whereas using skew-C_ℓ we obtain 0.93 ± 0.29. The dif-

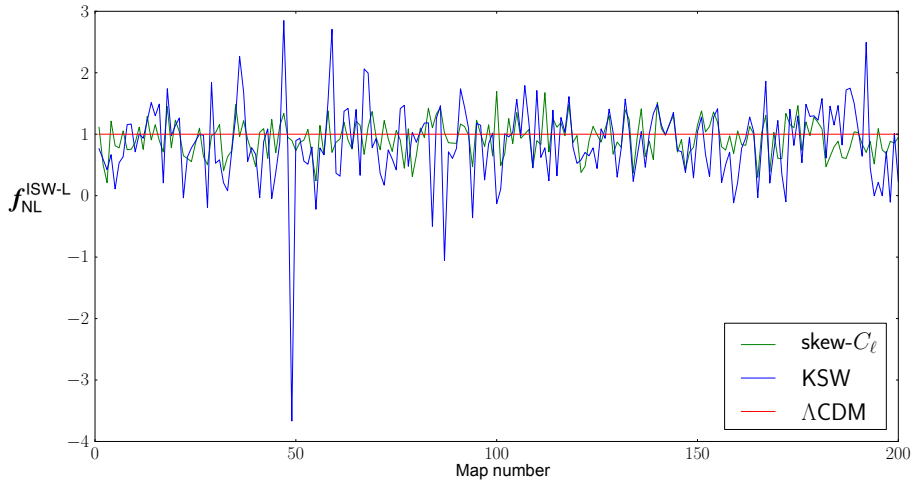

Figure 4.5: In this plot we show the ISW-lensing estimation with KSW and skew-C_ℓ algorithms on simulated Gaussian lensed maps. From ΛCDM model we expect a results equal 1 (red reference line). From the figure is clear how the KSW scatter (blue curve) is much higher than that of skew-C_ℓ (green line). This is a clear indication that 200 maps are too few for the KSW linear term to correctly converge. The results of skew-C_ℓ is validated and robust as can be seen in Planck Collaboration XIX (2013).

ference between the two estimators is clearly visible looking at Figure 4.5. The advantage of the skew-C_ℓ estimator over KSW will be useful in the next Planck release where, with more data, we would be able to estimate the ISW-lensing bispectrum with a nearly 3σ significance (see Chapter (6) for comments on future prospects).

4.4.2 Point-sources bispectrum

Extra-Galactic point sources at *Planck* frequencies are divided into two broad categories: radio sources with synchrotron and/or free-free emission; and infrared galaxies with thermal emission from dust heated by young stars. Radio sources are dominant at central CMB frequencies up to 143 GHz, and can be considered unclustered (González-Nuevo et al. 2005; Toffolatti et al. 1998). Hence their bispectrum is constant and is related to their number counts as

$$b_{\rm ps} = k_\nu^3 \int_0^{S_{\rm c}} S^3 \frac{dn}{dS} dS, \tag{4.29}$$

with S the flux density, dn/dS the number counts per steradiant, $S_{\rm c}$ the flux cut and k_ν the conversion factor from flux to relative temperature elevation, depending on the frequency and instrumental bandpass.

Infrared galaxies become important at higher frequencies, 217GHz and above, and are highly clustered in dark matter halos, which enhances their bispectrum on large angular scales (Curto et al. 2013; Lacasa et al. 2012). However, in the *Planck* context it was shown by Lacasa and Aghanim (2012) that the IR bispectrum is more than 90% correlated with the Poissonian template of the radio sources. So a joint estimation of $f_{\rm NL}$ with a Poissonian bispectrum template will essentially account for the IR signal, and provide quasi-identical values compared to an analysis accounting for the IR bispectrum template. Indeed, in our final optimal bispectrum constraints for primordial shapes, we will account for the potential contamination from point sources by jointly fitting primordial and Poisson templates to the data.

Our final measured point-source bispectrum amplitudes from the data are re-

ported in Table 4.3. The amplitude is expressed in dimensionless units, i.e., it has been divided by the appropriate power of the monopole temperature T_0, and has been multiplied by 10^{29}. As shown in Sect. 6.2.1, the Poisson template is the only one that still evolves significantly between $\ell = 2000$ and $\ell = 2500$. This explains the differences between the values of the KSW and binned (that use $\ell_{\rm max} = 2500$) and the modal (that uses $\ell_{\rm max} = 2000$) estimators. It has been shown that for the same value of $\ell_{\rm max}$ all three estimators agree very well (Planck Collaboration XXIV 2013).

We finally conclude from Table 4.3 that we detect the point-source bispectrum with high significance in the SMICA, NILC, and SEVEM cleaned maps, while it is absent from the C-R cleaned map. The measured skew-C_ℓ spectrum of the SMICA map in the bottom figure of Fig. (4.3) and Fig. (4.6) gives further evidence that the NG from foreground point sources is convincingly detected. The only degree of freedom in this plot is the amplitude, which is not set by a direct fit to the skew-C_ℓ, but rather is estimated by KSW. As a result, the good agreement with the shape of this skew-C_ℓ spectrum is powerful evidence that there is NG from point sources. However, this still turns out to be a negligible contaminant for primordial $f_{\rm NL}$ studies, due to the very low correlation between the Poisson bispectrum and the primordial shapes.

Figure 4.6: Point-sources skew-C_ℓ spectra. Blu points are mean skew-C_ℓ from simulations; green is the theoretical skew-C_ℓ; red is the skew-C_ℓ extracted from SMICA. TOP: 300 Gaussian simulations. BOTTOM: 200 Lensed Gaussian simulations. In those figures is clearly seen the residual point-sources contamination.

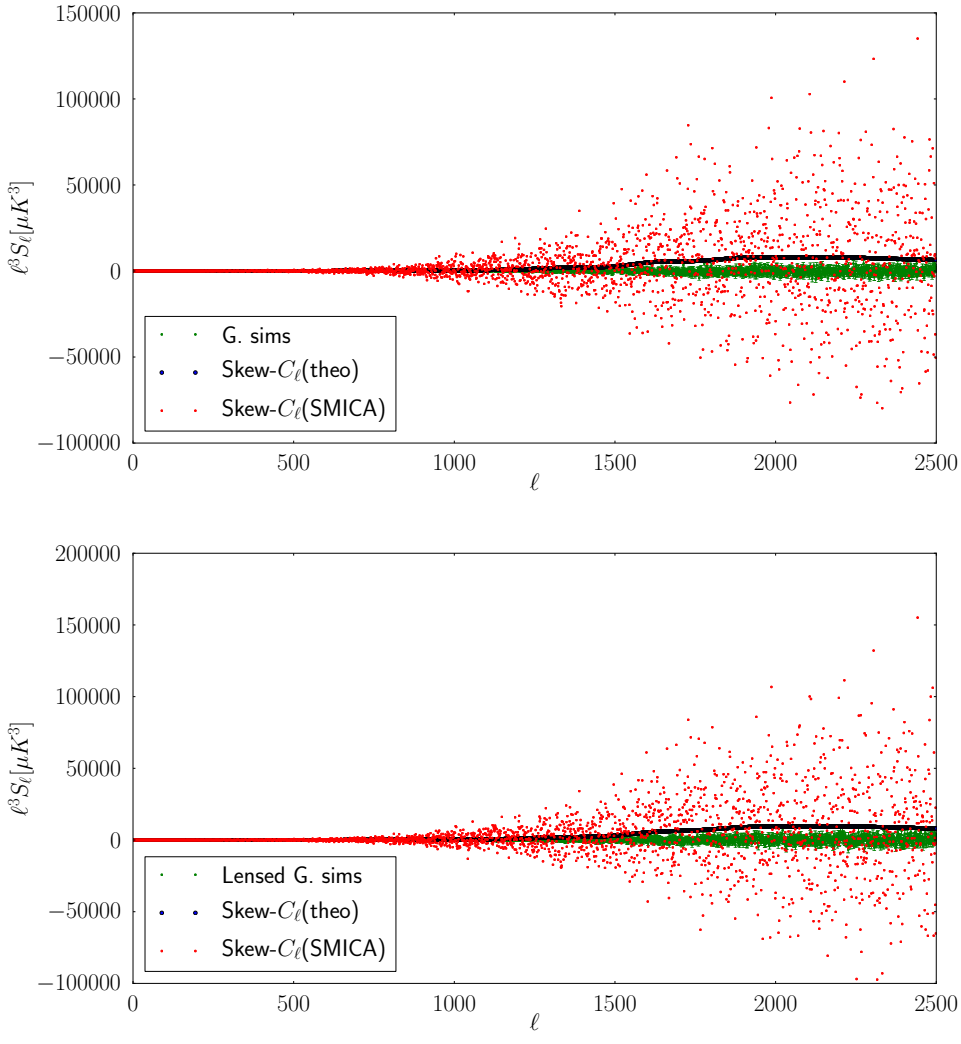

Table 4.3: Results for the amplitude of the point source (Poisson) bispectrum (in dimensionless units of 10^{-29}) from the SMICA, NILC, SEVEM, and C-R foreground-cleaned maps, for the KSW, binned, and modal (polynomial) estimators; error bars are 68% CL. Note that the KSW and binned estimators use $\ell_{\rm max} = 2500$, while the modal estimator has $\ell_{\rm max} = 2000$.

	SMICA	NILC	SEVEM	C-R
KSW	7.7 ± 1.5	9.2 ± 1.7	7.6 ± 1.7	1.1 ± 5.1
Binned	7.7 ± 1.6	8.2 ± 1.6	7.5 ± 1.7	0.9 ± 4.8
Modal	10 ± 3	11 ± 3	10 ± 3	0.5 ± 6

Chapter 5

Validation on simulated data

The $f_{\rm NL}$ results quoted in this thesis and in Planck Collaboration XXIV (2013) have all been cross-validated using multiple bispectrum-based estimators from different groups. Having multiple estimators was extremely useful for the entire analysis, for two main reasons. First, it allowed great improvement in the robustness of the final results. In the early stages of the work, the comparison between different independent techniques helped to resolve bugs and other technical issues in the various computer codes, while during the later stages it was very useful to understand the data and find the optimal way of extracting information about the various bispectrum templates. Secondly, besides these cross-checking purposes, different estimators provide also interesting complementary information, going beyond simple $f_{\rm NL}$ estimation. For example, the binned and modal estimators provide a reconstruction of the full bispectrum of the data (smoothed in different domains), the skew-C_ℓ estimator allows to monitor the contribution to $f_{\rm NL}$ from different sources of NG, the wavelets reconstruction allows $f_{\rm NL}$ directionality tests, and so on.

In this Chapter, we focus on the first point above, that is, the use of multiple bispectrum-based pipelines as a way to improve the robustness of the results. In particular, we will focus the attention on KSW and skew-C_ℓ estimators since were developed by the author of this thesis. For this purpose, a large amount of work was dedicated to the development and analysis of various test maps, in order to validate the estimators. This means not only checking that the various estimators recover the input $f_{\rm NL}$ within the expected errors, but also that the results agree on a map-by-map basis.

The Chapter is divided into two parts. Sect. 5.1 shows results on a set of initially full-sky, noiseless, Gaussian CMB simulations, to which we add, in several steps, realistic complications, including primordial NG, anisotropic coloured noise, and a mask, showing the impact on the results at each step. In Sect. 5.2, we show our results on a set of simulations that mimic the real data as closely as possible (except for the presence of foreground residuals, which will be studied in Sect. 6.2.4): no primordial NG, but NG due to the ISW-lensing effect; simulated instrumental effects and realistic noise; and simulations passed through the component separation pipelines. In fact these are the simulations that are used to determine the error bars for the final *Planck* results.

Here we will present only a small subset of the large number of validation tests that were performed. For example, we also had a number of "blind $f_{\rm NL}$ challenges", in which the different groups received a simulated data set with an unknown value of input $f_{\rm NL}$ for a given shape and they had to report their estimated values. In addition, different noise models were tested (white vs. coloured and isotropic vs. anisotropic), leading to the conclusion that it is important to make the noise in the estimator calibration as realistic as possible (coloured and

anisotropic). We also tested different Galactic and point source masks, with and without inpainting, concluding that it is best to fill in both the point sources and the Galactic mask, using a sufficient number of iterations in our diffusive procedure to entirely fill in the point source gaps, while at the same time only effectively apodizing the Galactic mask (no small-scale structure in its interior). There were also various tests on realistic simulations of *Planck* data, including detailed modelling of the *Planck* satellite, and the sky signals (Gaussian or non-Gaussian CMB and all foregrounds, provided by the PSM). These simulations were tested both before and after they passed through the component separation pipelines. In all comparison tests the results were consistent with input $f_{\rm NL}$ values and differences between estimators were consistent with theoretical expectations.

5.1 Validation of estimators in the presence of primordial non-Gaussianity

The aim of the first set of validation tests is threefold. First, we want to study the level of agreement from different estimators in ideal conditions (i.e., full-sky noiseless data). The expected scatter between measurements is, in this case, entirely due to the slightly imperfect correlation between weights of estimators that adopt different schemes to approximate the primordial shape templates. For this case the scatter can be computed analytically, and usually below an integer fraction of the scatter, like $1/3$ or $1/2$, see for example the Planck Collaboration XXIV (2013, Appendix). We can then verify that our results in ideal conditions match theoretical expectations. This is done in Sect. 5.1.1. Second, we want to make

sure that the estimators are unbiased and correctly recover $f_{\rm NL}$ in input for local, equilateral, and orthogonal shapes. This is done in Sects. 5.1.2 and 5.1.3, where a superposition of local, equilateral and orthogonal bispectra is included in the simulations and the three $f_{\rm NL}$ values are estimated both independently and jointly. Finally we want to understand how much the agreement between pipelines in ideal conditions is degraded when we include a realistic correlated noise component and a sky cut, thus requiring the introduction of a linear term in the estimators in order to account for off-diagonal covariance terms introduced by the breaking of rotational invariance. Since we want to study the impact of adding noise and masking separately, we will first work on a set of full-sky maps with noise in Sect. 5.1.2, and then add a mask in Sect. 5.1.3.

The tests that we are going to show were applied to the KSW, binned and modal estimators. These are three optimal bispectrum pipelines used to analyse *Planck* data in Chapt. 6. Our goal for this set of tests is not so much to attain the tightest possible agreement between methods, as it is to address the points summarized in the above paragraph. For this reason the estimator implementations used in this specific Section were slightly less accurate but faster to compute than those adopted for the final data analysis of Chapt. 6. The primary difference with respect to the main analysis is that a smaller number of simulations were used to calibrate the linear term (80–100 in these tests, as against 200 or more for the full analysis). For the modal estimator a faster expansion with a smaller number of modes was also used: 300 here versus 600 in the high accuracy version of the pipeline[1] used in Chapt. 6. Even with many fewer modes, the modal estimator

[1]While most of the modal results in this thesis come from the most accurate 600 modes pipeline, a few computationally intensive data validation tests of Sect. 6.2 also use the fast 300 modes version; therefore the results in this Section also provide a direct validation of the fast

is still quite accurate: the correlation coefficient for the modal expansion of the local template is 0.95, while for the equilateral and orthogonal shapes it is 0.98 (Planck Collaboration XXIV 2013).

A final comment is about the Skew-C_ℓ estimator. Even if we always refer to KSW numbers for $f_{\rm NL}$ analysis, this estimator was built in parallel with Skew-C_ℓ one. For a large amount of different analysis we explicitly checked that the $f_{\rm NL}$ obtained from Skew-C_ℓ was exactly the same as KSW with a difference $< 1/6\sigma$ for all the primordial shapes and point-sources. In Figure (5.1) is showed the $f_{\rm NL}$ difference between KSW and skew-C_ℓ for a set of 200 lensed maps with Gaussian CMB. This is true for all the primordial shapes and point sources contamination, yet in the case of ISW-lensing effect we saw in the previous chapter that the Skew-C_ℓ estimator had a faster convergence with respect to the KSW and is always used in the ISW-lensing analysis (the explanation of this, and the comparison with others estimators, can be found in Planck Collaboration XIX 2013).

5.1.1 Ideal Gaussian simulations

As a basis for the other tests we start with the ideal case, a set of 96 simulations of a full-sky Gaussian CMB, with a Gaussian beam with FWHM 5 arcmin and without any noise, cut off at $\ell_{\rm max} = 2000$ in our analyses. The independent Fisher matrix error bars in that case are 4.2 for local NG, 56 for equilateral, and 28 for orthogonal.

The purpose here is mostly aimed at checking consistency with the following formula (derived in Planck Collaboration XXIV 2013, Appendix) for the expected scatter (standard deviation) between $f_{\rm NL}$ results of the same map from an exact and

modal pipeline.

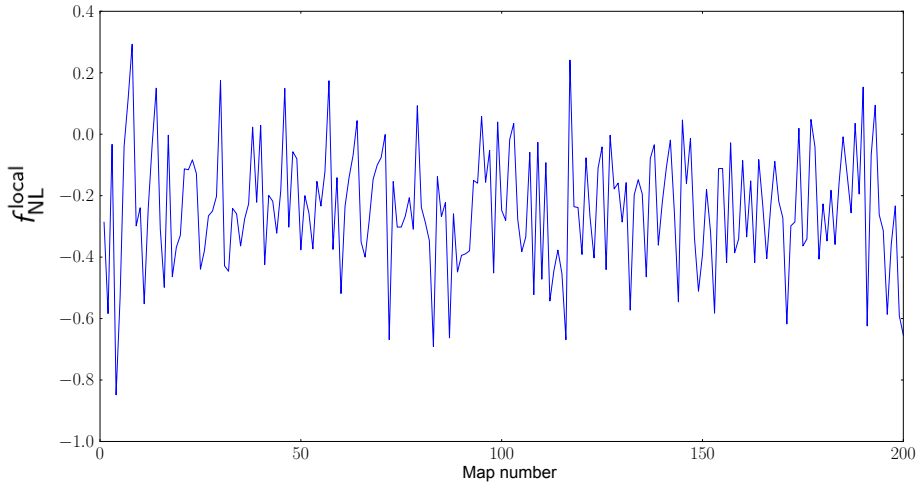

Figure 5.1: Map-by-map $f_{\rm NL}$ difference between KSW and skew-C_ℓ for the local shape. Since the standard deviation value for the set of 200 lensed simulations is $\sigma = 5.8$ we see that the difference between KSW and skew-C_ℓ is less than $1/6\sigma$.

an approximate estimator:

$$\sigma_{\delta f_{\rm NL}} = \Delta_{\rm th} \frac{\sqrt{1-r^2}}{r} \,. \tag{5.1}$$

Here $\Delta_{\rm th}$ is the standard deviation of the exact estimator and r is the correlation coefficient that gives the correlation of the approximate bispectrum template with the exact one, defined as

$$r \equiv \frac{\sum_{\ell_1 \le \ell_2 \le \ell_3} \frac{B^{\rm th}_{\ell_1\ell_2\ell_3} B^{\rm exp}_{\ell_1\ell_2\ell_3}}{g_{\ell_1\ell_2\ell_3} C_{\ell_1} C_{\ell_2} C_{\ell_3}}}{\sqrt{\sum_{\ell_1 \le \ell_2 \le \ell_3} \frac{(B^{\rm th}_{\ell_1\ell_2\ell_3})^2}{g_{\ell_1\ell_2\ell_3} C_{\ell_1} C_{\ell_2} C_{\ell_3}} \sum_{\ell_1 \le \ell_2 \le \ell_3} \frac{(B^{\rm exp}_{\ell_1\ell_2\ell_3})^2}{g_{\ell_1\ell_2\ell_3} C_{\ell_1} C_{\ell_2} C_{\ell_3}}}} \,, \tag{5.2}$$

Table 5.1: Results for $f_{\rm NL}$ for the set of ideal Gaussian simulations described in Sect. 5.1.1 for the KSW and modal estimators and for their difference, assuming all shapes to be independent.

Independent	KSW	Modal	Modal − KSW
Local	−0.5 ± 4.1	−0.5 ± 4.1	−0.0 ± 0.6
Equilateral	2.2 ± 48	1.3 ± 48	−0.9 ± 8.9
Orthogonal	−1.1 ± 29	−1.0 ± 30	0.1 ± 6.5

where the label "th" denotes the initial bispectrum shape which is used to fit to the data, and "exp" is the approximate expanded one. Note that this formula has been obtained under the simplifying assumptions of Gaussianity, full-sky coverage and homogeneous noise. For applications dealing with more realistic cases we might expect the scatter to become larger, while remaining qualitatively consistent.

The results averaged over the whole set of maps are given in Table 5.1 for the KSW and modal estimators individually, as well as for their difference. The plane wave modal expansion implemented here achieves about 98% correlation with the separable shapes used by KSW (Planck Collaboration XXIV 2013). According to the formula above we then expect a standard deviation of map-by-map differences of order $0.2\Delta_{f_{\rm NL}}$ for a given shape, where $\Delta_{f_{\rm NL}}$ is the corresponding $f_{\rm NL}$ error bar. Looking at the left-hand side of Table 5.1, we see that the error bars are 4 for local NG, 50 for equilateral, and 30 for orthogonal. So we predict a standard deviation of map-by-map differences of 0.8, 10 and 6 for local, equilateral, and orthogonal NG, respectively. As one can see from the "Modal-KSW" column, the measurements are in excellent agreement with the theoretical expectation.

Table 5.2: Results from the different estimators for $f_{\rm NL}$ for the set of full-sky non-Gaussian simulations described in Sect. 5.1.2. Both the results for the estimators individually and for the differences with KSW are given.

	KSW	Binned	Modal		Binned − KSW	Modal − KSW
Independent						
Local	13.8 ± 5.2	14.1 ± 5.2	14.1 ± 5.3	.....	0.3 ± 2.1	0.4 ± 2.6
Equilateral	63 ± 57	62 ± 58	64 ± 57	.....	−0.9 ± 20.1	1.0 ± 18.1
Orthogonal	−52 ± 37	−58 ± 40	−54 ± 37	.....	−6.0 ± 12.6	−2.2 ± 12.3
Joint						
Local	11.7 ± 6.2	12.0 ± 6.6	12.0 ± 6.4	.....	0.2 ± 2.7	0.2 ± 3.2
Equilateral	31 ± 59	29 ± 61	31 ± 59	.....	−1.8 ± 21.1	−0.2 ± 18.5
Orthogonal	−20 ± 43	−22 ± 47	−21 ± 42	.....	−2.1 ± 15.6	−0.6 ± 14.8

5.1.2 Gaussian simulations with realistic noise

A set of 96 full-sky non-Gaussian CMB simulations was created according to the process described by Fergusson et al. (2010a), with local $f_{\rm NL}^{\rm local} = 12$, equilateral $f_{\rm NL}^{\rm equil} = 35$, and orthogonal $f_{\rm NL}^{\rm ortho} = -22$. The effect of a 5 arcmin beam was added, as well as realistic coloured and anisotropic noise according to the specifications of the `SMICA` cleaned map. The independent Fisher matrix error bars in that case are 5.3 for local, 63 for equilateral, and 33 for orthogonal NG, while the joint ones are respectively 6.0, 64, and 37.

The results averaged over the whole set are given in Table 5.2 for the various estimators individually, as well as for the differences with respect to KSW. Compared to the previous case we now deviate from the exact theoretical expectation for two reasons: we include a realistic correlated noise component; and we have NG in the maps. The presence of NG in the input maps will lower the agreement between estimators with respect to the Gaussian case if the correlation between weights is not exactly 100%. This is even more true in this specific case, where

Table 5.3: Results from the different estimators for $f_{\rm NL}$ for the set of masked non-Gaussian simulations described in Sect. 5.1.3. Both the results for the estimators individually and for the differences with KSW are given.

	KSW	Binned	Modal		Binned − KSW	Modal − KSW
Independent						
Local	13.5 ± 7.1	13.1 ± 6.5	14.0 ± 6.8	.....	−0.3 ± 3.5	0.5 ± 4.6
Equilateral	55 ± 64	50 ± 59	58 ± 63	.....	−4.4 ± 24.1	3.3 ± 20.2
Orthogonal	−50 ± 45	−53 ± 46	−52 ± 45	.....	−3.5 ± 16.4	−1.9 ± 15.2
Joint						
Local	11.7 ± 8.3	11.4 ± 7.9	12.2 ± 8.4	.....	−0.3 ± 4.3	0.4 ± 5.7
Equilateral	23 ± 66	19 ± 59	24 ± 64	.....	−3.8 ± 27.7	1.7 ± 24.8
Orthogonal	−18 ± 51	−20 ± 54	−18 ± 55	.....	−1.3 ± 19.9	0.3 ± 20.4

NG of three different kinds is present in the input maps and also cross-correlation terms between different expanded shapes are involved (and propagated over in the joint analysis). Moreover, when noise is included the specific modal expansion used for this test is 95% correlated to the separable KSW local shape (so there is a 3% reduction of the correlation compared to the ideal case for the modal local shape), see Planck Collaboration XXIV (2013); we thus expect a further degradation of the level of agreement for this specific case. Finally, in order to correct for noise effects, a linear term has to be added to the estimators. Since the linear term is obtained by MC averaging over just 80 or 96 simulations in this test (depending on the estimator), MC errors are also adding to the measured differences. Of course, the MC error can be reduced by increasing the number of simulations in the linear term sample. We do this for the analysis of the real data and in Sect. 5.2, but it was computationally too expensive for this set of preliminary validation tests, so we decided here to just account for it in the final interpretation of the results.

As a consequence of the above, we can no longer expect the map-by-map $f_{\rm NL}$

Table 5.4: Results from the different estimators for $f_{\rm NL}$ for 99 maps from a set of realistic lensed simulations passed through the SMICA pipeline, described in Sect. 5.2. Both the results for the estimators individually and for the differences with KSW are given.

Independent	KSW	Binned	Modal	Wavelet	Binned − KSW	Modal − KSW	Wavelet − KSW
Local	7.6 ± 6.0	6.8 ± 5.8	7.7 ± 5.9	8.1 ± 8.4	−0.8 ± 1.2	0.1 ± 1.4	0.5 ± 6.4
Equilateral	4 ± 76	−1 ± 72	2 ± 76	−3 ± 76	−5 ± 20	−2 ± 13	−7 ± 91
Orthogonal	−21 ± 42	−20 ± 41	−21 ± 42	−15 ± 53	1.6 ± 11	−0.1 ± 8	6.4 ± 48

differences to follow perfectly the theoretical expectation, obtained in the previous Section in idealized conditions (full-sky, no noise, and Gaussianity). With these caveats in mind, the agreement between different pipelines remains very good, being about $0.3\,\sigma$ in most cases and about $0.5\,\sigma$ for the modal-KSW difference in the local case, which can be easily explained by the fact that this is the set of weights with the lowest correlation (95%, as mentioned above). All estimators are unbiased and recover the correct input values.

5.1.3 Impact of the mask

To the simulations of Sect. 5.1.2 we now apply the *Planck* union mask - denoted U73 - masking both the Galaxy and the brightest point sources and leaving 73% of the sky unmasked (Planck Collaboration XII 2013). This is the same mask used to analyse *Planck* data in Chapt. 6, see Planck Collaboration XXIV (2013). The independent Fisher matrix error bars in that case (taking into account the $f_{\rm sky}$ correction) are 6.2 for local NG, 74 for equilateral, and 39 for orthogonal, while the joint ones are respectively 7.1, 76, and 44.

All masked areas of the sky (both Galactic and point sources) are filled in with

a simple iterative method. In this simple inpainting method each pixel in the mask is filled with the average of all eight surrounding pixels, and this is repeated 2000 times over all masked pixels. The filling-in helps to avoid propagating the effect of a sharp edge and the lack of large-scale power inside the mask to the unmasked regions during harmonic transforms. This inpainting method is the one that was used to produce all NG results in this thesis for methods that need it (KSW, skew-C_ℓ).

The results averaged over the whole set of simulations are given in Table 5.3 for the various estimators individually, as well as for the differences with respect to KSW. The map-by-map results are shown in Fig. 5.2.

This is the most realistic case we consider in this set of tests. Besides noise, we also include a sky cut and our usual mask inpainting procedure. All the caveats mentioned for the previous case are still valid, and possibly emphasized by the inclusion of mask and inpainting. In the light of this, the agreement is still very good, worsening a bit with respect to the "full-sky + noise" case only for the local measurement, where the mask is indeed expected to have the biggest impact. In the joint analysis all estimators recover the correct input values for the local and orthogonal cases, but all estimators find a value for equilateral NG that is somewhat too low. It is unclear whether this is an effect of masking and inpainting on the equilateral measurement or just a statistical fluctuation for this set of simulations. In any case, this potential bias is small compared to the statistical uncertainty, so that it would not have a significant impact on the final results.

To summarize the results of this Sect. 5.1, we performed an extensive set of validation tests between different $f_{\rm NL}$ estimators using strongly, but not perfectly, correlated primordial NG templates in their weights. The test consisted in com-

paring the $f_{\rm NL}$ measured by the different estimators for different sets of simulations, on a map-by-map basis. We started from ideal conditions: full-sky Gaussian noiseless maps. In this case we computed a theoretical formula providing the expected standard deviation of the $f_{\rm NL}$ differences, as a function of the correlations between the input NG templates in the different estimators. Our results match this formula very well. In the other two simulation sets we added realistic features (noise, mask and inpainting) and we included a linear combination of local, equilateral and orthogonal NG. First of all we verified that all the pipelines correctly recover the three $f_{\rm NL}$ input values, hence they are unbiased. Moreover, we observed that adding such features produces an expected slight degradation of the level of agreement between different pipelines, that nevertheless remains very good: about 0.3–0.4 σ for equilateral and orthogonal NG, and about 0.5–0.6 σ for local NG, which is the shape most affected by mask and noise contamination.

5.2 Validation of estimators on realistic *Planck* simulations

In the tests of the previous Subsection we checked the bias of the estimators and studied their level of agreement, given the correlation between their weights, in the presence of noise and a sky cut. To speed up the computation while still retaining enough accuracy for the purposes of that analysis, we used a relatively small number of maps for linear term calibrations (80–100). In the present Subsection we instead try to simulate as accurately as possible real data analysis conditions. Our goal is to obtain an accurate MC-based expectation of the scatter between

different $f_{\rm NL}$ measurements when the pipelines are run on actual *Planck* maps.

To this aim we use FFP6 simulation maps described in (Planck Collaboration ES 2013). The original FFP6 maps were lensed using the `Lenspix` algorithm, and processed through the `SMICA` component separation pipeline. Then they were multiplied by the Galactic and point source mask U73 as in the actual $f_{\rm NL}$ analysis, and inpainted as usual. Since our final results show full consistency with Gaussianity for local, equilateral and orthogonal shapes, we do not include any primordial $f_{\rm NL}$ in these maps. We note that although the simulations were passed through `SMICA` in order to provide a realistic filtering of the data, they did not include any foreground components. The impact of foreground residuals will be studied separately in Sect. 6.2.4.

The configuration of all bispectrum pipelines was the same as used for the final data analysis, which implies a correlation of 99% or better between the weights of the KSW, binned and modal estimators. Linear terms were calibrated using 200 simulations, after verifying that this number allows accurate convergence for all the shapes. For those tests the wavelet bispectrum pipeline was also included (Planck Collaboration XXIV 2013). Although this last estimator turns out to be about 30% suboptimal and, in its current implementation, less correlated with the primordial templates than the other estimators, it does provide an additional interesting cross-check of our results by introducing another decomposition basis.

A comparison of the measured $f_{\rm NL}$ map-by-map for all shapes and estimators is shown in Fig. 5.3. As an overall figure of merit of the level of agreement achieved by different pipelines we take as usual the standard deviation of the map-by-map $f_{\rm NL}$ differences, $\sigma_{\delta_{f_{\rm NL}}}$. Table 5.4 shows that the final agreement between the three optimal pipelines (KSW, binned, and modal) is close to saturating the

ideal bound in Eq. (5.1) determined by the imperfect correlation of the weights, i.e., it varies from about once to twice $\sigma_{\delta_{f_{\rm NL}}} \simeq 0.15\,\Delta_{f_{\rm NL}}$ for an $r = 0.99$ correlation. This is very consistent with the level of agreement that we find between estimators for the final results from the data, providing a good indication that no spurious NG features are present in the actual data set when compared to our simulations. The level of agreement of wavelet estimator is of order $1\,\sigma$.

As we showed in Figure (5.1) all the results obtained in this chapter for KSW estimator are exactly valid for the skew-C_ℓ. This means that the optimal estimators for the *Planck* $f_{\rm NL}$ paper are indeed four.

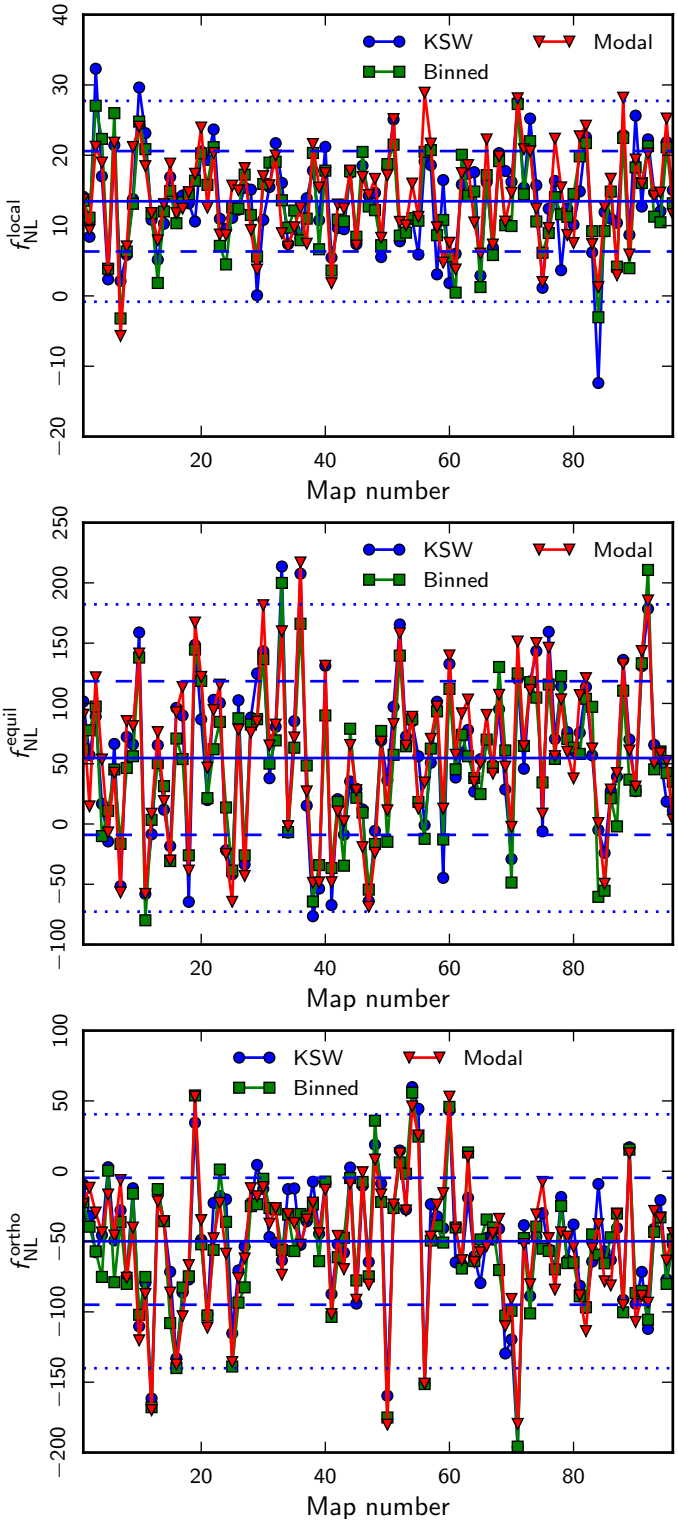

Figure 5.2: Map-by-map comparison of the results from the different estimators for local (top), equilateral (centre), and orthogonal (bottom) $f_{\rm NL}$ for the set of masked non-Gaussian simulations described in Sect. 5.1.3, assuming the shapes to be independent. The horizontal solid line is the average value of all maps for KSW, and the dashed and dotted horizontal lines correspond to 1σ and 2σ deviations, respectively.

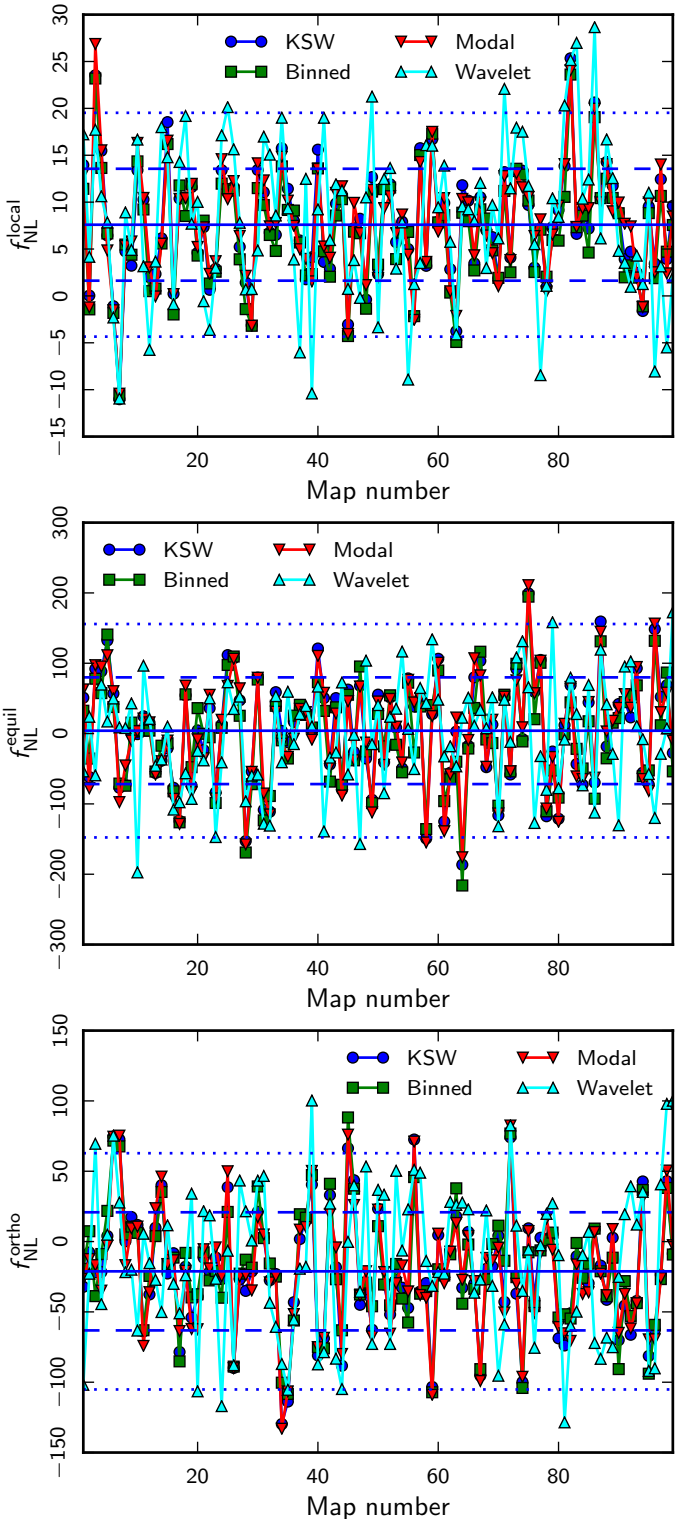

Figure 5.3: Map-by-map comparison of the results from the different estimators for local (top), equilateral (centre), and orthogonal (bottom) $f_{\rm NL}$ for 99 maps from a set of realistic lensed simulations passed through the SMICA pipeline, described in Sect. 5.2, assuming the shapes to be independent. The horizontal solid line is the average value of the maps for KSW, and the dashed and dotted horizontal lines correspond to 1σ and 2σ deviations, respectively.

Chapter 6

Results on Planck data

In this chapter we will show the results obtained from KSW and Skew-C_ℓ estimators. Moreover, when necessary, we will report the results of the companion estimators used in the *Planck* $f_{\rm NL}$ paper Planck Collaboration XXIV (2013). Those results will be necessary to illustrate the robustness of the final $f_{\rm NL}$ results.

For our analysis of *Planck* data we considered foreground-cleaned maps obtained with the four component separation methods `SMICA`, `NILC`, `SEVEM`, and `C-R`. For each map, $f_{\rm NL}$ amplitudes for the local, equilateral, and orthogonal primordial shapes have been measured. In the $f_{\rm NL}$ paper three bispectrum estimators are used (four on `SMICA`) , as described in Sect. B.3. The results can be found in Sect. 6.1. The estimators different than KSW and skew-C_ℓ use an expansion of the theoretical bispectrum templates in different domains, and truncate the expansion when a high level of correlation with the primordial templates is achieved. These decompositions, which are highly correlated with each other, are then matched to the data in order to extract $f_{\rm NL}$. The different expansions are all different implementations of the maximum-likelihood estimator given in Eq. (4.11). So the final

estimates are all expected to be optimal, and measure $f_{\rm NL}$ from nearly identical fitting templates. As discussed and tested in detail on simulations in Chapt. 5, central $f_{\rm NL}$ values from different methods are expected to be consistent with each other within about $0.3\sigma_{f_{\rm NL}}$. It is then clear that comparing outputs from both different estimators and different component separation methods, as we do, allows for stringent internal consistency checks and improved robustness of the final $f_{\rm NL}$ results.

Additionally, skew-C_ℓ method allow detection of possible NG features in the three-point function of the data that do not correlate significantly with the standard primordial shapes. A detection of such features would either produce a warning that some residual spurious NG effects are still present in the data or provide an interesting hint of "non-standard" primordial NG that is not captured by the local, equilateral and orthogonal shapes.

6.1 Constraints on local, equilateral and orthogonal $f_{\rm NL}$

Our goal here is to investigate the standard separable local, equilateral and orthogonal templates used e.g., in previous *WMAP* analyses (see e.g., Bennett et al. 2012b). When using the modal, binned, or wavelet estimator, these theoretical templates are expanded approximately (albeit very accurately) using the relevant basis functions or bins. On the other hand, the KSW and skew-C_ℓ estimators, by construction, works with the *exact* templates. Moreover, KSW was chosen by the *Planck* collaboration as the baseline to provide the final $f_{\rm NL}$ results for the

Table 6.1: Results for the $f_{\rm NL}$ parameters of the primordial local, equilateral, and orthogonal shapes, determined by the KSW estimator from the SMICA foreground-cleaned map. Both independent single-shape results and results marginalized over the point source bispectrum and with the ISW-lensing bias subtracted are reported; error bars are 68% CL.

	Independent	**ISW-lensing subtracted**
	KSW	KSW
SMICA		
Local	9.8 ± 5.8	**2.7 ± 5.8**
Equilateral	−37 ± 75	**−42 ± 75**
Orthogonal	−46 ± 39	**−25 ± 39**

standard shapes (local, equilateral, orthogonal), see Table 6.1.

There is an important note at this point regarding skew-C_ℓ estimator. We already said in the previous chapter that the KSW and skew-C_ℓ results are the same with respect to the primordial shapes. For the case of SMICA results we explicitly obtained the results for both KSW and skew-C_ℓ concluding again the extreme level of agreement between the two estimators. The primordial $f_{\rm NL}$ values obtained with skew-C_ℓ estimator for the SMICA map and their spectra are shown in Figure (6.1). Moreover, confronting the KSW and skew-C_ℓ results with both the binned and modal estimators we can achieve a remarkable level of cross-validation for our NG results.

We will be able to present consistent constraints for the local, equilateral and orthogonal models for all four *Planck* foreground-cleaned maps, using three independent optimal estimators (refer to Table 6.2). Regarding component separation methods, we adopt the SMICA map as the default for the final KSW results given its preferred status among foreground-separation techniques outlined by Planck Collaboration XII (2013). The other component separation maps will be used for important cross-validation of our results and to evaluate potential sen-

Table 6.2: Results for the $f_{\rm NL}$ parameters of the primordial local, equilateral, and orthogonal shapes, determined by the KSW, binned and modal estimators from the SMICA, NILC, SEVEM, and C-R foreground-cleaned maps. Both independent single-shape results and results marginalized over the point source bispectrum and with the ISW-lensing bias subtracted are reported; error bars are 68% CL .

	Independent			**ISW-lensing subtracted**		
	KSW	Binned	Modal	KSW	Binned	Modal
SMICA						
Local	9.8 ± 5.8	9.2 ± 5.9	8.3 ± 5.9	**2.7 ± 5.8**	2.2 ± 5.9	1.6 ± 6.0
Equilateral	−37 ± 75	−20 ± 73	−20 ± 77	**−42 ± 75**	−25 ± 73	−20 ± 77
Orthogonal	−46 ± 39	−39 ± 41	−36 ± 41	**−25 ± 39**	−17 ± 41	−14 ± 42
NILC						
Local	11.6 ± 5.8	10.5 ± 5.8	9.4 ± 5.9	4.5 ± 5.8	3.6 ± 5.8	2.7 ± 6.0
Equilateral	−41 ± 76	−31 ± 73	−20 ± 76	−48 ± 76	−38 ± 73	−20 ± 78
Orthogonal	−74 ± 40	−62 ± 41	−60 ± 40	−53 ± 40	−41 ± 41	−37 ± 43
SEVEM						
Local	10.5 ± 5.9	10.1 ± 6.2	9.4 ± 6.0	3.4 ± 5.9	3.2 ± 6.2	2.6 ± 6.0
Equilateral	−32 ± 76	−21 ± 73	−13 ± 77	−36 ± 76	−25 ± 73	−13 ± 78
Orthogonal	−34 ± 40	−30 ± 42	−24 ± 42	−14 ± 40	−9 ± 42	−2 ± 42
C-R						
Local	12.4 ± 6.0	11.3 ± 5.9	10.9 ± 5.9	6.4 ± 6.0	5.5 ± 5.9	5.1 ± 5.9
Equilateral	−60 ± 79	−52 ± 74	−33 ± 78	−62 ± 79	−55 ± 74	−32 ± 78
Orthogonal	−76 ± 42	−60 ± 42	−63 ± 42	−57 ± 42	−41 ± 42	−42 ± 42

sitivity to foreground residuals.

All the results presented in this Section were obtained using the union mask U73, which leaves 73% of the sky unmasked. The mask is the union of the confidence masks of the four different component separation methods, where each confidence mask defines the region where the corresponding CMB cleaning is trusted (see Planck Collaboration XII 2013). As it will be shown in Sect. 6.2.2, results are robust to changes that make the mask larger, but choosing a significantly smaller mask would leave some NG foreground contamination. For the linear term CMB and noise calibration, and error bar determination, we used sets

of realistic FFP6 maps that include all steps of data processing, and have realistic noise and beam properties (Planck Collaboration ES 2013). The simulations were also lensed using the `Lenspix`[1] algorithm and filtered through the component separation pipelines.

In Table 6.1 we show results for the combination of the KSW estimator and the `SMICA` map, at a resolution of $\ell_{\rm max} = 2500$. We present both "independent" single-shape results and "ISW-lensing subtracted" ones. The former are obtained by directly fitting primordial templates to the data. For the latter, two additional operations have been performed. In the first place, as the name indicates, they have been corrected by subtracting the bias due to the correlation of the primordial bispectra to the late-time ISW-lensing contribution (Hanson et al. 2009; Junk and Komatsu 2012; Mangilli and Verde 2009, see Sect. 4.4.1). In addition, a joint fit of the primordial shape with the (Poissonian) point source bispectrum amplitude extracted from the data has been performed on the results marked "ISW-lensing subtracted".[2] Instead of subtracting the ISW-lensing contribution there is the possibility to do a joint fit of all the shapes, both primordial and non. The results are shown in Table (6.4). In Kim et al. (2013) is shown that the subtraction of the bias from ISW-lensing do not bias the final results, and since in the joint fit the error bars are larger, the final results are obtained only with the subtraction methods described above.

A necessary quantity to do the joint analysis is the Fisher matrix entries. In Table (6.5) is shown the full-sky Fisher matrix with the input noise power-spectrum

[1] cosmologist.info/lenspix

[2] More precisely, in the subtracted ISW-lensing results the equilateral and orthogonal primordial shapes are also fitted jointly, although this has a nearly negligible impact on the final result because the two shapes are by construction nearly perfectly uncorrelated.

and the beam from SMICA map.

Since the ISW-lensing bispectrum is peaked on squeezed configurations, its impact is well known to be largest for the local shape. The ISW-lensing bias is also important for orthogonal measurements (there is a correlation coefficient $r \sim -0.5$ between the local and orthogonal CMB templates), while it is very small in the equilateral limit. The values of the ISW-lensing bias we subtract, summarized in Table 4.1, are calculated assuming the *Planck* best-fit cosmological model as our fiducial model. The same fiducial parameters were of course consistently used to compute the theoretical bispectrum templates and the estimator normalization. Regarding the point source contamination, we detect a Poissonian bispectrum at high significance in the SMICA map, see Sect. 4.4.2. However, marginalizing over point sources still carries a nearly negligible impact on the final primordial $f_{\rm NL}$ results, because the Poisson bispectrum template has very small correlations with all the other shapes.

Another important point with respect to the KSW and skew-C_ℓ analysis it the number of points used to calculate the real space integrals forming the cubic statistics for both KSW and skew-C_ℓ, e.g. Eq.(4.16) for KSW and Eq.(4.22) for skew-C_ℓ. We optimize the numbers of points by using the algorithm described in Smith and Zaldarriaga (2011b). The conformal distance r of the points and weights for SMICA are shown in Table (6.6). Without this optimization the $f_{\rm NL}$ analysis for *Planck* would be harder.

In light of the discussion at the beginning of this section, we take the numbers from the KSW SMICA analysis in Table 6.1 as *the* final local, equilateral and orthogonal $f_{\rm NL}$ constraints for the current *Planck* data release. These results clearly show that no evidence of NG of the local, equilateral or orthogonal type is found

in the data. After ISW-lensing subtraction, all $f_{\rm NL}$ for the three primordial shapes are consistent with 0 at 68% CL. Note that these numbers have been cross-checked using two completely independent KSW pipelines, one of which is an extension to *Planck* resolution of the pipeline used for the *WMAP* analysis (Bennett et al. 2012b).

Unlike other methods, the KSW technique is not designed to provide a reconstruction of the full bispectrum of the data. However, the related skew-C_ℓ statistic described in Sect. 4.2.2 allows, for each given shape, visualization and study of the contribution to the measured $f_{\rm NL}$ from separate ℓ-bins. This is a useful tool to study potential spurious NG contamination in the data. We show for the `SMICA` map in Fig. 6.1 the measured skew-C_ℓ spectrum for optimal detection of primordial local, equilateral and orthogonal NG, along with the best-fitting estimates of $f_{\rm NL}$ from the KSW method for different values of ℓ. Again, in Figures (6.2), (6.3) and (6.4) we shown the same results tested against the simulations. Contrary to the case of the point source and ISW-lensing foregrounds (see Sect. 4.4), the skew-C_ℓ statistics do not show convincing evidence for detection of the primordial shapes. In particular the skew-spectrum related to primordial local NG does not have the right shape, suggesting that whatever is causing this NG signal is not predominantly local. Again, point sources contribute very little to this statistics; ISW-lensing contributes, but only a small fraction of the amplitude, so there are indications of additional NG which are not captured by these foregrounds. In any event the estimators are consistent with no primordial signal of the types considered.

As mentioned before, our analysis went beyond the simple application of the KSW estimator to the `SMICA` map. All $f_{\rm NL}$ pipelines developed for *Planck* analysis

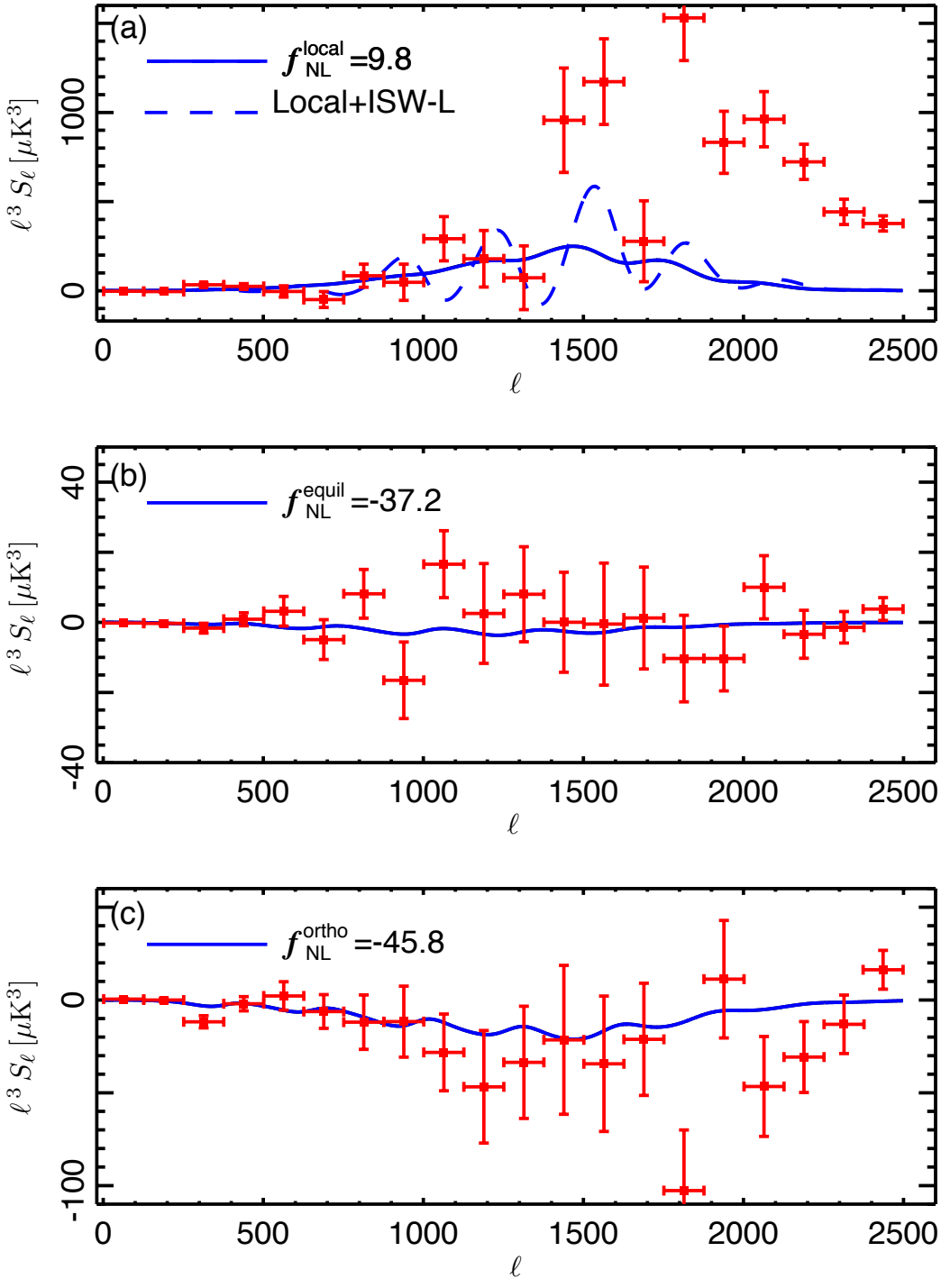

Figure 6.1: Binned skew-C_ℓ statistics from the SMICA map for (a) local, (b) equilateral, and (c) orthogonal. Theoretical curves are not fitted to the data shown, but are plotted with the amplitude (the only free parameter) determined from the KSW technique. The dashed line shows the ISW-lensing contribution to the local statistic. There is no evidence for detection of primordial NG. Note that the error bars are underestimated, as they ignore data correlations.

Figure 6.2: Local skew-C_ℓ spectra. Blu points are mean skew-C_ℓ from simulations; green is the theoretical skew-C_ℓ; red is the skew-C_ℓ extracted from SMICA. TOP: 300 Gaussian simulations. BOTTOM: 200 Lensed Gaussian simulations. In the Gaussian simulations the estimated mean skew-C_ℓ spectrum exploit a strange behaviour at high-ℓ that needs a more careful investigation.

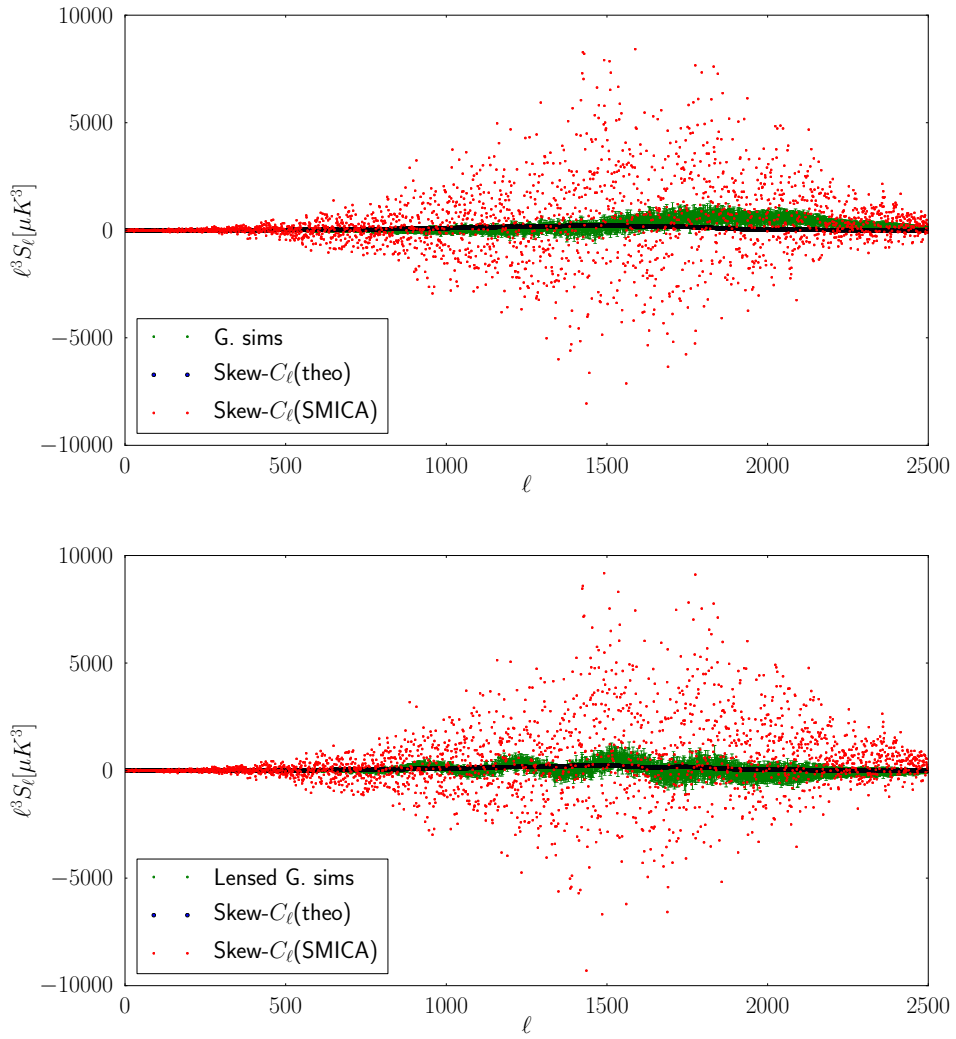

Figure 6.3: Equilateral skew-C_ℓ spectra. Blu points are mean skew-C_ℓ from simulations; green is the theoretical skew-C_ℓ; red is the skew-C_ℓ extracted from SMICA. TOP: 300 Gaussian simulations. BOTTOM: 200 Lensed Gaussian simulations.

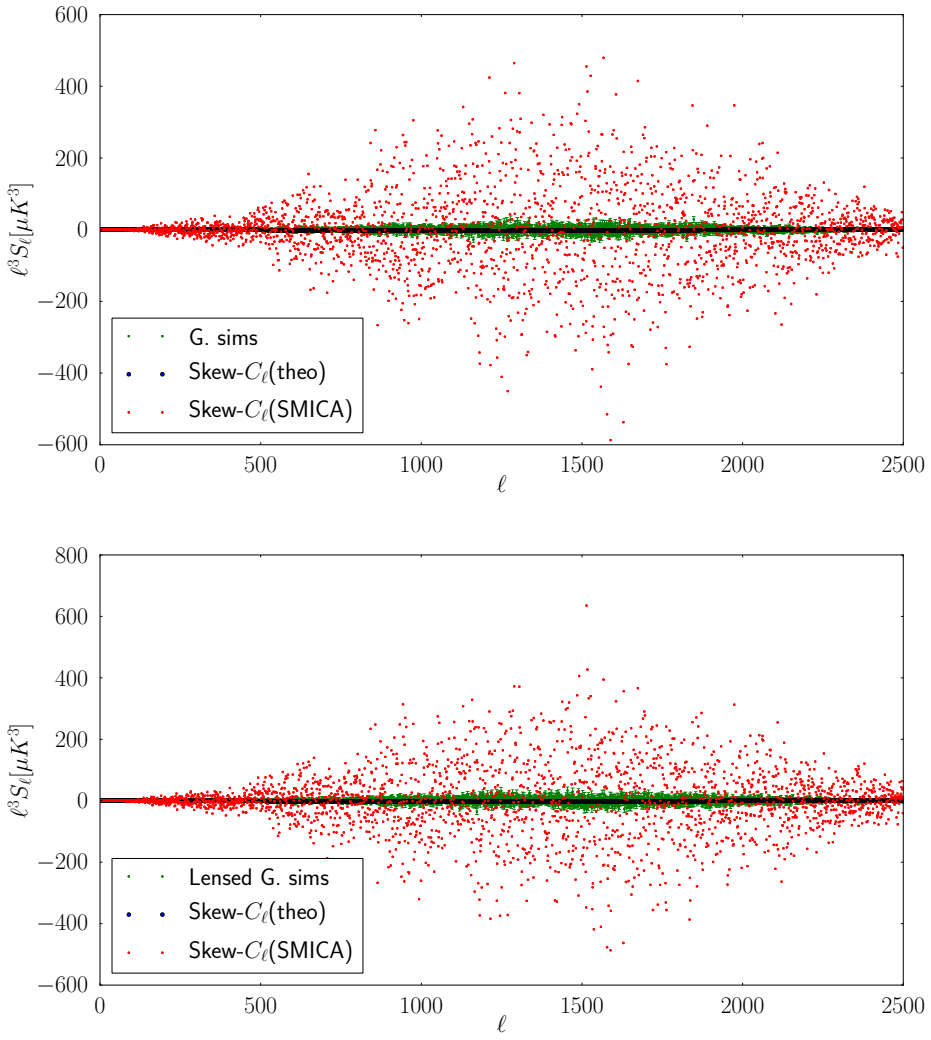

Figure 6.4: Orthogonal skew-C_ℓ spectra. Blu points are mean skew-C_ℓ from simulations; green is the theoretical skew-C_ℓ; red is the skew-C_ℓ extracted from SMICA. TOP: 300 Gaussian simulations. BOTTOM: 200 Lensed Gaussian simulations.

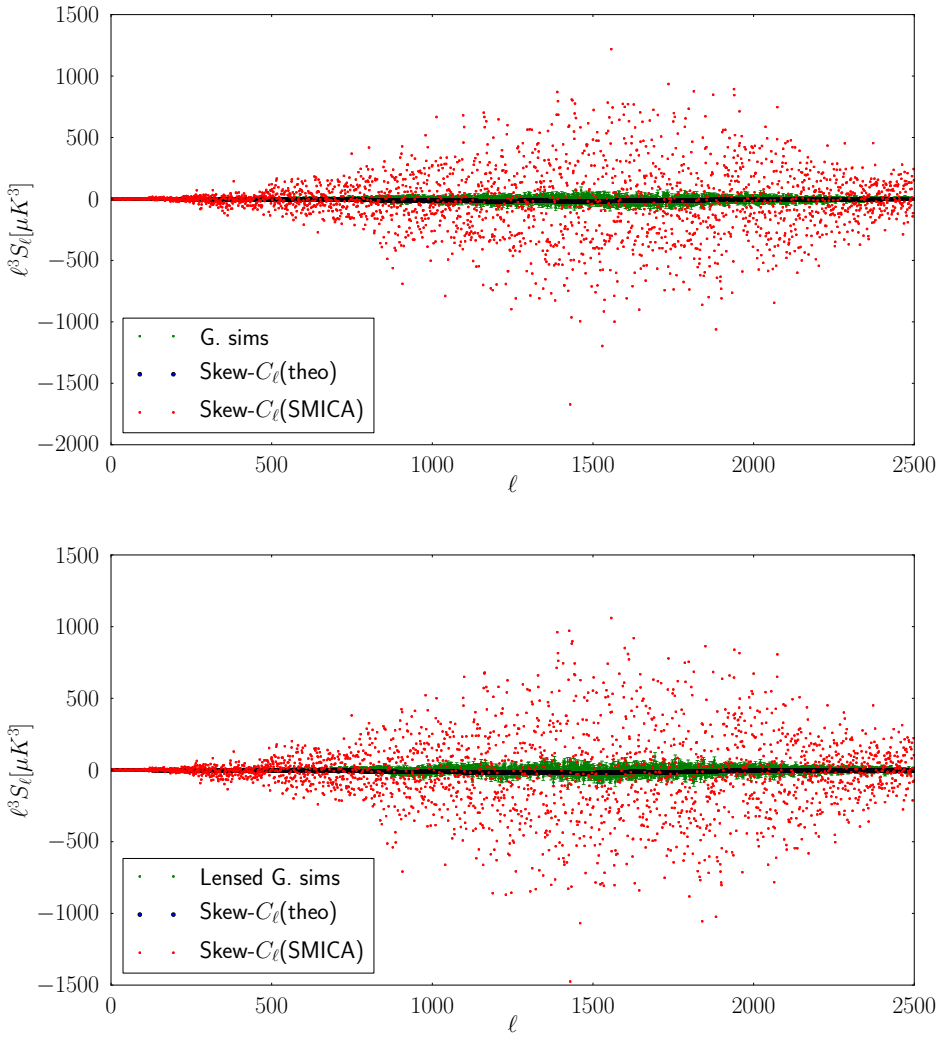

were actually applied to all component-separated maps by SMICA, NILC, SEVEM, and C-R. We found from simulations in the previous Sections that the KSW, skew-C_ℓ, binned, and modal pipelines saturate the Cramér-Rao bound, while the wavelet estimator in its current implementation provides slightly suboptimal results. Wavelets remain however a useful cross-check of the other methods, also given some technical complementarities, e.g., they are the only approach that does not require inpainting, as explained in Sect. B.3. Hence wavelet results were included in *Planck*'s results, but only for SMICA (see Planck Collaboration XXIV (2013)). The $f_{\rm NL}$ results for the optimal KSW, binned and modal bispectrum estimators, for the four component separation methods, are summarized in Table 6.2, one of the main products of our analysis of *Planck* data. The wavelet bispectrum analysis of SMICA is reported in Table 6.3. In the analysis, the KSW and binned bispectrum estimators considered multipoles up to $\ell_{\rm max} = 2500$, while the modal estimator went to $\ell_{\rm max} = 2000$. As shown in Sect. 6.2.1 and Table 6.7, error bars and central values for the three primordial shapes have converged at $\ell_{\rm max} = 2000$, so the final primordial $f_{\rm NL}$ estimates from the three pipelines are directly comparable (Planck Collaboration XXIV 2013).

The high level of agreement between results from the KSW, skew-C_ℓ, binned and modal $f_{\rm NL}$ estimators, and from all the component separation pipelines, is representative of the robustness of our results with respect to residual foreground contamination, and is fully consistent with our preliminary MC analysis shown in Chapt. 5. The scatter with wavelets is a bit larger, but this was expected due to the suboptimality of the wavelet estimator and is also in agreement with our MC expectations from the tests (Planck Collaboration XXIV 2013). Therefore wavelets do provide another successful cross-check.

6.2 Validation of *Planck* results

Here we perform a set of tests to check the robustness and stability of our $f_{\rm NL}$ measurements. As these are validation tests of *Planck* results, and not internal comparisons of bispectrum pipelines (already shown to be in tight agreement in Chapt. 5) not all the bispectrum estimators were employed on each test in the $f_{\rm NL}$ *Planck* paper (Planck Collaboration XXIV 2013). In general two estimators were used on each test, in order to have a cross-check of the outcomes without excessive redundancy (Planck Collaboration XXIV 2013).

In the following will be reported all the tests where KSW or skew-C_ℓ estimators are used. Note however, that some results from the *Planck*'s paper will be shown even if they are done by modal and binned estimator for two main reason. First, since KSW and skew-C_ℓ are heavily cross-validated with both modal and binned estimators, we are confident that the results can be translated to the estimators developed in this thesis. Second, KSW was explicitly used to check the consistency in the case of local $f_{\rm NL}$ estimation in the 143GHz channel, and with the big mask ($f_{\rm sky} = 0.32$) showing fully consistency.

6.2.1 Dependence on maximum multipole number

The dependence on the maximum multipole number $\ell_{\rm max}$ of the `SMICA` results (assuming independent shapes) is shown in Fig. 6.5 (for the binned estimator) and Table 6.7 (for both the KSW and binned estimators). Testing the $\ell_{\rm max}$ dependence is easiest for the binned estimator, where one can simply omit the highest bins in the final sum when computing $f_{\rm NL}$. It is clear that we have reached convergence both for the values of $f_{\rm NL}$ and for their error bars at $\ell_{\rm max} = 2500$, with the possible

exception of the error bars of the diffuse point source bispectrum. The diffuse point source bispectrum template is dominated by equilateral configurations at high ℓ. Moreover, for all the shapes except point sources, results at $\ell_{\rm max} = 2000$ are very close to those at $\ell_{\rm max} = 2500$, taking into account the size of the error bars.

It is very interesting to see that at $\ell_{\rm max} \sim 500$ we find a local $f_{\rm NL}$ result in very good agreement with the *WMAP*-9 value of 37.2 ± 19.9 (Bennett et al. 2012b). At these low $\ell_{\rm max}$ values we also find negative values for orthogonal $f_{\rm NL}$, although not as large or significant as the *WMAP*-9 value (which is -245 ± 100). One can clearly see the importance of the higher resolution of *Planck* both for the values of the different $f_{\rm NL}$ parameters and for their error bars.

It is also clear that the higher resolution of *Planck* is absolutely crucial for the ISW-lensing bispectrum; this is simply undetectable at *WMAP* resolution. On the other hand, the high sensitivity of *Planck* measurements also exposes us to a larger number of potentially spurious effects. For example we see that the bispectrum of point sources is also detected at high significance by *Planck* at $\ell_{\rm max} \geq 2000$, while remaining undetectable at lower resolutions. The presence of this bipectrum in the data could in principle contaminate our primordial $f_{\rm NL}$ measurements. For this reason, the presence of a large point source signal has been accounted for in previous Sections by always including the Poisson bispectrum in a joint fit with primordial shapes. Fortunately, it turns out that the very low correlation between the primordial templates and the Poisson one makes the latter a negligible contaminant for $f_{\rm NL}$, even when the residual point source amplitude is large.

6.2.2 Dependence on the mask and consistency between frequency channels

To test the dependence on the mask, the SMICA maps were analysed applying four different masks. Firstly the union mask U73 used for the final results at beginning of this chapter, which leaves 73% of the sky unmasked. Secondly was used the confidence mask CS-SMICA89 of the SMICA technique, which leaves 89% of the sky. Next, a bigger mask constructed by multiplying the union mask U73 with the *Planck* Galactic mask CG60, leading to a mask that leaves 56% of the sky. And finally a very large mask, leaving only 32% of the sky, which is the union of the mask CL31 - used for power spectrum estimation on the raw frequency maps - with the union mask U73 (for mask details see Planck Collaboration XII 2013 for U73, CS-SMICA89, and CG60; Planck Collaboration XV 2013 for CL31). The results of this analysis are presented in Table 6.8 for two different estimators: binned and modal. As previously said, the KSW results are fully consistent with the cases where it was applied (143GHz channel with the biggest mask for $f_{\rm NL}^{\rm Local}$). Here the $f_{\rm NL}$ are assumed independent . In order to correctly interpret our results and conclusions, an important point to note is that binned results have been obtained choosing $\ell_{\rm max} = 2500$, while modal results correspond to $\ell_{\rm max} = 2000$. Primordial shape and ISW-lensing results and error bars saturate at $\ell_{\rm max} = 2000$ (see Sect. 6.2.1), so the results from the two estimators are directly comparable in this case. The Poisson (point sources) bispectrum is however dominated by high-ℓ equilateral configurations and the signal for this specific template still changes from $\ell = 2000$ to $\ell = 2500$. The differences in central values and uncertainties between the two estimators for the Poisson shape are fully consistent with the dif-

ferent $\ell_{\rm max}$ values. Direct comparisons on data and simulations between these two estimators and the KSW estimator shown that Poisson bispectrum results match each other very well when the same $\ell_{\rm max}$ is used (Planck Collaboration XXIV 2013).

Results from the modal pipeline have uncertainties determined from MC simulations, while the results from the binned pipeline (in Table 6.8 and the next only) are given with Fisher error bars. It is very interesting to see that even with the large $f_{\rm sky} = 0.32$ mask, the simple inpainting technique still allows us to saturate the (Gaussian) Cramér-Rao bound, except for the ISW-lensing shape where we have a significant detection of NG in a squeezed configuration (so that an error estimate assuming Gaussianity is not good enough).

Besides confirming again the good level of agreement between the two estimators already discussed in Chapt. 5 and Chapt. 6, the main conclusion drawn from this analysis is that our measurements for all shapes are robust to changes in sky coverage, taking into account the error bars and significance levels, at least starting from a certain minimal mask. The $f_{\rm sky} = 0.89$ mask is probably a bit too small, likely leaving foreground contamination around the edges of the mask, though even for this mask the results are consistent within 1σ, except for point sources (which might suggest the presence of residual Galactic point source contamination for the small mask). The results from the $f_{\rm sky} = 0.73$ and $f_{\rm sky} = 0.56$ masks are highly consistent. This conclusion does not really change when going down to $f_{\rm sky} = 0.32$, although uncertainties of course start increasing significantly for this large mask (Planck Collaboration XXIV 2013).

We also investigated if there is consistency between frequency channels when the largest mask with $f_{\rm sky} = 0.32$ is used, and if these results agree with the `SMICA`

results obtained with the common mask. The results (assuming independent $f_{\rm NL}$) are given both for the binned and the modal estimator in Table 6.9. Again the KSW estimator results were fully consistent with the 143GHz channel results obtained by both modal and binned estimators. As one can see here, and was also checked explicitly in many other cases, the error bars from different estimators are perfectly consistent with each other and saturate the Cramér-Rao bound (except in the case of a significant non-Gaussian ISW-lensing detection).

A detailed analysis of Table 6.9 might actually suggest that the agreement between the two estimators employed for this test, although still clearly good, is slightly degraded when compared to their performance on clean maps from different component separation pipelines. If we compare e.g., `SMICA` results in Table 6.8 to raw data results in Table 6.9, we see that in the former case the discrepancy between the two estimators is at most of order $\sigma_{f_{\rm NL}}/3$, and smaller in most cases. In the latter case, however, we notice several measurements displaying differences of order $\sigma_{f_{\rm NL}}/2$ between the two pipelines, and the value of $f_{\rm NL}^{\rm ortho}$ at 70 GHz is 1σ away. We explain these larger differences as follows. For `SMICA` runs the estimator linear terms were calibrated using FFP6 simulations, accurately reproducing noise properties and correlations. On the other hand, for the tests on raw frequency channels a simple noise model was adopted , based on generating uncorrelated noise multipoles with a power spectrum as extracted from the half-ring null map, and remodulating the noise in pixel space according to the hit-count distribution. This approximation is expected to degrade the accuracy of the linear term calibration, and thus to produce a slightly lower agreement of different pipelines for shapes where the linear correction is most important. Those are the shapes that take significant contributions from squeezed triangles: local and ISW-

lensing, and to a smaller but non-negligible extent orthogonal, i.e., exactly the shapes for which we find slightly larger differences.

We can conclude that no significant fluctuations are observed when comparing measurements from different frequency channels (between themselves or with the clean and co-added SMICA map) or from different estimators on a given channel for the primordial shapes. The same is true for the ISW-lensing shape, although it should be noted that in particular the 70 GHz channel (like *WMAP*) does not have sufficient resolution to measure either the lensing or point source contributions. The uncertainties of the point source contribution vary significantly between frequency channels, although results remain consistent between channels given the error bars (when all multipoles up to $\ell_{\rm max} = 2500$ are taken into account, as performed by the binned estimator). This is due to the fact that this shape is dominated by high-ℓ equilateral configurations, the signal-to-noise of which depends crucially on the beam and noise characteristics, which vary from channel to channel. In the SMICA map point sources are partially removed by foreground cleaning, explaining the significantly lower value than for 217 GHz. As explained before, differences between the binned and modal estimators regarding point sources are due to the different values of $\ell_{\rm max}$ (2500 for binned and 2000 for modal), which particularly affects the 217 GHz channel and the SMICA cleaned map (Planck Collaboration XXIV 2013).

6.2.3 Null tests

To make sure there are no hidden NG in the instrumental noise, we performed a set of tests on null maps. These are noise-only maps obtained from differences

between maps with the same sky signal. In the first place we constructed half-ring null maps, i.e., maps constructed by taking the difference between the first and second halves of each pointing period, divided by 2. Secondly, we constructed a survey difference map (Survey 2 minus Survey 1 divided by 2). A "survey" is defined as half a year of data, roughly the time needed to scan the full sky once; the nominal period of *Planck* data described by these papers contains two full surveys. Finally we constructed the detector set difference map ("detset 1" minus "detset 2" divided by 2). The four polarized detectors at each frequency from 100 to 353 GHz are split into two detector sets per frequency, in such a way that each set can measure all polarizations and the detectors in a set are aligned in the focal plane (see Planck Collaboration VI (2013) and Planck Collaboration XII (2013) for details on the null maps analysed in this Section).

All these maps are analysed using the union mask U73 used for the final data results. However, in the case of the survey and detector set difference maps this mask needs to be increased by the unseen pixels. That effect only concerns a few additional pixels for the detector set null map, but is particularly important for the survey difference map, since a survey only approximately covers the full sky. The final $f_{\rm sky}$ of the mask used for the survey difference map is 64%.

The test consisted of extracting $f_{\rm NL}$ from the null maps described above, using only the cubic part of the bispectrum estimators (i.e., no linear term correction), and keeping the same weights as for the full "signal + noise" analysis. This means that the weights were not optimized for noise-only maps, as our aim was not to study the bispectrum of the noise per se but rather to check whether the noise alone produces a three-point function detectable by our estimators when they are run in the *same* configuration as for the actual CMB data analysis. For a similar

reason it would be pointless to introduce a linear term in this test. The purpose of the linear correction is in fact that of decreasing the error bars by accounting for off-diagonal covariance terms introduced by sky cuts and noise correlations when optimal weights are used, which is not the case here.

Our $f_{\rm NL}$ error bars for this test are obtained by running the estimators' cubic part on Gaussian noise simulations including realistic correlation properties. In the light of the above paragraph it is clear that such uncertainties have nothing to do with the actual uncertainties from CMB data, and cannot be compared to them.

Since SMICA was the main component-separation method for our final analysis of data, we present in Table 6.10 the results of our SMICA half-ring study using the KSW, binned and modal estimators, i.e., all the three main pipelines used in this thesis. For the cleaned maps we do not have survey or detector set difference maps.

As one can see *Planck* passes these null tests without any problems: all values found for $f_{\rm NL}$ in these null maps are completely negligible compared to the final measured results on the data maps, and consistent with zero within the error bars.

6.2.4 Impact of foreground residuals

In this chapter we applied different bispectrum estimators to *Planck* data filtered through four different component separation methods: SMICA, NILC, SEVEM and C-R , as we already mentioned (for a detailed description of component separation techniques used for *Planck* see Planck Collaboration XII (2013)). The resulting set of $f_{\rm NL}$ measurements shows very good internal consistency both between different estimators (as expected from our MC validation tests of bispec-

trum pipelines described in Chapt. 5) and between different foreground-cleaned maps. This already makes it clear that foreground residuals in the data are very well under control, and their impact on the final $f_{\rm NL}$ results is only at the level of a small fraction of the measured error bars. In this Section we further investigate this issue, and validate our previous findings on data by running extensive tests in which we compare simulated data sets with and without foreground residuals from two different component separation pipelines, `SMICA` and `NILC`. The goal is to provide a MC-based assessment of the expected $f_{\rm NL}$ systematic error from residual foreground contamination.

For each component separation pipeline, we consider two sets of simulations. One set includes realistic *Planck* noise and beam, is masked and inpainted in the same way as we do for real data, and is processed through `SMICA` and `NILC` but it does *not* contain any foreground component. The other set is obtained by adding to the first one a number of diffuse foreground residuals: thermal and spinning dust components; free-free and synchrotron emission; kinetic and thermal SZ; CO lines and correlated CIB. These residuals have been evaluated by applying the component separation pipelines to accurate synthetic *Planck* datasets including foreground emission according to the PSM (Delabrouille et al. 2012), and are of course dependent on the cleaning method adopted. The simple procedure of adding foreground residuals to the initially clean simulations is made possible because we consider only linear component separation methods for our analysis. Linearity is in general an important requirement for foreground cleaning algorithms aiming at producing maps suitable for NG analyses. All maps in both samples are lensed using the `LensPix` algorithm. We analyse both sets using different bispectrum estimators (modal, KSW, skew-C_ℓ and binned) for cross-validation

purposes.

The presence of residual foreground components in the data can have two main effects on the measured $f_{\rm NL}$. The first is to introduce a bias in the $f_{\rm NL}$ measurements due to the correlation between the foreground and primordial 3-point function for a given shape. The second is to increase the error bars while leaving the bispectrum estimator asymptotically unbiased. This is a consequence of accidental correlations between primordial CMB anisotropies and foreground emission. Of course these "CMB-CMB-foregrounds" bispectrum terms average to zero but they do not cancel in the bispectrum variance 6-point function). An interesting point to note is that a large foreground three-point function will tend to produce a *negative* bias in the local bispectrum measurements. That is because foreground emission produces a positive skewness of the CMB temperature distribution ("excess of photons"), and a positive skewness is in turn related to a negative $f_{\rm NL}^{\rm local}$ [3]. A large negative $f_{\rm NL}^{\rm local}$ is thus a signature of significant foreground contamination in the map. This is indeed what we observe if we consider raw frequency maps with a small Galactic cut, which is why our frequency-by-frequency analysis in Sect. 6.2.2 was performed using a very large mask. For more details regarding effects of foreground contamination on primordial NG measurements in the context of the *WMAP* analysis see Yadav and Wandelt 2008 and Senatore et al. 2010.

In the tests showed in this chapter we used maps contaminated with foreground residuals by simply adding residual components to the clean maps. That means that the difference $(f_{\rm NL}^{\rm residual} - f_{\rm NL}^{\rm clean})_i$ for the i-th realization in the simulated sam-

[3] While not rigorous, this argument captures the leading effect since Galactic foregrounds predominantly contaminate large scales. In principle, positively skewed, small scale foreground residuals ($\ell > 60$), or the negatively skewed SZ effect, can contribute positive bias. Our simulations with foreground residuals demonstrate that these contributions are subdominant.

ple exactly quantifies the change in $f_{\rm NL}$ due to foregrounds on that realization. In order to assess the level of residual foreground contamination on primordial and ISW-lensing shapes, first of all we considered the difference between average values and standard deviations of $f_{\rm NL}$ measured from the two map samples for each shape. As shown in Table 6.11, neither the average nor the standard deviation shown a significant change between the two datasets. That means that foreground residuals are clearly sub-dominant, as they do not bias the estimator for any shape and they do not increase the variance through spurious correlations with the CMB primordial signal (Planck Collaboration XXIV 2013).

The difference $f_{\rm NL}^{\rm residual} - f_{\rm NL}^{\rm clean}$ on a map-by-map basis was also considered and we compute its standard deviation. This is used as an estimate of the expected bias on a single realization due to the presence of residuals. As already expected from the negligible change in the standard deviations of the two samples, the variance of the map-by-map differences is also very small: Table 6.11 again shows that it is at most about $\sigma_{f_{\rm NL}}/6$ for any given shape, where $\sigma_{f_{\rm NL}}$ is the $f_{\rm NL}$ standard deviation for that shape. As an example, in Fig. 6.6 we show the measured values of $f_{\rm NL}^{\rm local}$ for the first 99 maps in both the `SMICA` and `NILC` samples, comparing results with and without residuals. It is evident also from this plot that the change in central value due to including residuals is very small. The very good agreement between the two component separation pipelines is also worth notice.

From the study shown here and from the comparison between different component separation methods in Chapt. 6, we can thus conclude that the combination of foreground-cleaned maps and $f_{\rm sky} = 0.73$ sky coverage we adopt in this work provide a very robust choice for $f_{\rm NL}$ studies.

Table 6.3: Results for the $f_{\rm NL}$ parameters of the primordial local, equilateral, and orthogonal shapes, determined by the suboptimal wavelet estimator from the SMICA foreground-cleaned map. Both independent single-shape results and results marginalized over the point source bispectrum and with the ISW-lensing bias subtracted are reported; error bars are 68% CL. As explained in the text, our current wavelets pipeline performs slightly worse in terms of error bars and correlation to primordial templates than the other bispectrum estimators, but it still provides a useful independent cross-check of other techniques.

	Independent	**ISW-lensing subtracted**
	Wavelets	Wavelets
SMICA		
Local	10 ± 8.5	0.9 ± 8.5
Equilateral	89 ± 84	90 ± 84
Orthogonal	-73 ± 52	-45 ± 52

Table 6.4: In this table is shown the $f_{\rm NL}$ estimation from SMICA map, for a joint analysis of all the shapes with respect to independent analysis.

KSW	Independent	Joint
Local	9.8 ± 5.8	4.3 ± 6.4
Equilateral	-37 ± 75	-53 ± 77
Orthogonal	-46 ± 39	-20 ± 42
Diff.ps(10^{29})	7.7 ± 1.5	7.7 ± 1.5
ISW-lensing	0.81 ± 0.31	0.75 ± 0.33

Table 6.5: Fisher matrix, full-sky and with noise and beam from SMICA map.

	Loc	Equi	Ortho	Diff.ps(10^{29})	ISWL
Loc	4.1e-2	6.8e-4	-2.9e-3	2.6e-4	2.9e-1
Equi	6.8e-4	2.6e-4	-1.3e-5	1.2e-4	9.1e-5
Ortho	-2.9e-3	-1.3e-5	1.1e-3	2.5e-05	-2.2e-2
Diff.ps(10^{29})	2.6e-4	1.2e-4	2.5e-05	6.6e-1	-1.2e-2
ISWL	2.9e-1	9.1e-5	-2.2e-2	-1.2e-2	28

Table 6.6: Optimal weights for SMICA map for primoridial shapes. The conformal distance r is in Mpc units. Practically all the information needed for primoridal shapes comes from recombination ($r\tilde{1}4000$Mpc). The rows are not ordered.

$r_{\rm Loc}$	$\rm Weights_{Loc}$	$r_{\rm Equi}$	$\rm Weights_{Equi}$	$r_{\rm Ortho}$	$\rm Weights_{Ortho}$
1.3926e+04	1.0889	1.3940e+04	1.0591	1.3954e+04	0.99710
1.3968e+04	0.99801	1.3968e+04	1.0046	1.3996e+04	1.0005
1.3996e+04	1.0003	1.4010e+04	1.0000	1.4319e+04	16.536
1.4010e+04	1.0000	1.3912e+04	1.5121	1.3898e+04	0.79325
1.3786e+04	0.78770	1.4446e+04	93.407	1.4053e+04	1.0058
1.4039e+04	0.99850	1.3996e+04	0.99991	1.3982e+04	0.99957
1.3982e+04	1.0005	1.3828e+04	-1.2277	1.4010e+04	1.0001
1.3954e+04	1.0070	1.3982e+04	0.99854	1.3814e+04	0.57898
1.3898e+04	1.5823	1.4039e+04	0.99558	1.4024e+04	1.0002
1.4024e+04	0.99902	1.4024e+04	1.0010	1.3926e+04	0.96853
1.3856e+04	-0.16989	1.4165e+04	11.656	1.4039e+04	1.0006
1.4067e+04	2.0778	1.4053e+04	0.99860	1.4081e+04	2.3632
1.3730e+04	3.9550	1.3954e+04	0.98325	1.3968e+04	1.0012
1.3940e+04	0.97422	1.4460e+04	-78.194	1.3856e+04	1.9740
1.4053e+04	0.97189	1.3884e+04	2.3252	1.3702e+04	-4.0213
1.3393e+04	6.1937	1.3814e+04	3.0665	1.3294e+04	29.184
1.3814e+04	2.4267	1.3252e+04	53.109	1.3940e+04	1.0096
1.3870e+04	2.2648	1.4067e+04	1.1675	1.4123e+04	0.26339
1.3589e+04	16.322	1.3716e+04	1.5951	1.3758e+04	2.4414
1.3772e+04	2.1482	1.3842e+04	2.5297	1.3800e+04	1.0257
1.3070e+04	19.355	1.3730e+04	2.5064	1.3589e+04	12.378
1.3912e+04	0.74291	1.3926e+04	0.80728	1.4151e+04	7.5586
1.3842e+04	1.9071	1.3786e+04	0.53155	1.3912e+04	1.0868
1.2227e+04	24.751	1.3631e+04	11.441	1.3828e+04	1.7686
1.4123e+04	0	1.3772e+04	2.2912	1.3870e+04	0.2784
1.4109e+04	0	1.4081e+04	1.6088	1.3028e+04	16.941
1.4095e+04	0	1.2410e+04	-17.964	1.3687e+04	5.1880
1.4081e+04	0	1.3856e+04	0.87737	1.3786e+04	1.4480
1.4305e+04	0	1.4221e+04	0	1.3716e+04	4.7636
1.4263e+04	0	1.4305e+04	0	1.3884e+04	1.4224
1.4390e+04	0	1.4347e+04	0	1.4067e+04	0.68559

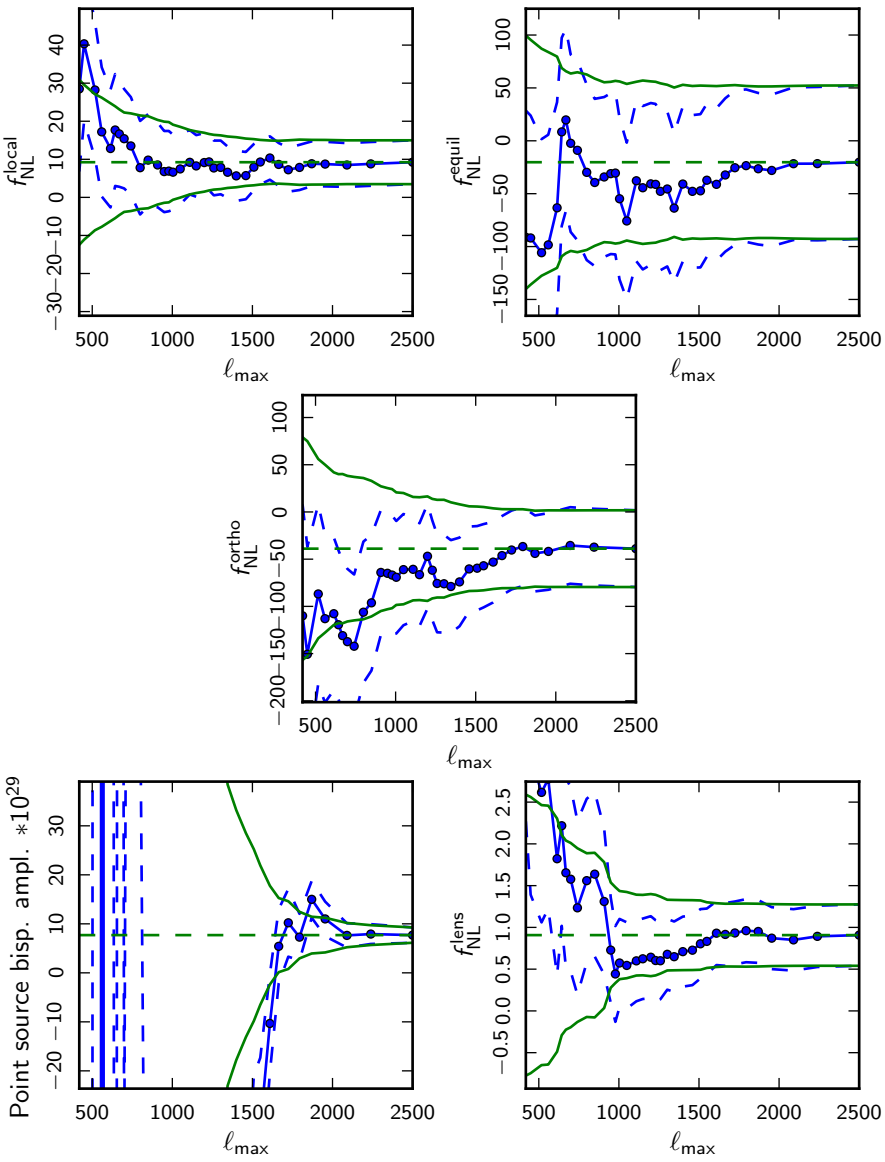

Figure 6.5: Evolution of the $f_{\rm NL}$ parameters (solid blue line with data points) and their uncertainties (dashed lines) for the five bispectrum templates as a function of the maximum multipole number $\ell_{\rm max}$ used in the analysis. From left to right and top to bottom the figures show respectively local, equilateral, orthogonal, diffuse point sources, and ISW-lensing. To better show the evolution of the uncertanties, they are also plotted around the final value of $f_{\rm NL}$ (solid green lines without data points). The results are for `SMICA`, assume all shapes to be independent, and have been determined with the binned bispectrum estimator. Those results are shown since are fully compatible with KSW and skew-C_ℓ estimators as can be seen in Table 6.7.

Table 6.7: Results for $f_{\rm NL}$ (assumed independent) of the SMICA cleaned map using different values of $\ell_{\rm max}$, for the KSW and binned estimators.

KSW	$\ell_{\rm max} = 500$	$\ell_{\rm max} = 1000$	$\ell_{\rm max} = 1500$	$\ell_{\rm max} = 2000$	$\ell_{\rm max} = 2500$
Local	38 ± 18	6.4 ± 9.7	6.9 ± 6.2	9.1 ± 5.8	9.8 ± 5.8
Equilateral	-119 ± 121	-45 ± 88	-41 ± 75	-40 ± 75	-37 ± 75
Orthogonal	-163 ± 109	-89 ± 52	-57 ± 45	-45 ± 40	-46 ± 39
Diff.ps $\cdot 10^{29}$	$(-1.5 \pm 1.3)\times 10^4$	$(-7.9 \pm 3.1)\times 10^2$	-39 ± 18	10.0 ± 3.1	7.7 ± 1.5
ISW-lensing	3.2 ± 1.2	1.00 ± 0.43	1.00 ± 0.35	0.83 ± 0.31	0.81 ± 0.31
Binned					
Local	33 ± 18	6.6 ± 9.8	7.1 ± 6.1	8.5 ± 5.9	9.2 ± 5.9
Equilateral	-95 ± 107	-55 ± 77	-47 ± 72	-22 ± 73	-20 ± 73
Orthogonal	-102 ± 94	-69 ± 58	-60 ± 44	-35 ± 40	-39 ± 41
Diff.ps $\cdot 10^{29}$	$(-1.4 \pm 1.2)\times 10^4$	$(-8.2 \pm 2.9)\times 10^2$	-42 ± 17	9.9 ± 2.9	7.7 ± 1.6
ISW-lensing	2.6 ± 1.6	0.57 ± 0.52	0.80 ± 0.42	0.85 ± 0.38	0.91 ± 0.37

Table 6.8: Results for $f_{\rm NL}$ (assumed independent) of the SMICA cleaned map using different masks as described in the main text (Sect. 6.2.2). Results are given for the binned and modal estimators. Uncertainties for the binned estimator in this table and the next are Fisher error bars. Both estimators were used in a degraded version for faster analysis ((Planck Collaboration XXIV 2013)).

Binned	$f_{\rm sky} = 0.89$	$f_{\rm sky} = 0.73$	$f_{\rm sky} = 0.56$	$f_{\rm sky} = 0.32$
Local	13 ± 5.4	9.2 ± 5.9	11 ± 6.8	6.1 ± 8.9
Equilateral	35 ± 66	-20 ± 73	-20 ± 83	39 ± 109
Orthogonal	-18 ± 36	-39 ± 39	-45 ± 45	-5 ± 59
Diff.ps · 1e29 . .	14.0 ± 1.3	7.7 ± 1.4	9.0 ± 1.7	10.3 ± 2.2
ISW-lensing . . .	0.69 ± 0.26	0.91 ± 0.29	0.84 ± 0.33	0.81 ± 0.43
Modal				
Local	12.1 ± 5.5	8.4 ± 6.0	12.3 ± 7.1	9.2 ± 8.7
Equilateral	52 ± 66	-56 ± 72	-31 ± 84	42 ± 104
Orthogonal	3.3 ± 35	-31 ± 40	-50 ± 47	-27 ± 59
Diff.ps · 1e29 . .	20.6 ± 2.5	11.4 ± 2.8	10.7 ± 3.2	12.7 ± 3.9
ISW-lensing . . .	0.42 ± 0.35	0.62 ± 0.40	1.1 ± 0.45	0.80 ± 0.48

Table 6.9: Results for $f_{\rm NL}$ (assumed independent) for the raw frequency maps at 70, 100, 143, and 217 GHz with a very large mask ($f_{\rm sky}$ = 0.32) compared to the SMICA result with the union mask U73 ($f_{\rm sky}$ = 0.73), as determined by the binned (with $\ell_{\rm max}$ = 2500) and modal (with $\ell_{\rm max}$ = 2000) estimators. The same caveats as for the previous table (Table 6.8) apply here as well (Planck Collaboration XXIV 2013).

	SMICA	70 GHz	100 GHz	143 GHz	217 GHz
Binned					
Local	9.2 ± 5.9	19.7 ± 26.0	−2.5 ± 13.2	10.4 ± 9.8	−4.7 ± 9.6
Equilateral	−20 ± 73	159 ± 188	70 ± 132	48 ± 114	−9 ± 114
Orthogonal	−39 ± 39	−78 ± 139	−106 ± 81	−101 ± 64	−84 ± 63
Diff.ps · 1e29	7.7 ± 1.4	(−1.4 ± 2.3)×10^3	−4.0 ± 64	8.7 ± 6.1	14.2 ± 3.0
ISW-lensing	0.91 ± 0.29	3.5 ± 2.2	0.35 ± 0.78	0.89 ± 0.50	0.87 ± 0.48
Modal					
Local	8.4 ± 6.0	36.5 ± 27.2	−6.6 ± 13.6	6.6 ± 9.4	−6.5 ± 8.9
Equilateral	−56 ± 72	74 ± 193	49 ± 123	81 ± 111	28.9 ± 110
Orthogonal	−31 ± 40	−225 ± 119	−75 ± 80	−133 ± 62	−112.4 ± 61
Diff.ps ·1e29	11.4 ± 2.8	(-2.5 ± 2.8)×10^3	−45 ± 64	5.7 ± 7.0	25 ± 5.0
ISW-lensing	0.62 ± 0.40	2.6 ± 2.3	0.92 ± 0.80	0.78 ± 0.60	0.85 ± 0.56

Table 6.10: Results for $f_{\rm NL}$ (assumed independent) of the SMICA half-ring null maps, determined by the KSW, binned and modal estimators.

SMICA *half-ring*	KSW	Binned	Modal
Local	−0.008 ± 0.18	−0.086 ± 0.20	−0.13 ± 0.35
Equilateral	−0.16 ± 2.2	1.3 ± 2.1	0.66 ± 2.0
Orthogonal	−0.035 ± 0.57	0.51 ± 0.57	0.14 ± 0.60
Diff.ps · 1e29 . .	−0.05 ± 0.60	0.03 ± 0.68	0.05 ± 0.65
ISW-lensing . . .	(-0.06 ± 2.0)×10^{-3}	(−2.2 ± 4.7)×10^{-3}	0.009 ± 0.030

Table 6.11: Summary of our $f_{\rm NL}$ analysis of foreground residuals. For realistic lensed FFP6 simulations processed through the SMICA and NILC component separation pipelines, we report: the average $f_{\rm NL}$ with and without foreground residuals added to the maps, the $f_{\rm NL}$ standard deviation in the same two cases, and the standard deviation of the map-by-map $f_{\rm NL}$ difference between the "clean" and "contaminated" sample. The impact of foreground residuals is clearly subdominant when compared to statistical error bars for all shapes. Results reported below have been obtained using the modal estimator (Planck Collaboration XXIV 2013). For the case of SMICA only, the same foreground residuals tests were performed by both KSW and skew-C_ℓ estimators confirming those results.

Modal	SMICA clean	SMICA residual	NILC clean	NILC residual	SMICA residual − clean	NILC residual − clean
Local	7.7 ± 5.9	7.8 ± 5.9	7.7 ± 5.8	7.4 ± 6.0	0.04 ± 1.0	−0.27 ± 1.1
Equilateral	−0.5 ± 77	−8.7 ± 79	−0.6 ± 78	−9.0 ± 79	−8.3 ± 8.2	−8.4 ± 8.3
Orthogonal	−23 ± 41	−25 ± 41	−24 ± 40	−26 ± 41	−2.0 ± 4.7	−2.4 ± 4.8
ISW-lensing	1.00 ± 0.38	1.01 ± 0.38	1.01 ± 0.38	1.02 ± 0.38	0.006 ± 0.052	0.013 ± 0.052

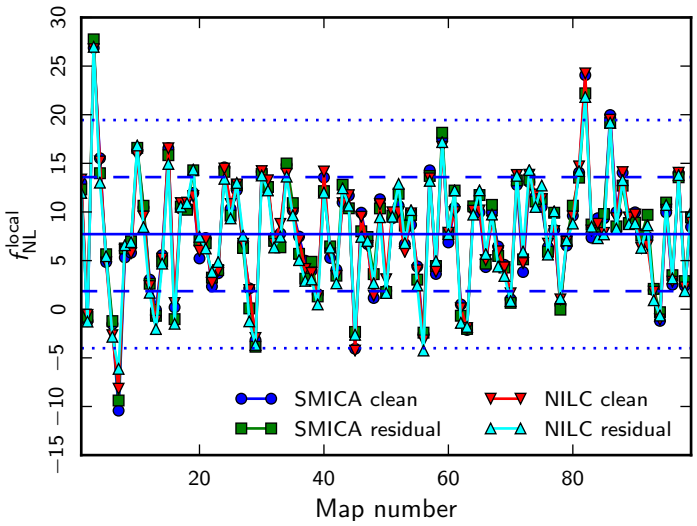

Figure 6.6: The measured $f_{\rm NL}^{\rm local}$ for the first 99 maps in the lensed FFP6 simulation sample used for the foreground studies presented in Sect. 6.2.4. Are showed measurements from `SMICA` and `NILC` processed maps both with and without foreground residuals. The horizontal solid line is the average value of the `SMICA` clean maps, and the dashed and dotted horizontal lines correspond to 1σ and 2σ deviations, respectively. The plot clearly shows the very small impact of including residuals, and the very good consistency between the two component separation pipelines (Planck Collaboration XXIV 2013).

Chapter 7

Conclusions

In this thesis we have derived constraints on primordial NG, using the CMB maps derived from the *Planck* nominal mission data. Using KSW and skew-C_ℓ optimal bispectrum estimators and some other companions – binned, and modal – we obtained consistent values for the primordial local, equilateral, and orthogonal bispectrum amplitudes, quoting as our final result $f_{\rm NL}^{\rm local} = 2.7 \pm 5.8$, $f_{\rm NL}^{\rm equil} = -42 \pm 75$, and $f_{\rm NL}^{\rm ortho} = -25 \pm 39$ (68 % CL statistical). Hence there is no evidence for primordial NG of one of these shapes. We did, however, measure the ISW-lensing bispectrum expected in the ΛCDM scenario (see Planck Collaboration XIX (2013)), as well as a contribution from diffuse point sources, and these contributions are clearly seen in the form of the associated skew-C_ℓ (Planck Collaboration XXIV 2013). These results have been demonstrated to be stable for the four different component separation techniques `SMICA`, `NILC`, `SEVEM`, and `C-R`, showing their robustness against foreground residuals. They have also passed an extensive suite of tests studying the dependence on the maximum multipole number and the mask, consistency checks between frequency channels, and several null tests. In addi-

tion, we have summarized in this thesis an extensive validation campaign for the KSW and skew-C_ℓ optimal bispectrum estimators on Gaussian and non-Gaussian simulations.

These results are also shown to be fully consistent between the different component separation techniques even for the full bispectrum, and contained no significant NG signals of a type not captured by our standard templates at low multipole values. At high multipoles, some indications of unidentified NG signals were found, as also evidenced by the results from the skew-C_ℓ estimator. Further study will be required to ascertain whether these indications are due to foreground residuals, beams, data processing, or a more interesting signal.

The impact of these results on physics of the early Universe, derived from bispectrum constrints on a selection of specific inflationary modelings, had an inpact on general single-field inflationary models (extensions to the standard single-field slow-roll case) as well as multi-field models (Planck Collaboration XXII 2013; Planck Collaboration XXIV 2013). The conclusions of those papers are:

- a lower bound on the speed of sound, $c_{\rm s} \geq 0.02$ (95% CL), from an effective field theory approach to inflationary models which includes models with non-standard kinetic terms, was improved. Strong constraints on other scenarios such as IR DBI, k-inflation, inflationary models involving gauge fields, and warm inflation have been obtained. Within the class of multi-field models, our measurements limit the curvaton decay fraction to $r_{\rm D} \geq 0.15$ (95% CL);

- Ekpyrotic (cyclic) scenarios are shown to be under in tension with the *Planck* data: the so-called "ekpyrotic conversion" mechanism is severely constrained

with our data, and the parameter space of the "kinetic conversion" mechanism is severely limited;

- combining power spectrum data with bounds on $f_{\rm NL}$ measured by *Planck* can constrain many other single-field inflation models with generalized Lagrangians;

- *Planck* data shrink the space of allowed standard inflationary models, preferring potentials with $V'' < 0$;

- models with a parametrized oscillatory feature can improve the χ^2 fit by ~ 10; however, studies based on the Bayesian evidence do not prefer these models.

With these results, the paradigm of standard single-field slow-roll inflation has survived its most stringent tests to-date.

7.1 Future prospect

The work within the *Planck* collaboration is still ongoing. In the 2014 the full mission data will be released and those data will contain polarization maps of the CMB. With this in mind we can the following main future lines:

- error bars will decrease by of about $\sim$ 20-30% because of the increase of the amount of data;

- polarization is an optimal cross-check of our $f_{\rm NL}$ results for three reasons. First, the harmonic space scale of the polarization spectrum is peaked around the Silk-damping tail of the power-spectrum (for temperature it is the first

acoustic peak). Second, using only polarization we can have an error bar for local $f_{\rm NL}$ comparable with *WMAP* (~ 20, see Planck Collaboration (2005)). Third, combining temperature and polarization from the full mission data we can reach an error bar around 4 for local NG (Planck Collaboration 2005);

- polarization foregrounds are at least an order of magnitude higher than the polarization CMB signal. In Yadav et al. (2008a) it is shown, that the $f_{\rm NL}$ estimators can still be optimal using polarization data, with $\ell > 10$. Moreover, since the polarization signal is peaked on small scales but the foregrounds signal are relevant on very large ones, we could hope to be systematics-limited only. This implies that the bispectrum estimators can be even more robust than the power-spectrum estimators, with respect to the polarization foregrounds;

- with the full mission we can possibly detect the ISW-lensing signal at the level of 3σ as it was forecasted in earlier works (Giovi and Baccigalupi 2005; Giovi et al. 2003; Goldberg and Spergel 1999; Verde and Spergel 2002b).

Appendix A

In this appendix we will summarize the KSW and Skew-C_ℓ results for the known separable shapes used in this thesis. In particular, KSW results are already known and can be found in a recent review Komatsu (2010). Instead, the Skew-C_ℓ results for orthogonal, and ISW-lensing are new and are presented here[1]. Since this appendix would be a compact summary, we will leave all the details on previous chapter of this thesis and on the cited references.

[1] Local, equilateral and point-sources results for Skew-C_ℓ can be found in Munshi and Heavens (2010) and Smidt et al. (2009).

A.1 Commonalities

Recalling Section (4.2.1) and (4.2.2), the filtered maps under consideration are, in the primordial shape case:

$$A(\hat{\mathbf{n}}, r) \equiv \sum_{lm} b_l \alpha_l(r)(C^{-1}a)_{lm} Y_{lm}(\hat{\mathbf{n}}), \ , \tag{A.1}$$

$$B(\hat{\mathbf{n}}, r) \equiv \sum_{lm} b_l \beta_l(r)(C^{-1}a)_{lm} Y_{lm}(\hat{\mathbf{n}}), \ , \tag{A.2}$$

$$C(\hat{\mathbf{n}}, r) \equiv \sum_{lm} b_l \gamma_l(r)(C^{-1}a)_{lm} Y_{lm}(\hat{\mathbf{n}}), \ , \tag{A.3}$$

$$D(\hat{\mathbf{n}}, r) \equiv \sum_{lm} b_l \delta_l(r)(C^{-1}a)_{lm} Y_{lm}(\hat{\mathbf{n}}), \ , \tag{A.4}$$

for the non-primordial shapes are used instead:

$$E(\hat{\mathbf{n}}) \equiv \sum_{lm} b_l (C^{-1}a)_{lm} Y_{lm}(\hat{\mathbf{n}}), \ , \tag{A.5}$$

$$P(\hat{\mathbf{n}}) \equiv \sum_{lm} b_l \tilde{C}_\ell^{TT} (C^{-1}a)_{lm} Y_{lm}(\hat{\mathbf{n}}), \ , \tag{A.6}$$

$$Q(\hat{\mathbf{n}}) \equiv \sum_{lm} b_l C_\ell^{T\phi} (C^{-1}a)_{lm} Y_{lm}(\hat{\mathbf{n}}), \ , \tag{A.7}$$

$$\hat{E}(\hat{\mathbf{n}}) \equiv \sum_{lm} -l(l+1) b_l (C^{-1}a)_{lm} Y_{lm}(\hat{\mathbf{n}}), \ , \tag{A.8}$$

$$\hat{P}(\hat{\mathbf{n}}) \equiv \sum_{lm} -l(l+1) b_l \tilde{C}_\ell^{TT} (C^{-1}a)_{lm} Y_{lm}(\hat{\mathbf{n}}), \ , \tag{A.9}$$

$$\hat{Q}(\hat{\mathbf{n}}) \equiv \sum_{lm} -l(l+1) b_l C_\ell^{T\phi} (C^{-1}a)_{lm} Y_{lm}(\hat{\mathbf{n}}), \ . \tag{A.10}$$

The experimental beam is b_l, C^{-1} is the covariance matrix of the signal that here is assumed diagonal and, C_l^{CMB} is the CMB power spectrum, N_l is the noise, then $C_l \equiv C_l^{CMB} b_l^2 + N_l$. P and Q (and E) matrices are connected with the ISW-lensing: $\tilde{C}_\ell^{TT}$ is the lensed temperature power-spectrum and $C_\ell^{T\phi}$ is the temperature-potential

cross power-spectrum.

The other coefficients are defined as

$$\alpha_l(r) = \frac{2}{\pi}\int k^2 dk g_{Tl}(k) j_l(kr), \ , \tag{A.11}$$

$$\beta_l(r) = \frac{2}{\pi}\int k^2 dk P_\Phi(k) g_{Tl}(k) j_l(kr), \ , \tag{A.12}$$

$$\gamma_l(r) = \frac{2}{\pi}\int k^2 dk P_\Phi^{1/3}(k) g_{Tl}(k) j_l(kr), \ , \tag{A.13}$$

$$\delta_l(r) = \frac{2}{\pi}\int k^2 dk P_\Phi(k)^{2/3} g_{Tl}(k) j_l(kr), \ , \tag{A.14}$$

where g_{Tl} is the temperature radiation transfer function, obtained from a modified version of the CAMB code[2], and P_Φ is the primordial gravitational potential power spectrum.

[2] `camb.info`

A.2 KSW

From the maps in previous subsection we can obtain different cubic statistics related to the different bispectrum template, for primordial shapes:

$$\begin{aligned} S_{\text{local}} &= \int r^2 dr \int d^2\hat{\mathbf{n}} \Big[A(\hat{\mathbf{n}}, r) B^2(\hat{\mathbf{n}}, r) \\ &\quad -2B(\hat{\mathbf{n}}, r) \langle A(\hat{\mathbf{n}}, r) B(\hat{\mathbf{n}}, r) \rangle_{MC} - A(\hat{\mathbf{n}}, r) \left\langle B^2(\hat{\mathbf{n}}, r) \right\rangle_{MC} \Big] \ , \end{aligned} \tag{A.15}$$

$$\begin{aligned} S_{\text{equilateral}} &= \int r^2 dr \int d^2\hat{\mathbf{n}} \\ &\quad \Big[-3A(\hat{\mathbf{n}}, r) B^2(\hat{\mathbf{n}}, r) + 6B(\hat{\mathbf{n}}, r) C(\hat{\mathbf{n}}, r) D(\hat{\mathbf{n}}, r) - 2D^3(\hat{\mathbf{n}}, r) \\ &\quad +3A(\hat{\mathbf{n}}, r) \left\langle B^2(\hat{\mathbf{n}}, r) \right\rangle_{MC} + 6B(\hat{\mathbf{n}}, r) \langle A(\hat{\mathbf{n}}, r) B(\hat{\mathbf{n}}, r) \rangle_{MC} \\ &\quad -6B(\hat{\mathbf{n}}, r) \langle C(\hat{\mathbf{n}}, r) D(\hat{\mathbf{n}}, r) \rangle_{MC} - 6D(\hat{\mathbf{n}}, r) \langle B(\hat{\mathbf{n}}, r) C(\hat{\mathbf{n}}, r) \rangle_{MC} \\ &\quad -6C(\hat{\mathbf{n}}, r) \langle D(\hat{\mathbf{n}}, r) B(\hat{\mathbf{n}}, r) \rangle_{MC} + 6D(\hat{\mathbf{n}}, r) \left\langle D^2(\hat{\mathbf{n}}, r) \right\rangle_{MC} \Big] \ , \end{aligned} \tag{A.16}$$

$$\begin{aligned} S_{\text{orthogonal}} &= \int r^2 dr \int d^2\hat{\mathbf{n}} \\ &\quad \Big[-9A(\hat{\mathbf{n}}, r) B^2(\hat{\mathbf{n}}, r) + 18B(\hat{\mathbf{n}}, r) C(\hat{\mathbf{n}}, r) D(\hat{\mathbf{n}}, r) - 8D^3(\hat{\mathbf{n}}, r) \\ &\quad +9A(\hat{\mathbf{n}}, r) \left\langle B^2(\hat{\mathbf{n}}, r) \right\rangle_{MC} + 18B(\hat{\mathbf{n}}, r) \langle A(\hat{\mathbf{n}}, r) B(\hat{\mathbf{n}}, r) \rangle_{MC} \\ &\quad -18B(\hat{\mathbf{n}}, r) \langle C(\hat{\mathbf{n}}, r) D(\hat{\mathbf{n}}, r) \rangle_{MC} - 18D(\hat{\mathbf{n}}, r) \langle B(\hat{\mathbf{n}}, r) C(\hat{\mathbf{n}}, r) \rangle_{MC} \\ &\quad -18C(\hat{\mathbf{n}}, r) \langle D(\hat{\mathbf{n}}, r) B(\hat{\mathbf{n}}, r) \rangle_{MC} + 24D(\hat{\mathbf{n}}, r) \left\langle D^2(\hat{\mathbf{n}}, r) \right\rangle_{MC} \Big] \ ; \end{aligned} \tag{A.17}$$

for non-primordial shapes:

$$S_{\text{point-sources}} = \int d^2\hat{\mathbf{n}}\frac{1}{6}\left[E^3(\hat{\mathbf{n}}) - 3E(\hat{\mathbf{n}})\left\langle E^2(\hat{\mathbf{n}})\right\rangle_{MC}\right] , \tag{A.18}$$

$$\begin{aligned} S_{\text{ISW-lensing}} = \int d^2\hat{\mathbf{n}}\frac{1}{6}\Big[& P(\hat{\mathbf{n}})\hat{E}(\hat{\mathbf{n}})Q(\hat{\mathbf{n}}) - \hat{P}(\hat{\mathbf{n}})E(\hat{\mathbf{n}})Q(\hat{\mathbf{n}}) - P(\hat{\mathbf{n}})E(\hat{\mathbf{n}})\hat{Q}(\hat{\mathbf{n}}) \\ & -P(\hat{\mathbf{n}})\left\langle\hat{E}(\hat{\mathbf{n}})Q(\hat{\mathbf{n}})\right\rangle_{MC} + \hat{P}(\hat{\mathbf{n}})\left\langle E(\hat{\mathbf{n}})Q(\hat{\mathbf{n}})\right\rangle_{MC} + P(\hat{\mathbf{n}})\left\langle E(\hat{\mathbf{n}})\hat{Q}(\hat{\mathbf{n}})\right\rangle_{MC} \\ & +Q(\hat{\mathbf{n}})\left\langle\hat{P}(\hat{\mathbf{n}})E(\hat{\mathbf{n}})\right\rangle_{MC} + \hat{Q}(\hat{\mathbf{n}})\left\langle P(\hat{\mathbf{n}})E(\hat{\mathbf{n}})\right\rangle_{MC} - Q(\hat{\mathbf{n}})\left\langle P(\hat{\mathbf{n}})\hat{E}(\hat{\mathbf{n}})\right\rangle_{MC} \\ & +E(\hat{\mathbf{n}})\left\langle\hat{Q}(\hat{\mathbf{n}})P(\hat{\mathbf{n}})\right\rangle_{MC} - \hat{E}(\hat{\mathbf{n}})\left\langle Q(\hat{\mathbf{n}})P(\hat{\mathbf{n}})\right\rangle_{MC} + E(\hat{\mathbf{n}})\left\langle Q(\hat{\mathbf{n}})\hat{P}(\hat{\mathbf{n}})\right\rangle_{MC}\Big] . \end{aligned} \tag{A.19}$$

Recall that, MC denotes Monte-Carlo averages over CMB simulations including all experimental features considered.

A.3 Skew-C_ℓ

From the maps at the beginning of this chapter we can obtain different skew-C_ℓ statistics related to the different bispectrum template, for primordial shapes:

$$\hat{C}_\ell^{\rm local} = \frac{1}{3}\left(C_\ell^{A,B^2} + 2C_\ell^{B,AB}\right) - C_\ell^{A,\langle B^2\rangle} - 2C_\ell^{B,\langle AB\rangle}\,, \tag{A.20}$$

$$\begin{aligned}\hat{C}_\ell^{\rm equilateral} = & -\left(C_\ell^{A,B^2} + 2C_\ell^{B,AB}\right) + 2\left(C_\ell^{B,CD} + C_\ell^{D,BC} + C_\ell^{C,DB}\right) - 2C_\ell^{D,DD} \\ & +3\left(C_\ell^{A,\langle B^2\rangle} + 2C_\ell^{B,\langle AB\rangle}\right) - 6\left(C_\ell^{B,\langle CD\rangle} + C_\ell^{D,\langle BC\rangle} + C_\ell^{C,\langle DB\rangle}\right) + 6C_\ell^{D,\langle DD\rangle}\,,\end{aligned} \tag{A.21}$$

$$\begin{aligned}\hat{C}_\ell^{\rm orthogonal} = & -3\left(C_\ell^{A,B^2} + 2C_\ell^{B,AB}\right) + 6\left(C_\ell^{B,CD} + C_\ell^{D,BC} + C_\ell^{C,DB}\right) - 8C_\ell^{D,DD} \\ & +9\left(C_\ell^{A,\langle B^2\rangle} + 2C_\ell^{B,\langle AB\rangle}\right) - 18\left(C_\ell^{B,\langle CD\rangle} + C_\ell^{D,\langle BC\rangle} + C_\ell^{C,\langle DB\rangle}\right) + 24C_\ell^{D,\langle DD\rangle}\,,\end{aligned} \tag{A.22}$$

for non-primordial shapes:

$$\hat{C}_\ell^{\rm point-sources} = \frac{1}{6}C_\ell^{E,E^2} - \frac{1}{2}C_\ell^{E,\langle E^2\rangle}\,, \tag{A.23}$$

$$\begin{aligned}\hat{C}_\ell^{\rm ISW-lensing} = & -\frac{1}{6}\left(C_\ell^{\hat{P},EQ} + C_\ell^{P,E\hat{Q}} - C_\ell^{P,\hat{E}Q} + (5\,\text{permutations})\right) \\ & +\frac{1}{2}\left(C_\ell^{\hat{P},\langle EQ\rangle} + C_\ell^{P,\langle E\hat{Q}\rangle} - C_\ell^{P,\langle\hat{E}Q\rangle} + (5\,\text{permutations})\right)\,.\end{aligned} \tag{A.24}$$

Recall that, MC denotes Monte-Carlo averages over CMB simulations including all experimental features considered.

Appendix B

In this appendix, the companion estimators used in the *Planck* $f_{\rm NL}$ data analysis are described.

B.1 Separable Modal Methodology

Primordial bispectra do not need to be manifestly separable (like the local bispectrum), or easily approximated by separable ad hoc templates (equilateral and orthogonal), so the described approach cannot be applied generically (nor to late-time bispectra). However, a highly-efficient generalization consisting considering a complete basis of separable modes describing any late-time bispectrum (see Fergusson and Shellard 2007; Fergusson et al. 2010a). This was applied to *WMAP*-7 data for a wide variety of separable and non-separable bispectrum models (Fergusson et al. 2012)[1]. This can be achieved by expanding the signal-to-noise-weighted bispectrum as

$$\frac{b_{\ell_1\ell_2\ell_3}}{\sqrt{C_{\ell_1}C_{\ell_2}C_{\ell_3}}} = \sum_{i,j,k} \alpha_{ijk} Q_{ijk}(\ell_1,\ell_2,\ell_3)\,, \tag{B.1}$$

[1] See also Planck Collaboration XXIII 2013 and Planck Collaboration XXV 2013.

where the (non-orthogonal) separable modes Q_n are defined by

$$Q_{ijk}(\ell_1, \ell_2, \ell_3) = \frac{1}{6}[q_i(\ell_1)\, q_j(\ell_2)\, q_k(\ell_3) + q_j(\ell_1)\, q_i(\ell_2)\, q_k(\ell_3) + \text{cyclic perms in } i, j, k\,]\,. \tag{B.2}$$

It is more efficient to label the basis as Q_n, with the subscript n representing an ordering of the $\{i, j, k\}$ products (e.g., by distance $i^2 + j^2 + k^2$). The $\bar{q}_i(\ell)$ are any complete basis functions up to a given resolution of interest and they can be augmented with other special functions adapted to target particular bispectra. The modal coefficients in the bispectrum of Eq. (B.1) are given by the inner product of the weighted bispectrum with each mode

$$\alpha_n = \sum_p \gamma^{-1}_{np} \left\langle \frac{b_{\ell_1\ell_2\ell_3}}{\sqrt{C_{\ell_1} C_{\ell_2} C_{\ell_3}}}\,,\; Q_p(\ell_1, \ell_2, \ell_3) \right\rangle \tag{B.3}$$

where the modal transformation matrix is

$$\begin{aligned} \gamma_{np} &= \langle Q_n,\, Q_p \rangle \\ &\equiv \sum_{\ell_1,\ell_2,\ell_3} h^2_{\ell_1\ell_2\ell_3} Q_{ijk}(\ell_1, \ell_2, \ell_3)\, Q_{i'j'k'}(\ell_1, \ell_2, \ell_3)\,. \end{aligned} \tag{B.4}$$

In the following, the specific basis functions $\bar{q}_i(\ell)$ employed include either weighted Legendre-like polynomials or trigonometric functions. These are combined with the Sachs-Wolfe local shape and the separable ISW shape in order to obtain high correlations to all known bispectrum shapes (usually in excess of 99%).

Substituting the separable mode expansion of Eq. (B.1) into the estimator and

exploiting the separability of the Gaunt integral (Eq. (4.4)), yields

$$\mathcal{E} = \frac{1}{N^2} \sum_{n \leftrightarrow prs} \alpha_n \int d^2\hat{\mathbf{n}} \left[\bar{M}_{\{p}(\hat{\mathbf{n}}) \bar{M}_r(\hat{\mathbf{n}}) \bar{M}_{s\}}(\hat{\mathbf{n}}) \right.$$
$$\left. - 6 \left\langle \bar{M}^{\mathrm{G}}_{\{p}(\hat{\mathbf{n}}) \bar{M}^{\mathrm{G}}_r(\hat{\mathbf{n}}) \right\rangle \bar{M}_{s\}}(\hat{\mathbf{n}}) \right] . \tag{B.5}$$

where the $\bar{M}_p(\hat{\mathbf{n}})$ represent versions of the original CMB map filtered with the basis function q_p (and the weights $(\sqrt{C_\ell})^{-1}$), that is,

$$\bar{M}_p(\hat{\mathbf{n}}) = \sum_{\ell m} q_p(\ell) \frac{a_{\ell m}}{\sqrt{C_\ell}} Y_{\ell m}(\hat{\mathbf{n}}) . \tag{B.6}$$

The maps $\bar{M}^{\mathrm{G}}_p(\hat{\mathbf{n}})$ incorporate the same mask and a realistic model of the inhomogeneous instrument noise; a large ensemble of these maps, calculated from Gaussian simulations, is used in the averaged linear term in the estimator of Eq. (B.5), allowing for the subtraction of these important effects. Defining the integral over these convolved product maps as cubic and linear terms respectively,

$$\beta_n{}^{\mathrm{cub}} = \int d^2\hat{\mathbf{n}}\, \bar{M}_{\{p}(\hat{\mathbf{n}}) \bar{M}_r(\hat{\mathbf{n}}) \bar{M}_{s\}}(\hat{\mathbf{n}}) , \tag{B.7}$$

$$\beta_n{}^{\mathrm{lin}} = \int d^2\hat{\mathbf{n}} \left\langle \bar{M}^{\mathrm{G}}_{\{p}(\hat{\mathbf{n}}) \bar{M}^{\mathrm{G}}_r(\hat{\mathbf{n}}) \right\rangle \bar{M}_{s\}}(\hat{\mathbf{n}}) , \tag{B.8}$$

the estimator reduces to a simple sum over the mode coefficients

$$\mathcal{E} = \frac{1}{N^2} \sum_n \alpha_n \bar{\beta}_n , \tag{B.9}$$

where $\bar{\beta}^Q_n \equiv \bar{\beta}^{Q\mathrm{cub}}_n - \bar{\beta}^{Q\mathrm{lin}}_n$. The estimator sum in Eq. (B.9) is now straightforward to evaluate because of separability, since it has been reduced to a product of three

sums over the observational maps (Eq. (B.5)), followed by a single 2D integral over all directions (Eq. (B.7)). The number of operations in evaluating the estimator sum is only $O(\ell^2)$.

For the purposes of testing a wide range of inflationary models, a set of primordial basis functions, $\overline{Q}_{ink}(k_1, k_2, k_3) = \bar{q}_i(k_1)\bar{q}_j(k_2)\bar{q}_k(k_3)$ + perms., can be defined, too, for wavenumbers satisfying the triangle condition (again we will order the $\{i, j, k\}$ with n). This provides a separable expansion for an arbitrary primordial shape function $S(k_1, k_2, k_3) = B(k_1, k_2, k_3)/(k_1k_2k_3)^2$, that is,

$$S(k_1, k_2, k_3) = \sum_n \bar{\alpha}_n \overline{Q}_n(k_1, k_2, k_3)\,. \tag{B.10}$$

Using the same transfer functions as in the KSW integral (4.16), it is possible to efficiently project forward each separable primordial mode $\overline{Q}_n(k_1, k_2, k_3)$ to a corresponding late-time solution $\widetilde{Q}_n(l_1l_2l_3)$ (essentially the projected CMB bispectrum for $\overline{Q}_n(k_1, k_2, k_3)$). By finding the inner product between these projected modes $\widetilde{Q}_n(\ell_1, \ell_2, \ell_3)$ and the CMB basis functions $Q_n(\ell_1, \ell_2, \ell_3)$, the transformation matrix (Fergusson et al. 2010a,b) can be obtained as

$$\Gamma_{np} = \sum_r \bar{\gamma}^{-1}_{np} \langle \widetilde{Q}_r(\ell_1, \ell_2, \ell_3),\ Q(\ell_1, \ell_2, \ell_3) \rangle\,, \tag{B.11}$$

which projects the primordial expansion coefficients α^Q_n to late-time:

$$\alpha_n = \sum_p \Gamma_{np}\bar{\alpha}_p\,. \tag{B.12}$$

Once Γ_{np} is calculated any given primordial bispectrum $B(k_1, k_2, k_3)$ can be efficiently converted into its late-time CMB bispectrum counterpart using Eq. (B.1).

It is also possible to extend the KSW methodology for searching broader range of primordial models beyond local, equilateral and orthogonal cases, after having validated this procedure on these standard shapes.

B.2 Binned Bispectrum

In the binned bispectrum approach (Bucher et al. 2010), the computational gain is achieved by data compression of the observed $\hat{B}$. This is feasible because the bispectrum is a rather smooth function, with features on the scale of the acoustic peaks. In this way one obtains an enormous reduction of the computational resources at the cost of only a tiny increase in variance (typically 1%).

More precisely, the following statistic is considered,

$$T_i(\hat{\mathbf{n}}) = \sum_{\ell \in \Delta_i} \sum_{m=-\ell}^{+\ell} a_{\ell m} Y_{\ell m}(\hat{\mathbf{n}}), \tag{B.13}$$

where the Δ_i are intervals (bins) of multipole values $[\ell_i, \ell_{i+1}-1]$, for $i = 0, \ldots, (N_{\rm bins}-1)$, with $\ell_0 = \ell_{\rm min}$ and $\ell_{N_{\rm bins}} = \ell_{\rm max}+1$, and the other bin boundaries chosen in such a way to minimize the variance of $\hat{f}_{\rm NL}$. The binned bispectrum is then obtained by using T_i instead of T_ℓ in the expression for the sample bispectrum of Eq. (4.9), to obtain:

$$B^{\rm bin}_{i_1 i_2 i_3} = \int T_{i_1}(\hat{\mathbf{n}}) T_{i_2}(\hat{\mathbf{n}}) T_{i_3}(\hat{\mathbf{n}}) d^2\hat{\mathbf{n}}. \tag{B.14}$$

The linear term $B^{\rm lin}$ is binned in an analogous way, and the theoretical bispectrum template $B^{\rm th}$ and variance V are also binned by summing them over the values of ℓ inside the bin. Finally $f_{\rm NL}$ is determined using the binned version of Eq. (4.14), i.e., by replacing all quantities by their binned equivalent and replacing the sum

over ℓ by a sum over bin indices i. An important point is that the binned bispectrum estimator does not mix the observed bispectrum and the theoretical template weights until the very last step of the computation of $\hat{f}_{\rm NL}$ (the final sum over bin indices). Thus, the (binned) bispectrum of the map is also a direct output of the code. Moreover, one can easily study the ℓ-dependence of the results by omitting bins from this final sum.

The full binned bispectrum allows one to explore the bispectral properties of maps independent of a theoretical model. In its simplest implementation, which is used in this thesis, the binned estimator uses top-hat filters in harmonic space, which makes the Gaussian noise independent between different bins; however, slightly overlapping bins could be used to provide better localization properties in pixel space. In this sense the binned estimator is related to the wavelet estimators, which is discussed below.

B.3 Wavelet estimator

Wavelet methods are well-established in the CMB literature and have been applied to virtually all areas of the data analysis pipeline, including map-making and component separation, point source detection, search for anomalies and anisotropies, cross-correlation with large scale structure and the ISW effect, and many others (see for instance Antoine and Vandergheynst 1998, Martínez-González et al. 2002, Cayon et al. 2003, McEwen et al. 2007a, Pietrobon et al. 2006, Starck et al. 2006, McEwen et al. 2007b, Cruz et al. 2007, Faÿ et al. 2008, Feeney et al. 2011, Geller and Mayeli 2009a, Geller and Mayeli 2009b, Starck et al. 2010, Scodeller et al. 2011, Fernandez-Cobos et al. 2012). These methods have the advantage of pos-

sessing localization properties both in real and harmonic space, allowing the effects of masked regions and anisotropic noise to be dealt with efficiently.

In terms of the current discussion, wavelets can be viewed as a way to compress the sample bispectrum vector by a careful binning scheme in the harmonic domain. See also Planck Collaboration XXIII (2013). In particular, the wavelet bispectrum can be rewritten as

$$q_{ijk} = \frac{1}{4\pi}\frac{1}{\sigma_i\sigma_j\sigma_k}\int d^2\hat{\mathbf{n}}\, w(R_i,\hat{\mathbf{n}})w(R_j,\hat{\mathbf{n}})w(R_k,\hat{\mathbf{n}}), \tag{B.15}$$

where

$$w(R;\vec{b}) = \int d^2\hat{\mathbf{n}}\, f(\hat{\mathbf{n}})\Psi(\hat{\mathbf{n}};\vec{b},R) = \sum_{\ell m} a_{\ell m}\omega_\ell(R)Y_{\ell m}(\hat{\mathbf{n}}). \tag{B.16}$$

Here $\vec{b}$ is the position on the sky at which the wavelet coefficient is evaluated and σ is is the dispersion of the wavelet coefficient map $w(R;\vec{b})$ for the scale R. The filters $\omega_\ell(R)$ can be seen as the coefficients of the expansion into spherical harmonic of the Spherical Mexican Hat Wavelet (SMHW) filter

$$\Psi(x,n;R) = \frac{1}{\sqrt{2\pi}}\frac{1}{N(R)}\left[1+\left(\frac{y}{2}\right)^2\right]^2\left[2-\left(\frac{y}{R}\right)^2\right]e^{-y^2/2R^2}. \tag{B.17}$$

Here $N(R) = R\sqrt{1+R^2/2+R^4/4}$ is a normalizing constant and $y = 2\tan(\theta/2)$ represents the distance between x and n, evaluated on the stereographic projection on the tangent plane at n; θ is the corresponding angular distance, evaluated on the spherical surface.

The implementation of the linear-term correction can proceed in analogy with the earlier cases. However, note that, in view of the real-space localization properties of the wavelet filters, the linear term here is smaller than for KSW and related

approaches, although not negligible. Moreover, it can be well-approximated by a term-by-term sample-mean subtraction for the wavelet coefficients, which allows for a further reduction of computational costs. Further details can be found in Curto et al. (2011a,b, 2012); Regan et al. (2013) (see also Donzelli et al. 2012; Lan and Marinucci 2008; Pietrobon et al. 2009, 2010; Rudjord et al. 2009 for related needlet-based procedures).

Bibliography

L. F. Abbott, E. Farhi, and M. B. Wise. Particle production in the new inflationary cosmology. *Physics Letters B*, 117:29–33, November 1982. doi: 10.1016/0370-2693(82)90867-X.

A. Achúcarro, J.-O. Gong, S. Hardeman, G. A. Palma, and S. P. Patil. Features of heavy physics in the CMB power spectrum. *J. Cosmology Astropart. Phys.*, 1: 030, January 2011. doi: 10.1088/1475-7516/2011/01/030.

V. Acquaviva, N. Bartolo, S. Matarrese, and A. Riotto. Gauge-invariant second-order perturbations and non-Gaussianity from inflation. *Nuclear Physics B*, 667:119–148, September 2003. doi: 10.1016/S0550-3213(03)00550-9.

A. Albrecht and P. J. Steinhardt. Cosmology for grand unified theories with radiatively induced symmetry breaking. *Physical Review Letters*, 48:1220–1223, April 1982. doi: 10.1103/PhysRevLett.48.1220.

A. Albrecht, P. J. Steinhardt, M. S. Turner, and F. Wilczek. Reheating an inflationary universe. *Physical Review Letters*, 48:1437–1440, May 1982. doi: 10.1103/PhysRevLett.48.1437.

M. Alishahiha, E. Silverstein, and D. Tong. DBI in the sky: Non-Gaussianity from

inflation with a speed limit. *Phys. Rev. D*, 70(12):123505, December 2004. doi: 10.1103/PhysRevD.70.123505.

J.-P. Antoine and P. Vandergheynst. Wavelets on the n-sphere and related manifolds. *Journal of Mathematical Physics*, 39:3987–4008, August 1998. doi: 10.1063/1.532481.

N. Arkani-Hamed, P. Creminelli, S. Mukohyama, and M. Zaldarriaga. Ghost inflation. *J. Cosmology Astropart. Phys.*, 4:1, April 2004. doi: 10.1088/1475-7516/2004/04/001.

C. Armendariz-Picon, T. Damour, and V. Mukhanov. k-Inflation. *Physics Letters B*, 458:209–218, July 1999. doi: 10.1016/S0370-2693(99)00603-6.

D. Babich. Optimal estimation of non-Gaussianity. *Phys. Rev. D*, 72(4):043003, August 2005. doi: 10.1103/PhysRevD.72.043003.

D. Babich, P. Creminelli, and M. Zaldarriaga. The shape of non-Gaussianities. *J. Cosmology Astropart. Phys.*, 8:9, August 2004. doi: 10.1088/1475-7516/2004/08/009.

J. M. Bardeen. Gauge-invariant cosmological perturbations. *Phys. Rev. D*, 22: 1882–1905, October 1980. doi: 10.1103/PhysRevD.22.1882.

J. M. Bardeen, P. J. Steinhardt, and M. S. Turner. Spontaneous creation of almost scale-free density perturbations in an inflationary universe. *Phys. Rev. D*, 28: 679–693, August 1983. doi: 10.1103/PhysRevD.28.679.

N. Barnaby and J. M. Cline. Non-Gaussian and nonscale-invariant perturbations

from tachyonic preheating in hybrid inflation. *Phys. Rev. D*, 73(10):106012, May 2006. doi: 10.1103/PhysRevD.73.106012.

N. Bartolo, S. Matarrese, and A. Riotto. Non-Gaussianity from inflation. *Phys. Rev. D*, 65(10):103505, May 2002. doi: 10.1103/PhysRevD.65.103505.

N. Bartolo, E. Komatsu, S. Matarrese, and A. Riotto. Non-Gaussianity from inflation: theory and observations. *Phys. Rep.*, 402:103–266, November 2004a. doi: 10.1016/j.physrep.2004.08.022.

N. Bartolo, E. Komatsu, S. Matarrese, and A. Riotto. Non-Gaussianity from inflation: theory and observations. *Phys. Rep.*, 402:103–266, November 2004b. doi: 10.1016/j.physrep.2004.08.022.

N. Bartolo, S. Matarrese, and A. Riotto. Non-Gaussianity in the curvaton scenario. *Phys. Rev. D*, 69(4):043503, February 2004c. doi: 10.1103/PhysRevD.69.043503.

N. Bartolo, S. Matarrese, and A. Riotto. Gauge-Invariant Temperature Anisotropies and Primordial Non-Gaussianity. *Physical Review Letters*, 93(23):231301, December 2004d. doi: 10.1103/PhysRevLett.93.231301.

N. Bartolo, M. Fasiello, S. Matarrese, and A. Riotto. Large non-Gaussianities in the effective field theory approach to single-field inflation: the bispectrum. *J. Cosmology Astropart. Phys.*, 8:8, August 2010. doi: 10.1088/1475-7516/2010/08/008.

C. L. Bennett, A. J. Banday, K. M. Gorski, G. Hinshaw, P. Jackson, P. Keegstra, A. Kogut, G. F. Smoot, D. T. Wilkinson, and E. L. Wright. Four-Year COBE

DMR Cosmic Microwave Background Observations: Maps and Basic Results. *ApJ*, 464:L1, June 1996. doi: 10.1086/310075.

C. L. Bennett, M. Halpern, G. Hinshaw, N. Jarosik, A. Kogut, M. Limon, S. S. Meyer, L. Page, D. N. Spergel, G. S. Tucker, E. Wollack, E. L. Wright, C. Barnes, M. R. Greason, R. S. Hill, E. Komatsu, M. R. Nolta, N. Odegard, H. V. Peiris, L. Verde, and J. L. Weiland. First-Year Wilkinson Microwave Anisotropy Probe (WMAP) Observations: Preliminary Maps and Basic Results. *ApJS*, 148:1–27, September 2003.

C. L. Bennett, D. Larson, J. L. Weiland, N. Jarosik, G. Hinshaw, N. Odegard, K. M. Smith, R. S. Hill, B. Gold, M. Halpern, E. Komatsu, M. R. Nolta, L. Page, D. N. Spergel, E. Wollack, J. Dunkley, A. Kogut, M. Limon, S. S. Meyer, G. S. Tucker, and E. L. Wright. Nine-Year Wilkinson Microwave Anisotropy Probe (WMAP) Observations: Final Maps and Results. *ArXiv e-prints*, December 2012a.

C. L. Bennett, D. Larson, J. L. Weiland, N. Jarosik, G. Hinshaw, N. Odegard, K. M. Smith, R. S. Hill, B. Gold, M. Halpern, E. Komatsu, M. R. Nolta, L. Page, D. N. Spergel, E. Wollack, J. Dunkley, A. Kogut, M. Limon, S. S. Meyer, G. S. Tucker, and E. L. Wright. Nine-Year Wilkinson Microwave Anisotropy Probe (WMAP) Observations: Final Maps and Results. *ArXiv e-prints*, December 2012b.

F. Bernardeau and J.-P. Uzan. Non-Gaussianity in multifield inflation. *Phys. Rev. D*, 66(10):103506, November 2002. doi: 10.1103/PhysRevD.66.103506.

F. Bernardeau, L. Kofman, and J.-P. Uzan. Modulated fluctuations from hybrid inflation. *Phys. Rev. D*, 70(8):083004, October 2004. doi: 10.1103/PhysRevD.70.083004.

M. Bersanelli, N. Mandolesi, R. C. Butler, A. Mennella, F. Villa, B. Aja, E. Artal, E. Artina, C. Baccigalupi, M. Balasini, G. Baldan, A. Banday, P. Bastia, P. Battaglia, T. Bernardino, E. Blackhurst, L. Boschini, C. Burigana, G. Cafagna, B. Cappellini, F. Cavaliere, F. Colombo, G. Crone, F. Cuttaia, O. D'Arcangelo, L. Danese, R. D. Davies, R. J. Davis, L. de Angelis, G. C. de Gasperis, L. de La Fuente, A. de Rosa, G. de Zotti, M. C. Falvella, F. Ferrari, R. Ferretti, L. Figini, S. Fogliani, C. Franceschet, E. Franceschi, T. Gaier, S. Garavaglia, F. Gomez, K. Gorski, A. Gregorio, P. Guzzi, J. M. Herreros, S. R. Hildebrandt, R. Hoyland, N. Hughes, M. Janssen, P. Jukkala, D. Kettle, V. H. Kilpiä, M. Laaninen, P. M. Lapolla, C. R. Lawrence, D. Lawson, J. P. Leahy, R. Leonardi, P. Leutenegger, S. Levin, P. B. Lilje, S. R. Lowe, P. M. Lubin, D. Maino, M. Malaspina, M. Maris, J. Marti-Canales, E. Martinez-Gonzalez, A. Mediavilla, P. Meinhold, M. Miccolis, G. Morgante, P. Natoli, R. Nesti, L. Pagan, C. Paine, B. Partridge, J. P. Pascual, F. Pasian, D. Pearson, M. Pecora, F. Perrotta, P. Platania, M. Pospieszalski, T. Poutanen, M. Prina, R. Rebolo, N. Roddis, J. A. Rubiño-Martin, M. J. Salmon, M. Sandri, M. Seiffert, R. Silvestri, A. Simonetto, P. Sjoman, G. F. Smoot, C. Sozzi, L. Stringhetti, E. Taddei, J. Tauber, L. Terenzi, M. Tomasi, J. Tuovinen, L. Valenziano, J. Varis, N. Vittorio, L. A. Wade, A. Wilkinson, F. Winder, A. Zacchei, and A. Zonca. Planck pre-launch status: Design and description of the Low Frequency Instrument. *A&A*, 520:A4+, September 2010. doi: 10.1051/0004-6361/200912853.

J. R. Bond, A. V. Frolov, Z. Huang, and L. Kofman. Non-Gaussian Curvature Spikes from Chaotic Billiards in Inflation Preheating. *Physical Review Letters*, 103(7):071301, August 2009. doi: 10.1103/PhysRevLett.103.071301.

M. Bucher and Y. Zhu. Non-Gaussian isocurvature perturbations from Goldstone modes generated during inflation. *Phys. Rev. D*, 55:7415–7422, June 1997. doi: 10.1103/PhysRevD.55.7415.

M. Bucher, B. van Tent, and C. S. Carvalho. Detecting bispectral acoustic oscillations from inflation using a new flexible estimator. *MNRAS*, 407:2193–2206, October 2010. doi: 10.1111/j.1365-2966.2010.17089.x.

C. T. Byrnes and K.-Y. Choi. Review of Local Non-Gaussianity from Multifield Inflation. *Advances in Astronomy*, 2010, 2010. doi: 10.1155/2010/724525.

L. Cayon, E. Martínez-González, F. Argueso, A. J. Banday, and K. M. Gorski. COBE-DMR constraints on the non-linear coupling parameter: a wavelet based method. *MNRAS*, 339:1189–1194, March 2003. doi: 10.1046/j.1365-8711.2003.06269.x.

A. Chambers and A. Rajantie. Lattice Calculation of Non-Gaussian Density Perturbations from the Massless Preheating Inflationary Model. *Physical Review Letters*, 100(4):041302, February 2008. doi: 10.1103/PhysRevLett.100.041302.

X. Chen. Running non-Gaussianities in Dirac-Born-Infeld inflation. *Phys. Rev. D*, 72(12):123518, December 2005. doi: 10.1103/PhysRevD.72.123518.

X. Chen. Primordial Non-Gaussianities from Inflation Models. *Advances in Astronomy*, 2010:638979, 2010. doi: 10.1155/2010/638979.

X. Chen, M.-x. Huang, S. Kachru, and G. Shiu. Observational signatures and non-Gaussianities of general single-field inflation. *J. Cosmology Astropart. Phys.*, 1:2, January 2007. doi: 10.1088/1475-7516/2007/01/002.

X. Chen, H. Firouzjahi, M. H. Namjoo, and M. Sasaki. A Single Field Inflation Model with Large Local Non-Gaussianity. *ArXiv e-prints*, January 2013.

C. Cheung, A. L. Fitzpatrick, J. Kaplan, L. Senatore, and P. Creminelli. The effective field theory of inflation. *Journal of High Energy Physics*, 3:14–014, March 2008. doi: 10.1088/1126-6708/2008/03/014.

M. Cicoli, G. Tasinato, I. Zavala, C. P. Burgess, and F. Quevedo. Modulated reheating and large non-gaussianity in string cosmology. *J. Cosmology Astropart. Phys.*, 5:039, May 2012. doi: 10.1088/1475-7516/2012/05/039.

P. Coles and F. Lucchin. *Cosmology. The origin and evolution of cosmic structure*. 1995.

A. Cooray and W. Hu. Imprint of Reionization on the Cosmic Microwave Background Bispectrum. *ApJ*, 534:533–550, May 2000. doi: 10.1086/308799.

P. Creminelli and M. Zaldarriaga. A single-field consistency relation for the three-point function. *J. Cosmology Astropart. Phys.*, 10:6, October 2004. doi: 10.1088/1475-7516/2004/10/006.

P. Creminelli, A. Nicolis, L. Senatore, M. Tegmark, and M. Zaldarriaga. Limits

on non-Gaussianities from WMAP data. *J. Cosmology Astropart. Phys.*, 5:4, May 2006. doi: 10.1088/1475-7516/2006/05/004.

M. Cruz, L. Cayon, E. Martínez-González, P. Vielva, and J. Jin. The Non-Gaussian Cold Spot in the 3 Year Wilkinson Microwave Anisotropy Probe Data. *ApJ*, 655:11–20, January 2007. doi: 10.1086/509703.

A. Curto, E. Martínez-González, and R. B. Barreiro. On the optimality of the spherical Mexican hat wavelet estimator for the primordial non-Gaussianity. *MNRAS*, 412:1038–1046, April 2011a. doi: 10.1111/j.1365-2966.2010.17961.x.

A. Curto, E. Martínez-González, R. B. Barreiro, and M. P. Hobson. Constraints on general primordial non-Gaussianity using wavelets for the Wilkinson Microwave Anisotropy Probe 7-year data. *MNRAS*, 417:488–494, October 2011b. doi: 10.1111/j.1365-2966.2011.19284.x.

A. Curto, E. Martínez-González, and R. B. Barreiro. The effect of the linear term on the wavelet estimator of primordial non-Gaussianity. *MNRAS*, 426:1361–1368, October 2012. doi: 10.1111/j.1365-2966.2012.21805.x.

A. Curto, M. Tucci, J. González-Nuevo, L. Toffolatti, E. Martínez-González, F. Argueso, A. Lapi, and M. Lopez-Caniego. Forecasts on the contamination induced by unresolved point sources in primordial non-Gaussianity beyond Planck. *ArXiv e-prints*, January 2013.

J. Delabrouille, M. Betoule, J.-B. Melin, M.-A. Miville-Deschênes, J. Gonzalez-Nuevo, M. Le Jeune, G. Castex, G. de Zotti, S. Basak, M. Ashdown, J. Aumont,

C. Baccigalupi, A. Banday, J.-P. Bernard, F. R. Bouchet, D. L. Clements, A. da Silva, C. Dickinson, F. Dodu, K. Dolag, F. Elsner, L. Fauvet, G. Faÿ, G. Giardino, S. Leach, J. Lesgourgues, M. Liguori, J. F. Macias-Perez, M. Massardi, S. Matarrese, P. Mazzotta, L. Montier, S. Mottet, R. Paladini, B. Partridge, R. Piffaretti, G. Prezeau, S. Prunet, S. Ricciardi, M. Roman, B. Schaefer, and L. Toffolatti. The pre-launch Planck Sky Model: a model of sky emission at submillimetre to centimetre wavelengths. *ArXiv e-prints*, July 2012.

S. Dodelson. *Modern cosmology*. 2003.

A. D. Dolgov and A. D. Linde. Baryon asymmetry in the inflationary universe. *Physics Letters B*, 116:329–334, October 1982. doi: 10.1016/0370-2693(82)90292-1.

S. Donzelli, F. K. Hansen, M. Liguori, D. Marinucci, and S. Matarrese. On the Linear Term Correction for Needlet/Wavelet Non-Gaussianity Estimators. *ApJ*, 755:19, August 2012. doi: 10.1088/0004-637X/755/1/19.

G. Dvali, A. Gruzinov, and M. Zaldarriaga. New mechanism for generating density perturbations from inflation. *Phys. Rev. D*, 69(2):023505, January 2004a. doi: 10.1103/PhysRevD.69.023505.

G. Dvali, A. Gruzinov, and M. Zaldarriaga. Cosmological perturbations from inhomogeneous reheating, freeze-out, and mass domination. *Phys. Rev. D*, 69(8):083505, April 2004b. doi: 10.1103/PhysRevD.69.083505.

F. Elsner and B. D. Wandelt. Efficient Wiener filtering without preconditioning. *A&A*, 549:A111, January 2013. doi: 10.1051/0004-6361/201220586. URL http://adsabs.harvard.edu/abs/2013A%26A...549A.111E.

K. Enqvist and M. S. Sloth. Adiabatic CMB perturbations in pre-Big-Bang string cosmology. *Nuclear Physics B*, 626:395–409, April 2002. doi: 10.1016/S0550-3213(02)00043-3.

K. Enqvist, A. Jokinen, A. Mazumdar, T. Multamäki, and A. Väihkönen. Non-Gaussianity from preheating. *Physical Review Letters*, 94(16):161301, April 2005. doi: 10.1103/PhysRevLett.94.161301.

T. Falk, R. Rangarajan, and M. Srednicki. The angular dependence of the three-point correlation function of the cosmic microwave background radiation as predicted by inflationary cosmologies. *ApJ*, 403:L1–L3, January 1993. doi: 10.1086/186707.

G. Faÿ, F. Guilloux, M. Betoule, J.-F. Cardoso, J. Delabrouille, and M. Le Jeune. CMB power spectrum estimation using wavelets. *Phys. Rev. D*, 78(8):083013, October 2008. doi: 10.1103/PhysRevD.78.083013.

S. M. Feeney, M. C. Johnson, D. J. Mortlock, and H. V. Peiris. First observational tests of eternal inflation: Analysis methods and WMAP 7-year results. *Phys. Rev. D*, 84(4):043507, August 2011. doi: 10.1103/PhysRevD.84.043507.

J. R. Fergusson and E. P. S. Shellard. Primordial non-Gaussianity and the CMB bispectrum. *Phys. Rev. D*, 76(8):083523, October 2007. doi: 10.1103/PhysRevD.76.083523.

J. R. Fergusson, M. Liguori, and E. P. S. Shellard. General CMB and primordial bispectrum estimation: Mode expansion, map making, and measures of F_{NL}. *Phys. Rev. D*, 82(2):023502, July 2010a. doi: 10.1103/PhysRevD.82.023502.

J. R. Fergusson, D. M. Regan, and E. P. S. Shellard. Optimal Trispectrum Estimators and WMAP Constraints. *ArXiv e-prints*, December 2010b.

J. R. Fergusson, M. Liguori, and E. P. S. Shellard. The CMB bispectrum. *J. Cosmology Astropart. Phys.*, 12:032, December 2012. doi: 10.1088/1475-7516/2012/12/032.

R. Fernandez-Cobos, P. Vielva, R. B. Barreiro, and E. Martínez-González. Multiresolution internal template cleaning: an application to the Wilkinson Microwave Anisotropy Probe 7-yr polarization data. *MNRAS*, 420:2162–2169, March 2012. doi: 10.1111/j.1365-2966.2011.20182.x.

A. A. Fraisse, P. A. R. Ade, M. Amiri, S. J. Benton, J. J. Bock, J. R. Bond, J. A. Bonetti, S. Bryan, B. Burger, H. C. Chiang, C. N. Clark, C. R. Contaldi, B. P. Crill, G. Davis, O. Doré, M. Farhang, J. P. Filippini, L. M. Fissel, N. N. Gandilo, S. Golwala, J. E. Gudmundsson, M. Hasselfield, G. Hilton, W. Holmes, V. V. Hristov, K. Irwin, W. C. Jones, C. L. Kuo, C. J. MacTavish, P. V. Mason, T. E. Montroy, T. A. Morford, C. B. Netterfield, D. T. O'Dea, A. S. Rahlin, C. Reintsema, J. E. Ruhl, M. C. Runyan, M. A. Schenker, J. A. Shariff, J. D. Soler, A. Trangsrud, C. Tucker, R. S. Tucker, A. D. Turner, and D. Wiebe. SPIDER: Probing the Early Universe with a Suborbital Polarimeter. *ArXiv e-prints*, June 2011.

A. Gangui and J. Martin. Best unbiased estimators for the three-point correlators of the cosmic microwave background radiation. *Phys. Rev. D*, 62(10):103004, November 2000. doi: 10.1103/PhysRevD.62.103004.

A. Gangui, F. Lucchin, S. Matarrese, and S. Mollerach. The three-point correla-

tion function of the cosmic microwave background in inflationary models. *ApJ*, 430:447–457, August 1994. doi: 10.1086/174421.

Daryl Geller and Azita Mayeli. Continuous wavelets on compact manifolds. *Math. Z.*, 262(4):895–927, 2009a. ISSN 0025-5874. doi: 10.1007/s00209-008-0405-7. URL http://dx.doi.org/10.1007/s00209-008-0405-7.

Daryl Geller and Azita Mayeli. Nearly tight frames and space-frequency analysis on compact manifolds. *Math. Z.*, 263(2):235–264, 2009b. ISSN 0025-5874. doi: 10.1007/s00209-008-0406-6. URL http://dx.doi.org/10.1007/s00209-008-0406-6.

F. Giovi and C. Baccigalupi. Dark Energy and CMB Bispectrum. In Y. Mellier and G. Meylan, editors, *Gravitational Lensing Impact on Cosmology*, volume 225 of *IAU Symposium*, pages 117–122, June 2005. doi: 10.1017/S1743921305001882.

F. Giovi, C. Baccigalupi, and F. Perrotta. Constraining the dark energy dynamics with the cosmic microwave background bispectrum. *Phys. Rev. D*, 68(12): 123002, December 2003. doi: 10.1103/PhysRevD.68.123002.

F. Giovi, C. Baccigalupi, and F. Perrotta. Cosmic microwave background constraints on dark energy dynamics: Analysis beyond the power spectrum. *Phys. Rev. D*, 71(10):103009, May 2005. doi: 10.1103/PhysRevD.71.103009.

D. M. Goldberg and D. N. Spergel. Microwave background bispectrum. II. A probe of the low redshift universe. *Phys. Rev. D*, 59(10):103002, May 1999. doi: 10.1103/PhysRevD.59.103002.

J. González-Nuevo, L. Toffolatti, and F. Argüeso. Predictions of the Angular Power Spectrum of Clustered Extragalactic Point Sources at Cosmic Microwave Background Frequencies from Flat and All-Sky Two-dimensional Simulations. *ApJ*, 621:1–14, March 2005. doi: 10.1086/427425.

J. González-Nuevo, F. Argüeso, M. López-Caniego, L. Toffolatti, J. L. Sanz, P. Vielva, and D. Herranz. The Mexican hat wavelet family: application to point-source detection in cosmic microwave background maps. *MNRAS*, 369: 1603–1610, July 2006. doi: 10.1111/j.1365-2966.2006.10442.x.

K. M. Gorski, E. Hivon, A. J. Banday, B. D. Wandelt, F. K. Hansen, M. Reinecke, and M. Bartelmann. HEALPix: A Framework for High-Resolution Discretization and Fast Analysis of Data Distributed on the Sphere. *Astrophys.J.*, 622: 759, 2005.

A. H. Guth. Inflationary universe: A possible solution to the horizon and flatness problems. *Phys. Rev. D*, 23:347–356, January 1981. doi: 10.1103/PhysRevD.23.347.

D. Hanson, K. M. Smith, A. Challinor, and M. Liguori. CMB lensing and primordial non-Gaussianity. *Phys. Rev. D*, 80(8):083004, October 2009. doi: 10.1103/PhysRevD.80.083004.

A. F. Heavens. Estimating non-Gaussianity in the microwave background. *MNRAS*, 299:805–808, September 1998. doi: 10.1046/j.1365-8711.1998.01820.x.

G. Hinshaw, D. Larson, E. Komatsu, D. N. Spergel, C. L. Bennett, J. Dunkley, M. R. Nolta, M. Halpern, R. S. Hill, N. Odegard, L. Page, K. M. Smith, J. L.

Weiland, B. Gold, N. Jarosik, A. Kogut, M. Limon, S. S. Meyer, G. S. Tucker, E. Wollack, and E. L. Wright. Nine-Year Wilkinson Microwave Anisotropy Probe (WMAP) Observations: Cosmological Parameter Results. *ArXiv e-prints*, December 2012a.

G. Hinshaw, D. Larson, E. Komatsu, D. N. Spergel, C. L. Bennett, J. Dunkley, M. R. Nolta, M. Halpern, R. S. Hill, N. Odegard, L. Page, K. M. Smith, J. L. Weiland, B. Gold, N. Jarosik, A. Kogut, M. Limon, S. S. Meyer, G. S. Tucker, E. Wollack, and E. L. Wright. Nine-Year Wilkinson Microwave Anisotropy Probe (WMAP) Observations: Cosmological Parameter Results. *ArXiv e-prints*, December 2012b.

H. M. Hodges, G. R. Blumenthal, L. A. Kofman, and J. R. Primack. Nonstandard primordial fluctuations from a polynomial inflation potential. *Nuclear Physics B*, 335:197–220, April 1990. doi: 10.1016/0550-3213(90)90177-F.

V. Junk and E. Komatsu. Cosmic microwave background bispectrum from the lensing-Rees-Sciama correlation reexamined: Effects of nonlinear matter clustering. *Phys. Rev. D*, 85(12):123524, June 2012. doi: 10.1103/PhysRevD.85.123524.

E. Keihänen, R. Keskitalo, H. Kurki-Suonio, T. Poutanen, and A.-S. Sirviö. Making cosmic microwave background temperature and polarization maps with MADAM. *A&A*, 510:A57+, February 2010. doi: 10.1051/0004-6361/200912813.

R. Keisler, C. L. Reichardt, K. A. Aird, B. A. Benson, L. E. Bleem, J. E. Carlstrom, C. L. Chang, H. M. Cho, T. M. Crawford, A. T. Crites, T. de Haan,

M. A. Dobbs, J. Dudley, E. M. George, N. W. Halverson, G. P. Holder, W. L. Holzapfel, S. Hoover, Z. Hou, J. D. Hrubes, M. Joy, L. Knox, A. T. Lee, E. M. Leitch, M. Lueker, D. Luong-Van, J. J. McMahon, J. Mehl, S. S. Meyer, M. Millea, J. J. Mohr, T. E. Montroy, T. Natoli, S. Padin, T. Plagge, C. Pryke, J. E. Ruhl, K. K. Schaffer, L. Shaw, E. Shirokoff, H. G. Spieler, Z. Staniszewski, A. A. Stark, K. Story, A. van Engelen, K. Vanderlinde, J. D. Vieira, R. Williamson, and O. Zahn. A Measurement of the Damping Tail of the Cosmic Microwave Background Power Spectrum with the South Pole Telescope. *ApJ*, 743:28, December 2011. doi: 10.1088/0004-637X/743/1/28.

T. Kelsall, J. L. Weiland, B. A. Franz, W. T. Reach, R. G. Arendt, E. Dwek, H. T. Freudenreich, M. G. Hauser, S. H. Moseley, N. P. Odegard, R. F. Silverberg, and E. L. Wright. The COBE Diffuse Infrared Background Experiment Search for the Cosmic Infrared Background. II. Model of the Interplanetary Dust Cloud. *ApJ*, 508:44–73, November 1998. doi: 10.1086/306380.

J. Kim, A. Rotti, and E. Komatsu. Removing the ISW-lensing bias from the local-form primordial non-Gaussianity estimation. *ArXiv e-prints*, February 2013.

H. Kodama and M. Sasaki. Cosmological Perturbation Theory. *Progress of Theoretical Physics Supplement*, 78:1, 1984. doi: 10.1143/PTPS.78.1.

L. Kofman. Probing String Theory with Modulated Cosmological Fluctuations. *ArXiv Astrophysics e-prints*, March 2003.

L. Kofman, G. R. Blumenthal, H. Hodges, and J. R. Primack. Generation of Non-Flat and Non-Gaussian Perturbations from Inflation. In D. W. Latham and L. A. N. da Costa, editors, *Large-scale Structures and Peculiar Motions in the*

Universe, volume 15 of *Astronomical Society of the Pacific Conference Series*, page 339, 1991.

E. W. Kolb, A. Riotto, and A. Vallinotto. Non-Gaussianity from broken symmetries. *Phys. Rev. D*, 73(2):023522, January 2006. doi: 10.1103/PhysRevD.73.023522.

E. Komatsu. The Pursuit of Non-Gaussian Fluctuations in the Cosmic Microwave Background. *ArXiv Astrophysics e-prints*, June 2002.

E. Komatsu. Hunting for primordial non-Gaussianity in the cosmic microwave background. *Classical and Quantum Gravity*, 27(12):124010, June 2010. doi: 10.1088/0264-9381/27/12/124010.

E. Komatsu and D. N. Spergel. Acoustic signatures in the primary microwave background bispectrum. *Phys. Rev. D*, 63(6):063002, March 2001. doi: 10.1103/PhysRevD.63.063002.

E. Komatsu, A. Kogut, M. R. Nolta, C. L. Bennett, M. Halpern, G. Hinshaw, N. Jarosik, M. Limon, S. S. Meyer, L. Page, D. N. Spergel, G. S. Tucker, L. Verde, E. Wollack, and E. L. Wright. First-Year Wilkinson Microwave Anisotropy Probe (WMAP) Observations: Tests of Gaussianity. *ApJS*, 148:119–134, September 2003. doi: 10.1086/377220.

E. Komatsu, D. N. Spergel, and B. D. Wandelt. Measuring Primordial Non-Gaussianity in the Cosmic Microwave Background. *ApJ*, 634:14–19, November 2005. doi: 10.1086/491724.

E. Komatsu, J. Dunkley, M. R. Nolta, C. L. Bennett, B. Gold, G. Hinshaw,

N. Jarosik, D. Larson, M. Limon, L. Page, D. N. Spergel, M. Halpern, R. S. Hill, A. Kogut, S. S. Meyer, G. S. Tucker, J. L. Weiland, E. Wollack, and E. L. Wright. Five-Year Wilkinson Microwave Anisotropy Probe Observations: Cosmological Interpretation. *ApJS*, 180:330–376, February 2009. doi: 10.1088/0067-0049/180/2/330.

E. Komatsu, K. M. Smith, J. Dunkley, C. L. Bennett, B. Gold, G. Hinshaw, N. Jarosik, D. Larson, M. R. Nolta, L. Page, D. N. Spergel, M. Halpern, R. S. Hill, A. Kogut, M. Limon, S. S. Meyer, N. Odegard, G. S. Tucker, J. L. Weiland, E. Wollack, and E. L. Wright. Seven-year Wilkinson Microwave Anisotropy Probe (WMAP) Observations: Cosmological Interpretation. *ApJS*, 192:18, February 2011. doi: 10.1088/0067-0049/192/2/18.

A. Kosowsky. The Atacama Cosmology Telescope. *New A Rev.*, 47:939–943, December 2003. doi: 10.1016/j.newar.2003.09.003.

F. Lacasa and N. Aghanim. Optimal estimator for the amplitude of the bispectrum from IR sources. *ArXiv e-prints*, November 2012.

F. Lacasa, N. Aghanim, M. Kunz, and M. Frommert. *MNRAS*, 421:1982–1995, April 2012. doi: 10.1111/j.1365-2966.2012.20415.x.

J.-M. Lamarre, J.-L. Puget, P. A. R. Ade, F. Bouchet, G. Guyot, A. E. Lange, F. Pajot, A. Arondel, K. Benabed, J.-L. Beney, A. Benoît, J.-P. Bernard, R. Bhatia, Y. Blanc, J. J. Bock, E. Bréelle, T. W. Bradshaw, P. Camus, A. Catalano, J. Charra, M. Charra, S. E. Church, F. Couchot, A. Coulais, B. P. Crill, M. R. Crook, K. Dassas, P. de Bernardis, J. Delabrouille, P. de Marcillac, J.-M. Delouis, F.-X. Désert, C. Dumesnil, X. Dupac, G. Efstathiou, P. Eng, C. Evesque,

J.-J. Fourmond, K. Ganga, M. Giard, R. Gispert, L. Guglielmi, J. Haissinski, S. Henrot-Versillé, E. Hivon, W. A. Holmes, W. C. Jones, T. C. Koch, H. Lagardère, P. Lami, J. Landé, B. Leriche, C. Leroy, Y. Longval, J. F. Macías-Pérez, T. Maciaszek, B. Maffei, B. Mansoux, C. Marty, S. Masi, C. Mercier, M.-A. Miville-Deschênes, A. Moneti, L. Montier, J. A. Murphy, J. Narbonne, M. Nexon, C. G. Paine, J. Pahn, O. Perdereau, F. Piacentini, M. Piat, S. Plaszczynski, E. Pointecouteau, R. Pons, N. Ponthieu, S. Prunet, D. Rambaud, G. Recouvreur, C. Renault, I. Ristorcelli, C. Rosset, D. Santos, G. Savini, G. Serra, P. Stassi, R. V. Sudiwala, J.-F. Sygnet, J. A. Tauber, J.-P. Torre, M. Tristram, L. Vibert, A. Woodcraft, V. Yurchenko, and D. Yvon. Planck prelaunch status: The HFI instrument, from specification to actual performance. *A&A*, 520:A9+, September 2010. doi: 10.1051/0004-6361/200912975.

X. Lan and D. Marinucci. The needlets bispectrum. *Electronic Journal of Statistics*, 2:332–367, 2008. doi: 10.1214/08-EJS197.

A. Lewis. The full squeezed CMB bispectrum from inflation. *J. Cosmology Astropart. Phys.*, 6:023, June 2012. doi: 10.1088/1475-7516/2012/06/023.

A. Lewis, A. Challinor, and D. Hanson. The shape of the CMB lensing bispectrum. *J. Cosmology Astropart. Phys.*, 3:18, March 2011. doi: 10.1088/1475-7516/2011/03/018.

A. R. Liddle and D. H. Lyth. *Cosmological Inflation and Large-Scale Structure*. June 2000.

M. Liguori, E. Sefusatti, J. R. Fergusson, and E. P. S. Shellard. Primordial Non-Gaussianity and Bispectrum Measurements in the Cosmic Microwave Back-

ground and Large-Scale Structure. *Advances in Astronomy*, 2010:980523, 2010. doi: 10.1155/2010/980523.

A. Linde. Extended chaotic inflation and spatial variations of the gravitational constant. *Physics Letters B*, 238:160–165, April 1990. doi: 10.1016/0370-2693(90)91713-L.

A. Linde and V. Mukhanov. Non-Gaussian isocurvature perturbations from inflation. *Phys. Rev. D*, 56:535, July 1997. doi: 10.1103/PhysRevD.56.R535.

A. D. Linde. A new inflationary universe scenario: A possible solution of the horizon, flatness, homogeneity, isotropy and primordial monopole problems. *Physics Letters B*, 108:389–393, February 1982. doi: 10.1016/0370-2693(82)91219-9.

A. D. Linde. Chaotic inflation. *Physics Letters B*, 129:177–181, September 1983. doi: 10.1016/0370-2693(83)90837-7.

M. López-Caniego, D. Herranz, J. González-Nuevo, J. L. Sanz, R. B. Barreiro, P. Vielva, F. Argüeso, and L. Toffolatti. Comparison of filters for the detection of point sources in Planck simulations. *MNRAS*, 370:2047–2063, August 2006. doi: 10.1111/j.1365-2966.2006.10639.x.

D. H. Lyth. Generating the curvature perturbation at the end of inflation. *J. Cosmology Astropart. Phys.*, 11:6, December 2005. doi: 10.1088/1475-7516/2005/11/006.

D. H. Lyth and A. Riotto. Generating the Curvature Perturbation at the End of

Inflation in String Theory. *Physical Review Letters*, 97(12):121301, September 2006. doi: 10.1103/PhysRevLett.97.121301.

D. H. Lyth and Y. Rodriguez. Inflationary Prediction for Primordial Non-Gaussianity. *Physical Review Letters*, 95(12):121302, September 2005. doi: 10.1103/PhysRevLett.95.121302.

D. H. Lyth and D. Wands. Generating the curvature perturbation without an inflaton. *Physics Letters B*, 524:5–14, January 2002. doi: 10.1016/S0370-2693(01)01366-1.

D. H. Lyth, C. Ungarelli, and D. Wands. Primordial density perturbation in the curvaton scenario. *Phys. Rev. D*, 67(2):023503, January 2003. doi: 10.1103/PhysRevD.67.023503.

J. Maldacena. Non-gaussian features of primordial fluctuations in single field inflationary models. *Journal of High Energy Physics*, 5:13, May 2003. doi: 10.1088/1126-6708/2003/05/013.

A. Mangilli and L. Verde. Non-Gaussianity and the CMB bispectrum: Confusion between primordial and lensing-Rees-Sciama contribution? *Phys. Rev. D*, 80(12):123007, December 2009. doi: 10.1103/PhysRevD.80.123007.

A. Mangilli, B. Wandelt, F. Elsner, and M. Liguori. Optimal bispectrum estimator and simulations of the the CMB Lensing-ISW non-Gaussian signal. *ArXiv e-prints*, March 2013.

E. Martínez-González, J. E. Gallegos, F. Argüeso, L. Cayon, and J. L. Sanz. The performance of spherical wavelets to detect non-Gaussianity in the cos-

mic microwave background sky. *MNRAS*, 336:22–32, October 2002. doi: 10.1046/j.1365-8711.2002.05648.x.

J. D. McEwen, P. Vielva, M. P. Hobson, E. Martínez-González, and A. N. Lasenby. Detection of the integrated Sachs-Wolfe effect and corresponding dark energy constraints made with directional spherical wavelets. *MNRAS*, 376: 1211–1226, April 2007a. doi: 10.1111/j.1365-2966.2007.11505.x.

J. D. McEwen, P. Vielva, Y. Wiaux, R. B. Barreiro, L. Cayon, M. P. Hobson, A. N. Lasenby, E. Martínez-González, and J. L. Sanz. Cosmological applications of a wavelet analysis on the sphere. *Journal of Fourier Analysis and Applications*, 13:495–510, August 2007b. doi: 10.1007/s00041-006-6918-8.

A. Mennella, R. C. Butler, A. Curto, F. Cuttaia, R. J. Davis, J. Dick, M. Frailis, S. Galeotta, A. Gregorio, H. Kurki-Suonio, C. R. Lawrence, S. Leach, J. P. Leahy, S. Lowe, D. Maino, N. Mandolesi, M. Maris, E. Martínez-González, P. R. Meinhold, G. Morgante, D. Pearson, F. Perrotta, G. Polenta, T. Poutanen, M. Sandri, M. D. Seiffert, A.-S. Suur-Uski, D. Tavagnacco, L. Terenzi, M. Tomasi, J. Valiviita, F. Villa, R. Watson, A. Wilkinson, A. Zacchei, A. Zonca, B. Aja, E. Artal, C. Baccigalupi, A. J. Banday, R. B. Barreiro, J. G. Bartlett, N. Bartolo, P. Battaglia, K. Bennett, A. Bonaldi, L. Bonavera, J. Borrill, F. R. Bouchet, C. Burigana, P. Cabella, B. Cappellini, X. Chen, L. Colombo, M. Cruz, L. Danese, O. D'Arcangelo, R. D. Davies, G. de Gasperis, A. de Rosa, G. de Zotti, C. Dickinson, J. M. Diego, S. Donzelli, G. Efstathiou, T. A. Enßlin, H. K. Eriksen, M. C. Falvella, F. Finelli, S. Foley, C. Franceschet, E. Franceschi, T. C. Gaier, R. T. Génova-Santos, D. George, F. Gómez, J. González-Nuevo, K. M. Górski, A. Gruppuso, F. K. Hansen, D. Herranz, J. M. Herreros,

R. J. Hoyland, N. Hughes, J. Jewell, P. Jukkala, M. Juvela, P. Kangaslahti, E. Keihänen, R. Keskitalo, V.-H. Kilpia, T. S. Kisner, J. Knoche, L. Knox, M. Laaninen, A. Lähteenmäki, J.-M. Lamarre, R. Leonardi, J. León-Tavares, P. Leutenegger, P. B. Lilje, M. López-Caniego, P. M. Lubin, M. Malaspina, D. Marinucci, M. Massardi, S. Matarrese, F. Matthai, A. Melchiorri, L. Mendes, M. Miccolis, M. Migliaccio, S. Mitra, A. Moss, P. Natoli, R. Nesti, H. U. Nørgaard-Nielsen, L. Pagano, R. Paladini, D. Paoletti, B. Partridge, F. Pasian, V. Pettorino, D. Pietrobon, M. Pospieszalski, G. Prézeau, M. Prina, P. Procopio, J.-L. Puget, C. Quercellini, J. P. Rachen, R. Rebolo, M. Reinecke, S. Ricciardi, G. Robbers, G. Rocha, N. Roddis, J. A. Rubino-Martín, M. Savelainen, D. Scott, R. Silvestri, A. Simonetto, P. Sjoman, G. F. Smoot, C. Sozzi, L. Stringhetti, J. A. Tauber, G. Tofani, L. Toffolatti, J. Tuovinen, M. Türler, G. Umana, L. Valenziano, J. Varis, P. Vielva, N. Vittorio, L. A. Wade, C. Watson, S. D. M. White, and F. Winder. Planck early results. III. First assessment of the Low Frequency Instrument in-flight performance. *A&A*, 536:A3, 2011.

S. Mitra, G. Rocha, K. M. Górski, K. M. Huffenberger, H. K. Eriksen, M. A. J. Ashdown, and C. R. Lawrence. Fast Pixel Space Convolution for Cosmic Microwave Background Surveys with Asymmetric Beams and Complex Scan Strategies: FEBeCoP. *ApJS*, 193:5–+, March 2011. doi: 10.1088/0067-0049/193/1/5.

S. Mollerach. Isocurvature baryon perturbations and inflation. *Phys. Rev. D*, 42: 313–325, July 1990. doi: 10.1103/PhysRevD.42.313.

T. Moroi and T. Takahashi. Effects of cosmological moduli fields on cosmic mi-

crowave background. *Physics Letters B*, 522:215–221, December 2001. doi: 10.1016/S0370-2693(01)01295-3.

D. Munshi and A. Heavens. A new approach to probing primordial non-Gaussianity. *MNRAS*, 401:2406–2418, February 2010. doi: 10.1111/j.1365-2966.2009.15820.x.

P. J. E. Peebles. *The large-scale structure of the universe*. 1980.

P. J. E. Peebles. An Isocurvature Model for Early Galaxy Assembly. *ApJ*, 483: L1, July 1997. doi: 10.1086/310738.

A. A. Penzias and R. W. Wilson. A Measurement of Excess Antenna Temperature at 4080 Mc/s. *ApJ*, 142:419–421, July 1965. doi: 10.1086/148307.

D. Pietrobon, A. Balbi, and D. Marinucci. Integrated Sachs-Wolfe effect from the cross correlation of WMAP 3year and the NRAO VLA sky survey data: New results and constraints on dark energy. *Phys. Rev. D*, 74(4):043524, August 2006. doi: 10.1103/PhysRevD.74.043524.

D. Pietrobon, P. Cabella, A. Balbi, G. de Gasperis, and N. Vittorio. Constraints on primordial non-Gaussianity from a needlet analysis of the WMAP-5 data. *MNRAS*, 396:1682–1688, July 2009. doi: 10.1111/j.1365-2966.2009.14847.x.

D. Pietrobon, P. Cabella, A. Balbi, R. Crittenden, G. de Gasperis, and N. Vittorio. Needlet bispectrum asymmetries in the WMAP 5-year data. *MNRAS*, 402:L34–L38, February 2010. doi: 10.1111/j.1745-3933.2009.00794.x.

Planck Collaboration. The Scientific Programme of Planck. *ESA publication ESA-SCI(2005)/01*, 2005.

Planck Collaboration ES. *The Explanatory Supplement to the Planck 2013 results*. ESA, 2013.

Planck Collaboration I. Planck early results. I. The Planck mission. *A&A*, 536: A1, 2011.

Planck Collaboration I. *Planck* 2013 results: Overview of Planck Products and Scientific Results (p01). *Submitted to A&A*, 2013.

Planck Collaboration VI. *Planck* 2013 results: High Frequency Instrument Data Processing (p03). *Submitted to A&A*, 2013.

Planck Collaboration VII. *Planck* 2013 results: HFI time response and beams (p03c). *Submitted to A&A*, 2013.

Planck Collaboration VIII. Planck early results. VIII. The all-sky early Sunyaev-Zeldovich cluster sample. *A&A*, 536:A8, 2011.

Planck Collaboration VIII. *Planck* 2013 results: HFI calibration and Map-making (p03f). *Submitted to A&A*, 2013.

Planck Collaboration XII. *Planck* 2013 results: Component separation (p06). *Submitted to A&A*, 2013.

Planck Collaboration XIII. *Planck* 2013 results: Galactic CO emission as seen by Planck (p03a). *Submitted to A&A*, 2013.

Planck Collaboration XIV. *Planck* 2013 results: Zodiacal emission (pip88). *Submitted to A&A*, 2013.

Planck Collaboration XIX. *Planck* 2013 results: The integrated Sachs-Wolfe effect (p14). *Submitted to A&A*, 2013.

Planck Collaboration XV. *Planck* 2013 results: CMB power spectra and likelihood (p08). *Submitted to A&A*, 2013.

Planck Collaboration XVI. *Planck* 2013 results: Cosmological parameters (p11). *Submitted to A&A*, 2013.

Planck Collaboration XVII. *Planck* 2013 results: Gravitational lensing by large-scale structure (p12). *Submitted to A&A*, 2013.

Planck Collaboration XVIII. Planck early results. XVIII. The power spectrum of cosmic infrared background anisotropies. *A&A*, 536:A18, 2011.

Planck Collaboration XXII. *Planck* 2013 results: Constraints on inflation (p17). *Submitted to A&A*, 2013.

Planck Collaboration XXIII. *Planck* 2013 results: Isotropy and statistics of the CMB (p09). *Submitted to A&A*, 2013.

Planck Collaboration XXIV. *Planck* 2013 results: Constraints on primordial non-Gaussianity (p09a). *Submitted to A&A*, 2013.

Planck Collaboration XXIX. *Planck* 2013 results: The Planck catalogue of Sunyaev-Zeldovich sources (p05a). *Submitted to A&A*, 2013.

Planck Collaboration XXV. *Planck* 2013 results: Searches for cosmic strings and other topological defects (p20). *Submitted to A&A*, 2013.

Planck Collaboration XXVIII. *Planck* 2013 results: The Planck Catalogue of Compact Sources (p05). *Submitted to A&A*, 2013.

Planck HFI Core Team. Planck early results, IV. First assessment of the High Frequency Instrument in-flight performance. *A&A*, 536:A4, 2011.

A. Rajantie. Magnetic monopoles in field theory and cosmology. *Royal Society of London Philosophical Transactions Series A*, 370:5705–5717, December 2012. doi: 10.1098/rsta.2011.0394.

D. Regan, P. Mukherjee, and D. Seery. General CMB bispectrum analysis using wavelets and separable modes. *ArXiv e-prints*, February 2013.

B. Reichborn-Kjennerud, A. M. Aboobaker, P. Ade, F. Aubin, C. Baccigalupi, C. Bao, J. Borrill, C. Cantalupo, D. Chapman, J. Didier, M. Dobbs, J. Grain, W. Grainger, S. Hanany, S. Hillbrand, J. Hubmayr, A. Jaffe, B. Johnson, T. Jones, T. Kisner, J. Klein, A. Korotkov, S. Leach, A. Lee, L. Levinson, M. Limon, K. MacDermid, T. Matsumura, X. Meng, A. Miller, M. Milligan, E. Pascale, D. Polsgrove, N. Ponthieu, K. Raach, I. Sagiv, G. Smecher, F. Stivoli, R. Stompor, H. Tran, M. Tristram, G. S. Tucker, Y. Vinokurov, A. Yadav, M. Zaldarriaga, and K. Zilic. EBEX: a balloon-borne CMB polarization experiment. In *Society of Photo-Optical Instrumentation Engineers (SPIE) Conference Series*, volume 7741 of *Society of Photo-Optical Instrumentation Engineers (SPIE) Conference Series*, July 2010. doi: 10.1117/12.857138.

S. Renaux-Petel, S. Mizuno, and K. Koyama. Primordial fluctuations and non-Gaussianities from multifield DBI Galileon inflation. *J. Cosmology Astropart. Phys.*, 11:42, November 2011. doi: 10.1088/1475-7516/2011/11/042.

G. I. Rigopoulos, E. P. S. Shellard, and B. J. W. van Tent. Large non-Gaussianity in multiple-field inflation. *Phys. Rev. D*, 73(8):083522, April 2006. doi: 10.1103/PhysRevD.73.083522.

G. I. Rigopoulos, E. P. S. Shellard, and B. J. W. van Tent. Quantitative bispectra from multifield inflation. *Phys. Rev. D*, 76(8):083512, October 2007. doi: 10.1103/PhysRevD.76.083512.

O. Rudjord, F. K. Hansen, X. Lan, M. Liguori, D. Marinucci, and S. Matarrese. An Estimate of the Primordial Non-Gaussianity Parameter f $_{NL}$ Using the Needlet Bispectrum from WMAP. *ApJ*, 701:369–376, August 2009. doi: 10.1088/0004-637X/701/1/369.

J. Ruhl, P. A. R. Ade, J. E. Carlstrom, H.-M. Cho, T. Crawford, M. Dobbs, C. H. Greer, N. w. Halverson, W. L. Holzapfel, T. M. Lanting, A. T. Lee, E. M. Leitch, J. Leong, W. Lu, M. Lueker, J. Mehl, S. S. Meyer, J. J. Mohr, S. Padin, T. Plagge, C. Pryke, M. C. Runyan, D. Schwan, M. K. Sharp, H. Spieler, Z. Staniszewski, and A. A. Stark. The South Pole Telescope. In C. M. Bradford, P. A. R. Ade, J. E. Aguirre, J. J. Bock, M. Dragovan, L. Duband, L. Earle, J. Glenn, H. Matsuhara, B. J. Naylor, H. T. Nguyen, M. Yun, and J. Zmuidzinas, editors, *Society of Photo-Optical Instrumentation Engineers (SPIE) Conference Series*, volume 5498 of *Society of Photo-Optical Instrumentation Engineers (SPIE) Conference Series*, pages 11–29, October 2004. doi: 10.1117/12.552473.

R. K. Sachs and A. M. Wolfe. Perturbations of a Cosmological Model and Angular

Variations of the Microwave Background. *ApJ*, 147:73, January 1967. doi: 10.1086/148982.

M. P. Salem. Generation of density perturbations at the end of inflation. *Phys. Rev. D*, 72(12):123516, December 2005. doi: 10.1103/PhysRevD.72.123516.

D. S. Salopek and J. R. Bond. Nonlinear evolution of long-wavelength metric fluctuations in inflationary models. *Phys. Rev. D*, 42:3936–3962, December 1990. doi: 10.1103/PhysRevD.42.3936.

M. Sasaki, J. Väliviita, and D. Wands. Non-Gaussianity of the primordial perturbation in the curvaton model. *Phys. Rev. D*, 74(10):103003, November 2006. doi: 10.1103/PhysRevD.74.103003.

S. Scodeller, O. Rudjord, F. K. Hansen, D. Marinucci, D. Geller, and A. Mayeli. Introducing Mexican Needlets for CMB Analysis: Issues for Practical Applications and Comparison with Standard Needlets. *ApJ*, 733:121, June 2011. doi: 10.1088/0004-637X/733/2/121.

L. Senatore, K. M. Smith, and M. Zaldarriaga. Non-Gaussianities in single field inflation and their optimal limits from the WMAP 5-year data. *J. Cosmology Astropart. Phys.*, 1:28, January 2010. doi: 10.1088/1475-7516/2010/01/028.

G. Shiu and J. Xu. Effective field theory and decoupling in multifield inflation: An illustrative case study. *Phys. Rev. D*, 84(10):103509, November 2011. doi: 10.1103/PhysRevD.84.103509.

J. L. Sievers, R. A. Hlozek, M. R. Nolta, V. Acquaviva, G. E. Addison, P. A. R.

Ade, P. Aguirre, M. Amiri, J. W. Appel, L. F. Barrientos, E. S. Battistelli, N. Battaglia, J. R. Bond, B. Brown, B. Burger, E. Calabrese, J. Chervenak, D. Crichton, S. Das, M. J. Devlin, S. R. Dicker, W. Bertrand Doriese, J. Dunkley, R. Dünner, T. Essinger-Hileman, D. Faber, R. P. Fisher, J. W. Fowler, P. Gallardo, M. S. Gordon, M. B. Gralla, A. Hajian, M. Halpern, M. Hasselfield, C. Hernández-Monteagudo, J. C. Hill, G. C. Hilton, M. Hilton, A. D. Hincks, D. Holtz, K. M. Huffenberger, D. H. Hughes, J. P. Hughes, L. Infante, K. D. Irwin, D. R. Jacobson, B. Johnstone, J. Baptiste Juin, M. Kaul, J. Klein, A. Kosowsky, J. M Lau, M. Limon, Y.-T. Lin, T. Louis, R. H. Lupton, T. A. Marriage, D. Marsden, K. Martocci, P. Mauskopf, M. McLaren, F. Menanteau, K. Moodley, H. Moseley, C. B Netterfield, M. D. Niemack, L. A. Page, W. A. Page, L. Parker, B. Partridge, R. Plimpton, H. Quintana, E. D. Reese, B. Reid, F. Rojas, N. Sehgal, B. D. Sherwin, B. L. Schmitt, D. N. Spergel, S. T. Staggs, O. Stryzak, D. S. Swetz, E. R. Switzer, R. Thornton, H. Trac, C. Tucker, M. Uehara, K. Visnjic, R. Warne, G. Wilson, E. Wollack, Y. Zhao, and C. Zuncke. The Atacama Cosmology Telescope: Cosmological parameters from three seasons of data. *ArXiv e-prints*, January 2013.

E. Silverstein and D. Tong. Scalar speed limits and cosmology: Acceleration from D-cceleration. *Phys. Rev. D*, 70(10):103505, November 2004. doi: 10.1103/PhysRevD.70.103505.

J. Smidt, A. Amblard, P. Serra, and A. Cooray. Measurement of primordial non-Gaussianity using the WMAP 5-year temperature skewness power spectrum. *Phys. Rev. D*, 80(12):123005, December 2009. doi: 10.1103/PhysRevD.80.123005.

K. M. Smith and M. Zaldarriaga. Algorithms for bispectra: forecasting, optimal analysis and simulation. *MNRAS*, 417:2–19, October 2011a. doi: 10.1111/j.1365-2966.2010.18175.x.

K. M. Smith and M. Zaldarriaga. Algorithms for bispectra: forecasting, optimal analysis and simulation. *MNRAS*, 417:2–19, October 2011b. doi: 10.1111/j.1365-2966.2010.18175.x.

K. M. Smith, L. Senatore, and M. Zaldarriaga. Optimal limits on f_{NL}^{local} from WMAP 5-year data. *J. Cosmology Astropart. Phys.*, 9:006, September 2009. doi: 10.1088/1475-7516/2009/09/006.

G. F. Smoot, C. L. Bennett, A. Kogut, E. L. Wright, J. Aymon, N. W. Boggess, E. S. Cheng, G. de Amici, S. Gulkis, M. G. Hauser, G. Hinshaw, P. D. Jackson, M. Janssen, E. Kaita, T. Kelsall, P. Keegstra, C. Lineweaver, K. Loewenstein, P. Lubin, J. Mather, S. S. Meyer, S. H. Moseley, T. Murdock, L. Rokke, R. F. Silverberg, L. Tenorio, R. Weiss, and D. T. Wilkinson. Structure in the COBE differential microwave radiometer first-year maps. *ApJ*, 396:L1–L5, September 1992. doi: 10.1086/186504.

J.-L. Starck, Y. Moudden, P. Abrial, and M. Nguyen. Wavelets, ridgelets and curvelets on the sphere. *A&A*, 446:1191–1204, February 2006. doi: 10.1051/0004-6361:20053246.

Jean-Luc Starck, Fionn Murtagh, and Jalal M. Fadili. *Sparse image and signal processing*. Cambridge University Press, Cambridge, 2010. ISBN 978-0-521-11913-9. doi: 10.1017/CBO9780511730344. URL http://dx.doi.org/10.1017/CBO9780511730344. Wavelets, curvelets, morphological diversity.

J. A. Tauber, N. Mandolesi, J.-L. Puget, T. Banos, M. Bersanelli, F. R. Bouchet, R. C. Butler, J. Charra, G. Crone, J. Dodsworth, and et al. Planck pre-launch status: The Planck mission. *A&A*, 520:A1+, September 2010. doi: 10.1051/0004-6361/200912983.

L. Toffolatti, F. Argueso Gomez, G. de Zotti, P. Mazzei, A. Franceschini, L. Danese, and C. Burigana. Extragalactic source counts and contributions to the anisotropies of the cosmic microwave background: predictions for the Planck Surveyor mission. *MNRAS*, 297:117–127, June 1998. doi: 10.1046/j.1365-8711.1998.01458.x.

A. J. Tolley and M. Wyman. Equilateral non-Gaussianity from multifield dynamics. *Phys. Rev. D*, 81(4):043502, February 2010. doi: 10.1103/PhysRevD.81.043502.

E. Tzavara and B. van Tent. Bispectra from two-field inflation using the long-wavelength formalism. *J. Cosmology Astropart. Phys.*, 6:026, June 2011. doi: 10.1088/1475-7516/2011/06/026.

L. Verde and D. N. Spergel. Dark energy and cosmic microwave background bispectrum. *Phys. Rev. D*, 65(4):043007, February 2002a. doi: 10.1103/PhysRevD.65.043007.

L. Verde and D. N. Spergel. Dark energy and cosmic microwave background bispectrum. *Phys. Rev. D*, 65(4):043007, February 2002b. doi: 10.1103/PhysRevD.65.043007.

L. Verde, L. Wang, A. F. Heavens, and M. Kamionkowski. Large-scale structure,

the cosmic microwave background and primordial non-Gaussianity. *MNRAS*, 313:141–147, March 2000. doi: 10.1046/j.1365-8711.2000.03191.x.

L. Verde, R. Jimenez, L. Alvarez-Gaume, A. F. Heavens, and S. Matarrese. Multivariate joint PDF for non-Gaussianities: exact formulation and generic approximations. *ArXiv e-prints*, January 2013.

F. Vernizzi and D. Wands. Non-Gaussianities in two-field inflation. *J. Cosmology Astropart. Phys.*, 5:19, May 2006. doi: 10.1088/1475-7516/2006/05/019.

A. Vilenkin and E. P. S. Shellard. *Cosmic strings and other topological defects*. 1994.

L. Wang and M. Kamionkowski. Cosmic microwave background bispectrum and inflation. *Phys. Rev. D*, 61(6):063504, March 2000. doi: 10.1103/PhysRevD.61.063504.

M. White and W. Hu. The Sachs-Wolfe effect. *A&A*, 321:8–9, May 1997.

A. P. S. Yadav and B. D. Wandelt. Evidence of Primordial Non-Gaussianity (f_{NL}) in the Wilkinson Microwave Anisotropy Probe 3-Year Data at 2.8σ. *Physical Review Letters*, 100(18):181301, May 2008. doi: 10.1103/PhysRevLett.100.181301.

A. P. S. Yadav and B. D. Wandelt. Primordial Non-Gaussianity in the Cosmic Microwave Background. *Advances in Astronomy*, 2010:565248, 2010. doi: 10.1155/2010/565248.

A. P. S. Yadav, E. Komatsu, and B. D. Wandelt. Fast Estimator of Primordial Non-

Gaussianity from Temperature and Polarization Anisotropies in the Cosmic Microwave Background. *ApJ*, 664:680–686, August 2007. doi: 10.1086/519071.

A. P. S. Yadav, E. Komatsu, B. D. Wandelt, M. Liguori, F. K. Hansen, and S. Matarrese. Fast Estimator of Primordial Non-Gaussianity from Temperature and Polarization Anisotropies in the Cosmic Microwave Background. II. Partial Sky Coverage and Inhomogeneous Noise. *ApJ*, 678:578–582, May 2008a. doi: 10.1086/586695.

A. P. S. Yadav, E. Komatsu, B. D. Wandelt, M. Liguori, F. K. Hansen, and S. Matarrese. Fast Estimator of Primordial Non-Gaussianity from Temperature and Polarization Anisotropies in the Cosmic Microwave Background. II. Partial Sky Coverage and Inhomogeneous Noise. *ApJ*, 678:578–582, May 2008b. doi: 10.1086/586695.

D. G. Yamazaki, T. Kajino, G. J. Mathews, and K. Ichiki. The search for a primordial magnetic field. *Phys. Rep.*, 517:141–167, August 2012. doi: 10.1016/j.physrep.2012.02.005.

M. Zaldarriaga. Non-Gaussianities in models with a varying inflaton decay rate. *Phys. Rev. D*, 69(4):043508, February 2004. doi: 10.1103/PhysRevD.69.043508.